MANIPULATING LIGHT USING NANOSTRUCTURES

by

Anil Ghimire

A dissertation submitted to the faculty of
The University of Utah
in partial fulfillment of the requirements for the degree of

Doctor of Philosophy

in

Physics

Department of Physics and Astronomy

The University of Utah

December 2014

The University of Utah Graduate School

STATEMENT OF DISSERTATION APPROVAL

The following faculty members served as the supervisory committee chair and members for the dissertation of **Anil Ghimire**

Dates at right indicate the members' approval of the dissertation.

Jordan M. Gerton,	Chair	08/14/2014 Date Approved
Benjamin Bromley,	Member	08/14/2014 Date Approved
Shanti Deemyad,	Member	08/14/2014 Date Approved
Joel M. Harris,	Member	08/14/2014 Date Approved
Brian Saam,	Member	08/14/2014 Date Approved

The dissertation has also been approved by **Carleton DeTar**

Chair of the Department of **Physics and Astronomy**

and by **David B. Kieda**, Dean of The Graduate School.

ABSTRACT

This dissertation describes progress made towards the control of emission direction and polarization from a single emitter using a sharp gold-coated atomic force microscope tip. When a metallic tip is scanned in the emitter near-field, the probe acts as a secondary emitter such that the superposition of electromagnetic fields from these two emitters modifies the emission polarization and pattern in the far-field.

The physical mechanism underlying this ability to manipulate the emission polarization and direction is studied in detail using a unique data acquisition technique and finite-difference time domain (FDTD) simulations. This technique enables us to reveal how the polarization of emitted photons from a quantum dot (QD) is modified as a gold-coated tip is scanned laterally and vertically in its proximity, and the FDTD simulations are used to calculate the angular emission pattern. The simulated emission pattern at the back-focal plane enables us to identify how the direction of emitted photons is altered as the gold tip is scanned in the proximity of a dipole emitter.

This dissertation also highlights a novel back-focal imaging technique correlated with the vertically oscillating probe. By pulsing the continuous-wave laser at various phases of tip oscillation and using the near-field interaction of the tip-sample, the exact tip-sample distance can be identified. Tip-induced modification of the angular emission pattern from an individual quantum dot is experimentally demonstrated.

This work also includes the study of the emission properties of GaN nanowires. A

hyper-spectral imaging technique combined with spectral center of mass (SCOM) analysis helps us to identify the spectral inhomogeneity within a nanowire. The spectral information within a diffraction-limited spot of a nanowire provides the insight regarding the distribution of mid-gap defect states within a nanowire.

To my family - Garima and Sophie

TABLE OF CONTENTS

ACKNOWLEDGEMENTS

First, I would like to thank my advisor, Prof. Jordan M. Gerton, for his exemplary guidance, care, and constant encouragement. I was so fortunate to experience and learn from his knowledge, patience, and critical thinking which led to the completion of this study. I cannot express enough thanks to my supervisory committee members for their support: Professors Shanti Deemyad, Brian Saam, Ben Bromley, and Joel M. Harris.

My completion of this project could not be accomplished without the support of my lab members, Dr. Analia Dall'Asen, Jessica Johnston, Charles McGuire, Sophia Dimas, Mary Harges, and Cassandra Hammons. I would like to thank Yuchen Young for his helpful discussions and willingness to help in any way possible. I would not forget my former group members Dr. Ben Mangum and Dr. Eyal Shafran, who introduced me to the field and experimental techniques. I would like to thank Carl Ebeling, who as a good friend was always willing to help and give his best suggestions. A special thanks to new lab member Lauren Simonsen, who has been an excellent proofreader and to Dr. Tek Basel for helping to resolve technical issues in writing.

I am indebted to my parents and family members for their love and inspiration with their best wishes. I would like to express my gratitude to my caring and loving wife, Garima Sapkota, for her continuous support and encouragement during my studies.

CHAPTER 1

INTRODUCTION

Near-field optics includes a wide variety of phenomena related to optical interactions that occur within a distance from an object that is less than the wavelength of light. A central goal of near-field optics is to extend the use of optical techniques to understand, construct, and optimize light-matter interactions within a subwavelength volume. Previously, it was not possible to optically interact selectively with nanoscale features because the diffraction limit prevents focusing light to a size smaller than approximately half the wavelength (~ 200 nm in visible range) [1]. Recently, several new approaches have been developed to surpass the diffraction limit, including far-field super-resolution [2, 3] and near-field microscopy [4-7] techniques. Some obvious potential technological applications that arise from breaking the diffraction limit are high-resolution microscopy and ultra-high density information storage and retrieval. Besides the technological applications, nano-optics also opens new doors to fundamental research on nanometer sized structures.

In recent years, the advent of nanoscience and nanotechnology has provided the ability to fabricate fine structures with nanometer-scale dimensions (i.e., nanostructures), well below the diffraction limit for visible light. The optical response of these structures can be very different from their respective bulk properties. Most importantly, these properties vary based on the exact shape, size, and material of nanostructures, which

allows the optical properties to be tuned by careful design of the nanostructures and the materials that surround them. For example, scattering from a metallic nanoparticle can be strongly modified in the presence of specific analyte solutions/environment, which can be useful for sensing applications [8]. In addition, metallic nanostructures can act as optical nanoantennas (counterparts to radio and microwave antennas) to decrease the optical impedance mismatch between the near-field ($\ll \lambda$) and far-field ($\gg \lambda$) regimes, and thereby enhance the optical interaction between light and single quantum emitters including quantum dots (QDs) [9, 10].

The central issue of this dissertation deals with the optical interactions between a quantum emitter and a sharp metallic tip that functions as a nanoantenna. In general, by coupling an emitter to an antenna, the near-field of the emitter interacts through the antenna mode. For a resonant antenna, the large local density of optical states (LDOS) leads to emission properties such as direction, polarization, transition rates, and spectrum which are strongly influenced by the antenna modes [11, 12]. In contrast to a resonant antenna, the nonresonant sharp tips used in this work have a much smaller LDOS which leads emission properties that depend very sensitively on the position of the tip and the orientation of the emitter. In particular, this work is related to the control of emission polarization and direction of light at the various length scales in the near-field of an emitter, which was not been studied previously in detail [11-21]. Interestingly, we found that when separated by an intermediate distance, the emitter and tip contribute roughly equally to the emission properties. The maximum control over the emission direction and polarization is achieved in this intermediate zone, with peformance similar to the resonant antennas, but with much better tunability. Such control over the polarization together with

the direction of emission from a single photon source could have implications for quantum information processing [22-24].

1.1 Optical Resolution and Evanescent Field

In a classical microscopy system, light is focused by a microscope lens onto/from a sample. In practice, the collection lens is placed many wavelengths (λ) distant from the object surface, so the high spatial frequencies corresponding to fine features of the object decay before reaching the lens [25]. This inability to collect the highest spatial frequencies limits the spatial resolution of a conventional optical system and leads to the famous *Rayleigh criterion* [26]:

$$\delta = \frac{0.61\lambda}{\mathrm{NA}} \tag{1.1}$$

where δ is the minimum resolvable distance between two objects, and NA is the numerical aperture of the objective lens. The numerical aperture is defined by $\mathrm{NA} = n\sin\theta$, with n being the refractive index of the medium within which the lens operates while the angle θ is the half-angle of the maximum cone of light that can enter or exit the lens from the focal position, as shown in Figure 1.1. Therefore, the optical resolution can be enhanced by using a high NA objective or very short wavelengths. The highest NA objective available is an oil immersion with $\mathrm{NA} = 1.49$. So the smallest features that can be resolved by conventional microscopy are not less than $\sim\lambda/2$. This optical phenomenon is a major limitation in the study of nanoscience.

Heisenberg's uncertainty principle can be used to understand the concept of optical resolution. For photons, the relationship holds as:

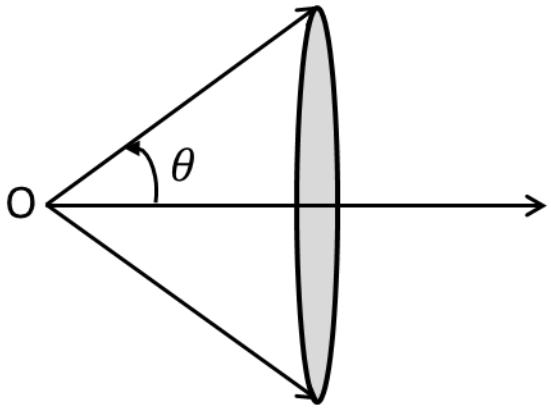

Figure 1.1 Numerical aperture of a lens with respect to a focal point O depends on the half angle θ that corresponds to maximum cone angle that light enters or exits the lens.

$$\Delta(\hbar k_x) \cdot \Delta x \geq \frac{\hbar}{2} \Longrightarrow \Delta x \geq \frac{1}{2\Delta k_x}. \tag{1.2}$$

This relation indicates that the uncertainty in the spatial position (Δx) decreases with increasing spatial frequency bandwidth (Δk_x); that is, the spatial resolution increases. The maximum possible spatial frequency carried in a propagating field is given by $k_{max} = 2\pi n/\lambda$. In this case, the resolution cannot be better than:

$$\Delta x_{min} = \lambda/(2\pi n) \tag{1.3}$$

In practice, the entire spatial frequency spectrum $\Delta k = 0 \ldots\ldots k_{max}$ is not collected by the lens and the upper limit is defined in terms of the collection angle of an objective, i.e.:

$$\Delta x_{min} = \lambda/(2\pi NA) \tag{1.4}$$

which is a similar expression to the diffraction limit. Thus, the spatial resolution is limited by the inability to detect the nonpropagating components (evanescent waves) of the light.

By detecting the evanescent waves, spatial resolution can be enhanced without violating the uncertainty principle. A thorough discussion about detecting evanescent waves in the near-field optics can be found in Ref. [27, 28]. To understand how it is possible, consider wave vectors in the x- and z-directions forming a total wave vector as:

$$k^2 = k_x^2 + k_z^2 = (2\pi/\lambda)^2 \tag{1.5}$$

Increasing the value of k_x more than total wave vector k is possible if k_z becomes imaginary (i.e., $k_z \rightarrow ik_z$). The expression for the wave vector in x-direction takes the form: $k_x^2 = (2\pi/\lambda)^2 + |k_z|^2$ which increases the optical resolution in z-direction as given by Equation 1.4. If we define k_z as an imaginary, the plane wave in the z-direction becomes $e^{ik_z z} \rightarrow e^{-|k_z|z}$ and the field decays exponentially, as expected for evanescent waves. Now, the problem is to detect such strongly localized decaying light. To do so, an object of subwavelength feature size should be brought into the evanescent zone (near-field zone) as discussed in detail in the following section.

1.2 Probing Evanescent Waves

The evanescent waves near an optical interface decay exponentially over a length scale much shorter than the wavelength. One way to detect evanescent waves is by placing a local detector very close to the specimen surface ($d < \lambda$). Realization of such detection schemes can be achieved using aperture-type NSOM [29]. In this scheme, a tapered fiber probe or aperture probe can be used to excite and/or detect light from the sample within a subwavelength distance. In this technique, the spatial resolution is mainly limited by the aperture size rather than the wavelength of light. The main drawback of aperture type NSOM is that the transmission/detection of the signal drops as the aperture

size reduces in the subwavelength range ($\propto [d/\lambda]^6$).

Another way of probing evanescent waves is by scanning a local scatterer near the sample surface, such as in apertureless NSOM (Figure 1.2). In this technique, a small nanostructure or a sharp tip is brought within a subwavelength distance from the sample. A sharp tip or particle perturbs the local field at the sample surface; the response of this perturbation can be detected in the far-field. For example, emission from a dipole source consists of both propagating and evanescent components [30]. The evanescent components are confined within a subwavelength distance from the source. Due to the presence of a local scatterer (a sharp tip), the evanescent waves are converted partially to propagating waves and detected in the far-field. Besides operating as a local scatterer, the sharp pointed probe can act as a point light source. Under proper illumination conditions and using suitable probe materials, the excitation light can be strongly enhanced at the apex of the probe. When the probe is brought in the proximity of a fluorescent sample, a highly localized near-field interaction between the enhanced field and the sample can be achieved, as shown in Figure 1.2. As a local scatterer and/or nanoscopic light source, the sharp tip exploits the evanescent waves to enhance the spatial resolution. The local-intensity enhanced technique is commonly known as tip-enhanced near-field scanning optical microscopy [7].

In order to detect the highly decaying field, one needs to put a probe within the subwavelength distance as discussed previously. The resulting near-field light-matter coupling can lead to complex or misunderstood results. However, this coupling can also impart the ability to control and manipulate light in the nanoscale regime. The main work of this dissertation relates to controlling the emission properties (polarization and

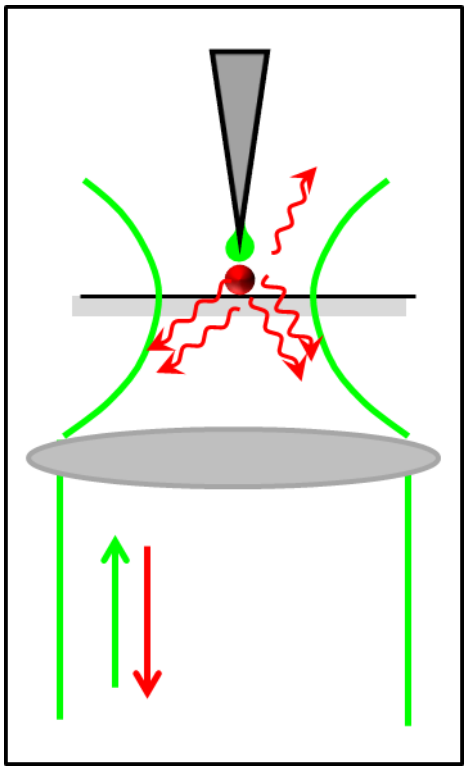

Figure 1.2 Schematic of tip-enhanced NSOM. A sharp atomic force microscope tip is illuminated (green) through an objective lens with a diffraction-limited spot. Using proper illumination conditions, the excitation intensity at the apex of the tip can be highly localized. The enhanced excitation interacts locally with sample surface (or an emitting source). The emission from the sample is also collected by the same lens for detection.

direction) of a single emitter using a sharp metallic tip within the near-field of a QD.

1.3 Outline of Dissertation

In this work, optical interactions in a nanoscale environment are explored. A scattering type NSOM is used to study the light-matter interactions between a single emitter and a metallic tip. Chapter 2 will provide the background theory necessary to understand what the near-field of an emitter is and how it can be useful to control the emission properties. The optical response of metallic nanoparticles, especially scattering mechanisms, are discussed in detail. Chapter 3 will discuss the experimental setup

required to make a near-field scanning optical microscope. This chapter comprises both the equipment requirements and the basic theory needed to appreciate the design of the instrument. This mainly instrumentation chapter is very useful for a new student in the lab. Chapter 4 gives a brief introduction to a numerical method to solve Maxwell's equations using finite-difference time domain (FDTD) simulations.

In Chapter 5, the near-field interaction between a sharp metallic tip and a single emitter is discussed. The interference of the scattered field from the tip and the field directly emitted from a quantum dot (which results in controlling emission polarization and direction of emitted photons in the system) is studied both experimentally and theoretically. Chapter 6 reports progress in the development of a technique to directly measure the angular emission pattern from a single emitter using back-focal imaging.

In Chapter 7, the optical properties of gallium nitride (GaN) nanowires are presented. Spatial and temporal inhomogeneity in the emission spectrum is explored utilizing different spectroscopy techniques: photoluminescence excitation spectroscopy, time-resolved emission spectroscopy, and hyper-spectral imaging.

CHAPTER 2

THEORETICAL BACKGROUND

The scanning probe microscope used in our lab is an apertureless type near-field optical microscope, also known as a scattering type near-field microscope. The pointed probe of the microscope works as a local scatterer of light, creating a point source that can be scanned over the sample surface. The pointed probe structure can also perturb the near-field of an emitter by scattering the evanescent emission waves into propagating waves, which can be detected in the far-field with a photon counter, camera, or other photo-sensitive detector. The interaction between an emitter and a scanning probe is very complex and depends on the orientation of the emitter as well as the shape, size, and material properties of the probe. The material properties of the probe are modified from its bulk properties when the shape and size of the material enters the nanoscale domain. As a result, the light-matter interactions in a nanoscale environment are fairly complicated.

This chapter will introduce the general theoretical background related to the work in this dissertation. I consider a fluorescent molecule or nanocrystal (quantum dot) as an oscillating dipole. The electric and magnetic field in the near, intermediate, and far-field zones of the source dipole and its radiation patterns are explained. The influence on the emission rate of an emitter in an inhomogeneous environment is examined. Then, the optical properties of noble metals are discussed. Optical responses, particularly the

scattering mechanism of metallic nanostructures, are reviewed for different sizes and shapes of particles. I will discuss the difficulty of solving the Maxwell's equations for an arbitrary structure, which leads to the necessity of numerical solutions. The polarization-dependent scattering from an elongated tip is reviewed. The controlling of the light with a sharp tip for different physical effects (emission, excitation, polarization, direction, etc.) is discussed. Finally, I introduce an optical antenna and its interaction with light.

2.1 Dipole Radiation

Fluorescence in a two-level system can be considered as radiation resulting from an oscillating electric or magnetic dipole in time. The harmonically oscillating electric dipole can be described in the form of a dipole moment (**p**) as:

$$\boldsymbol{p}(t) = \Re\{\boldsymbol{p}\, e^{-i\omega t}\} \tag{2.1}$$

where ω is the frequency of oscillation [1]. The magnetic and electric fields produced in a homogenous medium due to this oscillating dipole are given by:

$$\mathbf{H} = \frac{ck^2}{4\pi}(\mathbf{n}\times\mathbf{p})\frac{e^{ikr}}{r}\left(1-\frac{1}{ikr}\right) \tag{2.2}$$

$$\mathbf{E} = \frac{1}{4\pi\epsilon_0}\left\{k^2(\mathbf{n}\times\mathbf{p})\times\mathbf{n}\frac{e^{ikr}}{r} + [3\mathbf{n}(\mathbf{n}\cdot\mathbf{p})-\mathbf{p}]\left(\frac{1}{r^3}-\frac{ik}{r^2}\right)e^{ikr}\right\} \tag{2.3}$$

where **n** is the unit vector in the direction of **r,** and *k* is the wave number ($k = 2\pi/\lambda$) [31]. If we align the dipole moment along the z-axis such that $\mathbf{p} = \mathrm{p}_0\,\hat{z}$, we can use the coordinate transformation [32] to find **E** and **H** in terms of a spherical coordinate system, as shown in Figure 2.1. We have $\mathbf{n}\times\mathbf{p} = -\mathrm{p}_0\sin\theta\,\hat{\phi}$, $\mathbf{n}\cdot\mathbf{p} = -\mathrm{p}_0\cos\theta$, and

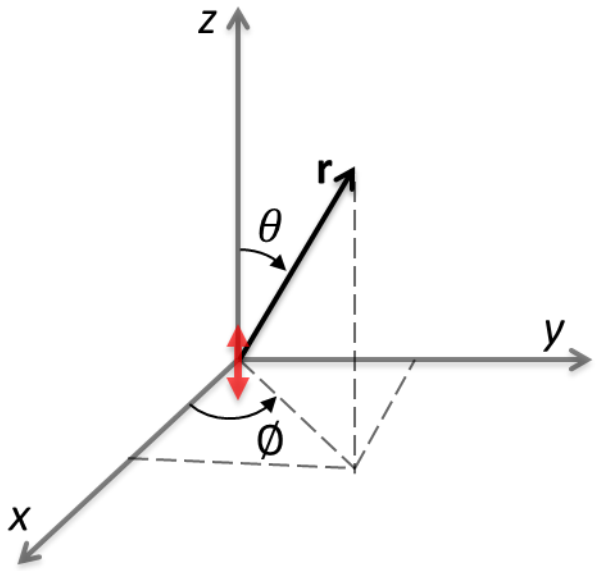

Figure 2.1 Dipole orientation along *z*-axis in spherical coordinate system (r, θ, ϕ).

$\mathbf{p} = \mathrm{p}_0(\cos\theta\,\hat{r} - \sin\theta\,\hat{\theta})$. In the spherical coordinate system, $E_\phi = H_r = H_\theta = 0$. The remaining nonzero components are:

$$E_r = \frac{p_0 \cos\theta}{4\pi\epsilon_0}\frac{e^{ikr}}{r}k^2\left(\frac{2}{k^2r^2} - \frac{2i}{kr}\right) \tag{2.4}$$

$$E_\theta = \frac{p_0 \sin\theta}{4\pi\epsilon_0}\frac{e^{ikr}}{r}k^2\left(\frac{1}{k^2r^2} - \frac{i}{kr} - 1\right) \tag{2.5}$$

$$H_\phi = \frac{p_0 \sin\theta}{4\pi\epsilon_0}\frac{e^{ikr}}{r}k^2\left(-\frac{i}{kr} - 1\right)\sqrt{\frac{\epsilon_0}{\mu_0}} \tag{2.6}$$

In the above expressions, the fields have $1/r^3$, $1/r^2$, and $1/r$ dependence. When $r \ll \lambda$, only the terms with $1/r^3$ contribute to the field known as the *near-field* zone. For $r \approx \lambda$, the terms containing $1/r^2$ dominate, known as *intermediate-field* zone. In the far-field zone, in which $r \gg \lambda$, only the terms containing $1/r$ survive. The magnetic

field in the near-field zone (missing $1/r^3$ term) is negligible compared to the electric field, which implies that the electric field is the dominant contribution in the near-field. The radial component of the electric field (E_r) extends in the near- and intermediate-fields, but the far-field is purely dominated by the transverse electric field. The intermediate-field is 90° out of phase with respect to the near- and far-fields.

Figure 2.2 shows the intensity pattern for a radiating dipole with an oscillating frequency that corresponds to the free space wavelength of 605 nm. The intensity is shown for the distance $r = 20$ nm, 200 nm, and 2,000 nm, which correspond to the near, intermediate, and far-field patterns, respectively. The intensity pattern in the near-field zone is distributed in all directions with bigger lobes along the dipole axis (Figure 2.2a). The far-field intensity pattern is completely different from that of the near-field. There is no field along the direction of the dipole axis. Within one wavelength distance of the dipole, the intensity pattern evolves from the near-field (Figure 2.2a) and approaches the far-field (Figure 2.2a) pattern. The intensity pattern in the intermediate zone changes rapidly with the choice of distance r.

So far, we have discussed the frequency-dependent solution for a harmonically oscillating dipole. The frequency of the electromagnetic radiation associated with this dipole is the same as the frequency of the dipole oscillation. If we rewrite the equations for $E_r, E_\theta,$ and E_ϕ in time-dependent solutions, we will get [1]:

$$E_r(t) = \frac{\cos\theta}{4\pi\epsilon_0}\left(\frac{2}{r^3} + \frac{1}{c}\frac{2}{r^2}\frac{\mathrm{d}}{dt}\right)|\mathbf{p}(t - r/c)| \tag{2.7}$$

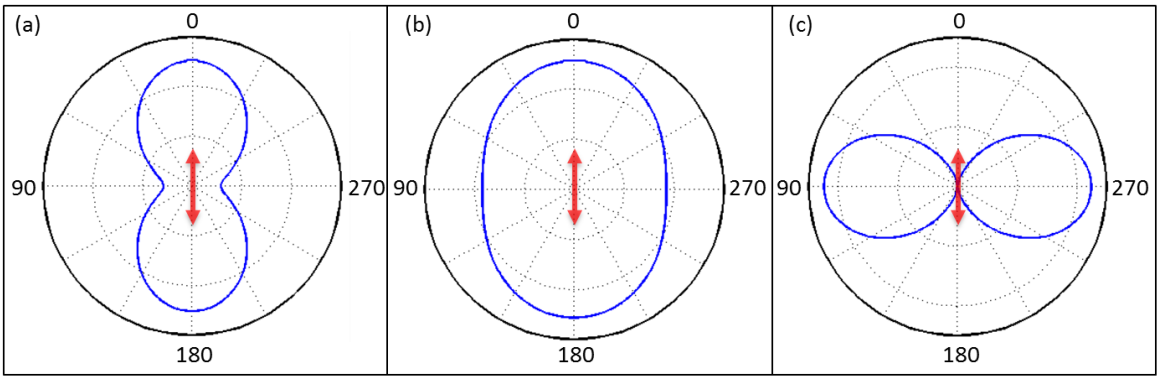

Figure 2.2 Intensity pattern for an oscillating dipole in free space; the frequency of oscillation corresponds to free space wavelength $\lambda = 605$ nm. The red arrow represents the orientation of the dipole moment. (a) Electric field intensity in the near-field zone at $r = 20$ nm. (b) Electric field intensity in the intermediate zone at $r = 200$ nm. (c) Intensity pattern in the far-field at $r = 2{,}000$ nm.

$$E_\theta(t) = \frac{\sin\theta}{4\pi\epsilon_0}\left(\frac{1}{r^3} + \frac{1}{c}\frac{1}{r^2}\frac{\mathrm{d}}{dt} + \frac{1}{c^2}\frac{1}{r}\frac{\mathrm{d}^2}{dt^2}\right)|\mathbf{p}(t - r/c)| \tag{2.8}$$

$$H_\phi(t) = \frac{\sin\theta}{4\pi\epsilon_0}\left(\frac{1}{r^3} + \frac{1}{c}\frac{1}{r^2}\frac{\mathrm{d}}{dt} + \frac{1}{c^2}\frac{1}{r}\frac{\mathrm{d}^2}{dt^2}\right)|\mathbf{p}(t - r/c)|\sqrt{\frac{\epsilon_0}{\mu_0}} \tag{2.9}$$

where c is the velocity of light in free space, the field at the time t is related to the retarded time $(t - r/c)$ at the dipole. The above equations indicate that the near-field for an oscillating dipole is generated due to the position of charges. Similarly, the intermediate-field is produced due to the speed of the charges and the far-field is generated due to the acceleration of the charges forming the dipole.

The power transmitted from the oscillating dipole is calculated by integrating the time-averaged Poynting vector $\langle \mathbf{S} \rangle = (1/2)\,\Re(\mathbf{E} \times \mathbf{H}^*)$ over the enclosed surface. Here, **E** and **H** are the complex fields given in Equations 2.4-2.6. When solving for the

Poynting vector, the near and intermediate-fields vanish and only the far-field of the dipole contributes to the net energy transport. Solving for $\langle \mathbf{S} \rangle$, we get:

$$\langle \mathbf{S} \rangle = \frac{\mathrm{p}_0^2 \sin^2\theta}{32\pi^2\epsilon^2}\frac{1}{r^2}k^4\sqrt{\frac{\epsilon_0}{\mu_o}}\,\hat{r} \tag{2.10}$$

Equation 2.10 indicates that most of the energy is radiated in the direction perpendicular to the dipole moment, and there is zero energy radiated in the direction of the dipole moment. The radiation pattern for a dipole is the same as the far-field intensity pattern in Figure 2.2c. After integrating Equation 2.10 over a closed spherical surface, the total power radiated is given by:

$$P = \frac{\mathrm{p}_0^2}{4\pi\epsilon_0}\frac{\omega^4}{3c^3} \propto \frac{1}{\lambda^4}. \tag{2.11}$$

2.2 Radiation in an Inhomogeneous Environment

When a dipolar light source is in a free space, the decay rate of spontaneous emission is proportional to the density of optical states in the vacuum (Fermi's golden rule), i.e., the vacuum fluctuation explained by quantum electrodynamics. The decay rate in free space is given by $\gamma_0 = P_0/\hbar\omega$, where P_0 is given by Equation 2.11. In an inhomogeneous environment, a harmonically oscillating dipole will experience its own field as a driving force. The driving field is the field that arrives back to the dipole after it has been scattered from a nearby environment. The interacting field for a dipole sitting near the glass substrate and a sharp metallic tip in the near-field of the dipole emitter is shown in Figure 2.3.

In the classical picture, the equation of motion for a harmonically oscillating

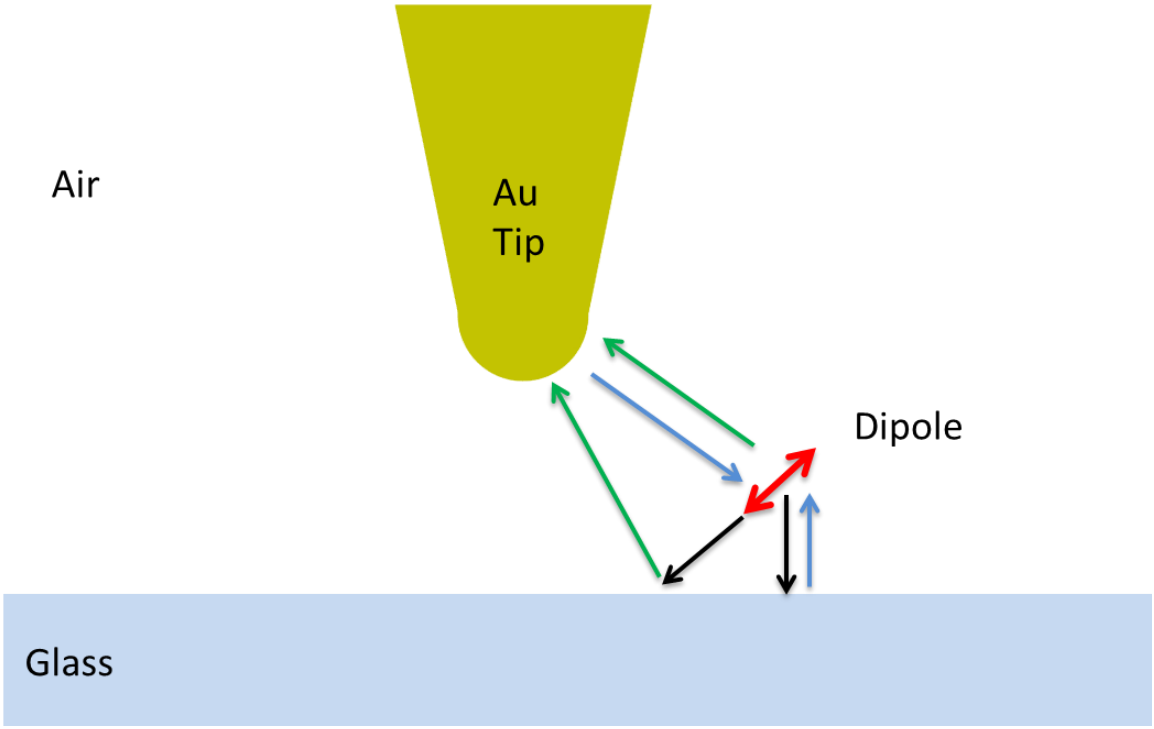

Figure 2.3 Schematic of the interacting fields of a dipole field near the air/glass interface in the presence of a sharp gold tip. Only the first-order interaction is taken into consideration. The red double-headed arrow represents an oscillating dipole. The green arrows are incident fields to the tip. The black arrows represent outgoing field from the dipole. The blue colored arrows show the scattered field back from the tip and the glass.

dipole in the presence of a driving force is written as [33, 34]:

$$\ddot{\mathrm{p}}(t) + \gamma_o \dot{\mathrm{p}}(t) + \omega^2 \mathrm{p}(t) = \frac{q^2}{m} \mathbf{E}_s(t) \tag{2.12}$$

where $\mathrm{p}(t)$ is the harmonically oscillating dipole with frequency ω and $\mathbf{E}_s$ is the secondary local field at the point of the dipole. In our case, $\mathbf{E}_s = \mathbf{E}_{tip} + \mathbf{E}_{glass}$, as shown in Figure 2.3. Due to the presence of driving field, the spontaneous emission rate is modified. In the limit of the modified decay rate $\gamma \ll \omega$, the scattered field $\mathbf{E}_s$ field is weak and Equation 2.12 can be solved. The normalized decay rate is given by:

$$\frac{\gamma}{\gamma_0} = 1 + \mathrm{q_i}\frac{6\pi\epsilon_o}{\mathrm{p}_0^2}\frac{1}{k^3}\,\Im(\mathbf{p}^* \cdot \mathbf{E_s}(\boldsymbol{r_0})) \tag{2.13}$$

where $\mathrm{q_i}$ is defined as the intrinsic quantum yield [1]. Its value ranges from zero to one and indicates the fraction of dissipated energy associated with radiation. The variable k is the wave number.

The fluorescence lifetime $\tau = 1/\gamma$ measures the $1/e$ decay time of the quantum oscillator. The lifetime is modified in an inhomogeneous medium; the ratio of the spontaneous lifetime of a molecule in the medium compared to its lifetime in free space is given by:

$$\frac{\gamma}{\gamma_0} = \frac{\tau_0}{\tau} = \frac{P}{P_0}. \tag{2.14}$$

This equation relates the decay rate to lifetime and the amount of power radiated by a molecule in an inhomogeneous environment normalized to free space. This ratio is also known as the Purcell factor, which gives the environmental effect on a measured spontaneous emission rate [35]. In a 1970 experiment, Drexhage showed that the emission lifetime of Eu^{3+} ions is modified near a silver mirror positioned at various distances from the ions [36].

As the decay rate of a molecule is modified due to the presence of a secondary field at the location of the molecule, the modified decay rate is often too complicated to analytically solve. Thus, numerical methods are employed to calculate the decay rate/lifetime for an arbitrary geometry.

2.3 Optical Constants of Metals

Solving Maxwell's equations in a medium introduces the frequency-dependent dielectric constant when calculating the time and spatial evolution of electric and magnetic fields [1]. The dielectric constants used in electrodynamical calculations are based on solid state physics. A simple model for metals was developed by Drude (1990) based on electrons as a free gas [37]. Sommerfeld made some corrections to the Drude model by incorporating the Pauli-exclusion principle, termed the quasi-free-electron model [38]. Using the quasi-free electron model, the frequency-dependent dielectric constant for a metal can be written as:

$$\epsilon(\omega) = \epsilon_\infty - \frac{\omega_p^2}{\omega(\omega + i\Gamma)} \tag{2.15}$$

where ϵ_∞ includes the contribution of the bound electrons due to the polarizability. The value of $\epsilon_\infty = 1$ if only the conduction electrons contribute to the dielectric function. The bulk plasmon frequency is represented by $\omega_p = \sqrt{(ne^2)/\epsilon_0 m^*}$ with n and m^* as the density and effective mass of conduction electrons while $\Gamma = 1/\tau^*$ is the electron relaxation rate of collisions. The Drude parameters for the noble metals gold (Au), silver (Ag), and cupper (Cu) are given in Table 2.1.

Despite its modest assumptions, the Drude-Sommerfeld model successfully describes many properties of a metal. The dielectric function for metals is well-described by this model when the incident light has low energy. However, at optical frequencies, this model cannot explain the experimentally measured dielectric constants for many metals. At these high frequencies, an extra contribution to the dielectric constant from the higher energy excitation of deeper band electrons into the conduction band must be

Table 2.1 Drude parameters for noble metals Au, Ag, and Cu. Electron density (n) is from reference [39]. Effective mass (m*/me) and relaxation time (τ^*) are from reference [40].

	Au	**Ag**	**Cu**
$\boldsymbol{n}$ **(m^{-3})**	5.88×10^{28}	5.83×10^{28}	4.78×10^{28}
$\boldsymbol{m^*/m_e}$	0.99	0.96	1.49
$\boldsymbol{\tau^*}$ **(sec)**	9.3×10^{-15}	31×10^{-15}	6.9×10^{-15}

included. In noble metals like gold, the electrons are excited from the completely filled d-bands.

Figure 2.4 shows the real and imaginary parts of the dielectric function for bulk gold over a broad wavelength range. At the longer wavelength end of the range, the experimentally measured and theoretically predicted values follow each other. The experimentally measured value departs from the Drude-Sommerfeld model in the short wavelength range due to interband transitions discussed above. The contribution of interband transitions to the dielectric function is calculated by subtracting experimentally measured values from theoretically predicted values. Interband transitions dominate the imaginary part of dielectric function below 690 nm wavelength.

The dielectric function so far discussed is only for bulk materials. When the size of the particle is smaller than the mean free path ($l_f = v_f \tau^*$, v_f : Fermi velocity, v_f/c ~0.05, c: velocity of light in free space), surface scattering adds an additional collision for conduction electrons. This mechanism modifies the relaxation rate (Γ) in Equation 2.15, eventually changing the dielectric function. Both the real and imaginary parts of the dielectric function are changed because they are related to each other by Kramers-Kronig

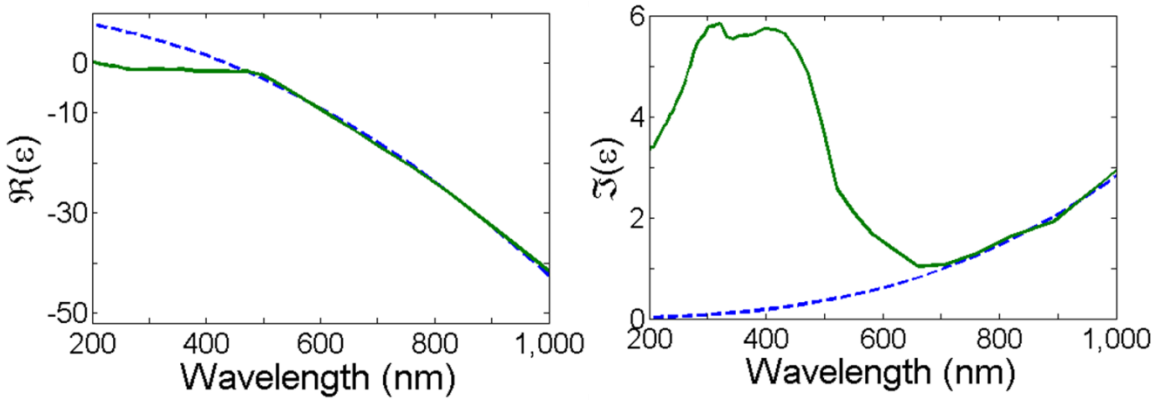

Figure 2.4 The real (a) and imaginary parts (b) of the dielectric function for bulk gold. Continuous (green) lines are the experimentally measured data from Johnson and Christy [40]. The dotted (blue) lines are the calculated values using the Drude-Sommerfeld model (Equation 2.15). The Drude parameters used in the calculation are: $\epsilon_\infty = 9.84$, $\hbar\omega_p = 9$ eV, $h\tau^{*-1} = 0.067$eV from reference [40, 41].

relations [39]. For extremely small particles, the dielectric function depends on its size and shape.

Below the plasma frequency (ω_p), the electromagnetic field cannot penetrate into the bulk metal. In practice, there is a finite penetration of the field. To understand how the electromagnetic field infiltrates inside a metal surface, let us assume a plane wave in a material:

$$\mathrm{E} = \mathrm{E}_0\, e^{i(\mathbf{k}\cdot\boldsymbol{r}-\omega t)} \tag{2.16}$$

where the wave vector $\mathbf{k} = \omega n/c\hat{s}$ is given in terms of the refractive index n of the medium. The refractive index (the square root of the dielectric function for metals) is complex ($n \to n + ik'$). The plane wave (Equation 2.16) in terms of real and imaginary parts of refractive index is written as:

$$\mathrm{E} = \mathrm{E}_0\, e^{-\frac{\omega k'}{c}(\hat{s}\cdot\boldsymbol{r})}\, e^{i(\mathrm{n}\,\hat{s}\cdot\boldsymbol{r}-\omega t)} \tag{2.17}$$

which is attenuated inside the metal. The penetration depth (δ) is defined as the distance within the metal in which the power density falls to $1/e^2$ of its initial value. This depth is given by:

$$\delta = \frac{c}{2\omega k'} = \frac{\lambda}{4\pi k'}. \tag{2.18}$$

The penetration depth is usually a very small fraction of the wavelength. For a perfect metal with infinite conductivity, k' becomes infinite as well; there is no penetration of the electromagnetic field inside such a conductor and the entire incident light is reflected [32]. The calculated value of δ for gold at a 605 nm wavelength is 31.8 nm. Understanding this length is crucial when dealing with nanostructures of sizes comparable to δ at optical frequencies.

2.4 Optical Response of a Gold Nano-Sphere

The optical properties of a gold nanosphereare mainly governed by the collective oscillation response of conduction electrons. When the diameter of the metal nanoparticle is comparable to the penetration depth, the external electric field is able to penetrate and displace the electron gas away from the equilibrium. This creates a dipole-like charge separation, as shown in Figure 2.5. The electron build up on one surface and residual positive charge on an opposite surface produces a restoring force, resulting in charge oscillations. When the frequency of light is resonant with the natural frequency of these self-oscillations, the oscillation amplitude is maximized; this is known as the *plasmon*

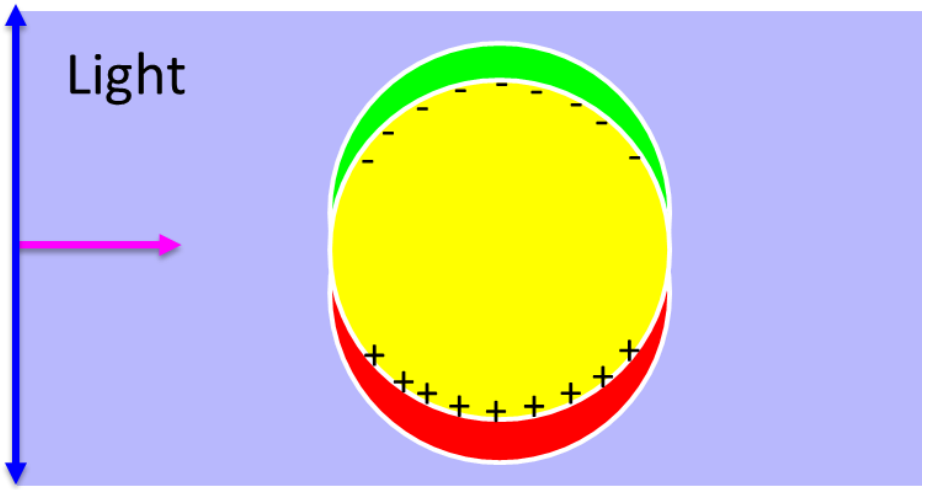

Figure 2.5 Schematic of the instantaneous plasmon mode of oscillation in the external electromagnetic field.

resonance condition. Mathematically, the magnitude and width of the resonance are related to the damping constant. The damping can lead to both radiative and nonradiative energy dissipation. The resonance frequency is related to the restoring force, which depends on the separation of surface charges. The separation of charges is related to the polarizability of metal and the surrounding medium. With an oscillating external field, the surface charges also oscillate, forming an oscillating dipole. This oscillation of charges leads to electromagnetic radiation.

For a particle much smaller than the free-space light wavelength ($a \sim \lambda/10$), the instantaneous electromagnetic field within the particle can be approximated as having constant phase over the dimensions of the particle. In this electrostatic limit (neglecting retardation effects), the polarizability of the metallic nanosphere is given by [31]:

$$\alpha = 4\pi a^3 \left(\frac{\epsilon_r - 1}{\epsilon_r + 2}\right) \tag{2.19}$$

where a is the radius of particle and $\epsilon_r = \epsilon_{metal}/\epsilon_{medium}$ is the complex relative dielectric constant of the metal relative to the medium in which it is embedded. For optical frequencies, the real part of the dielectric constant is typically negative and for the particular frequency when $\Re(\epsilon_r) = -2$, the magnitude of polarizability is maximumized. This condition is known as *localized surface plasmon resonance*.

2.5 Scattering and Absorption by the Nanoparticle

As we discussed in the previous section, the external oscillating field creates a collective oscillation of charge (plasmons). This oscillation decays by two mechanisms: radiative (i.e., by emission of a photon) or nonradiative (i.e., by thermal dissipation). From classical electrodynamics, the scattered field is due to radiation associated with the oscillating charge distribution.

We can understand the nonradiative decay of a plasmon by considering each electron as independent in the Drude-Sommerfeld model. The plasmons are then a superposition of independent electron oscillations. The nonradiative decay is due to the dephasing of each electron oscillation. In a naïve picture, the electrons get scattered multiple times with phonons, lattice ions, others electrons, metal surfaces, impurities, etc. during oscillation. The frequency-dependent conductivity $\sigma(\omega)$ can be written in terms of the imaginary part of complex dielectric constant:

$$\epsilon = \epsilon' + i\frac{\sigma}{\epsilon_0 \omega} \tag{2.20}$$

where ϵ_0 is the permittivity of free space. The current associated with the conduction of electrons experiences the frequency-dependent resistance in the metal implied by Equation 2.20. The energy dissipated through this nonradiative decay will be lost via

Joule heating. In this model, the total time-dependent current (J_t) can be written as source current (J_s) that generates the scattered field and loss current (J_c) that is associated with absorption, i.e., ultimately heat.

Scattering and absorption always occur simultaneously: a fraction of the oscillation energy is lost via thermal dissipation – absorption, and the balance is radiated into the far-field. The total energy loss associated with both scattering and absorption is known as *extinction*, and the frequency-dependent cross-sections for extinction (σ_{ext}), scattering (σ_{sca}) and absorption (σ_{abs}) are related by:

$$\sigma_{ext} = \sigma_{sca} + \sigma_{abs}. \tag{2.21}$$

The radiative quantum yield of the nanoparticle is defined by:

$$\eta = \frac{\sigma_{sca}}{\sigma_{sca} + \sigma_{abs}}. \tag{2.22}$$

2.6 Near- and Far-Field Effects

Plasmons produce both near- and far-field responses in metal nanoparticles. To understand the near- and far-field response of a nanostructure, a finite-difference time domain (FDTD) simulation is performed on a gold nanosphere with an incident plane wave, as shown in Figure 2.6. The total intensity (incident and scattered) in the *xz*-plane passing though the center of a sphere is shown in Figure 2.6a, which shows that intensity is enhanced at the "poles" of the nanoparticle aligned with the polarization direction of incident light (*z*-axis). The near-field intensity enhancement is localized in the vicinity of particle ($d \ll \lambda$).

The far-field intensity pattern for the scattered light from the gold nanosphere is

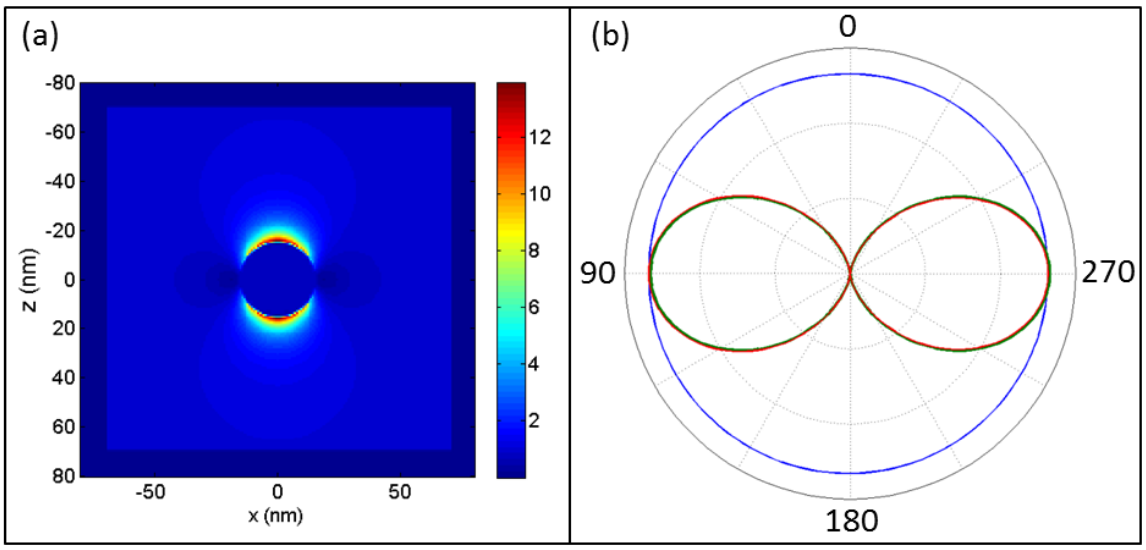

Figure 2.6 FDTD simulation for a gold nanosphere showing near- and far-field effects. A plane wave (polarization vector along *z*-direction and propagation vector along y-direction) is incident on a gold nano sphere (radius = 15 nm). (a) Intensity image in the *xz*-plane passing through the center of sphere. The color scale shows the normalized intensity at 525 nm wavelength, close to the localized surface plasmon resonance. (b) Intensity pattern of the scattered field in far-field region. The superimposed green and red lines are the intensity pattern for scattered field in the *xz* and *yz*-plane, respectively. The blue line represents the intensity pattern for the scattered field in the *xy*-plane.

shown in Figure 2.6b. The intensity pattern in the *xz*- and *yz*-plane are completely overlapped (green and red curves) and resemble the emission pattern of a dipole situated at the center of the sphere with a dipole moment along the direction of polarization of the incident light.

2.7 Scattering for an Arbitrary Structure

Maxwells's equations can be solved analytically for a spherical particle to understand the optical response of such particle, which is known as Mie theory [42] (see Appendix A for size effects on Mie scattering). Mie theory has also been extended for nonspherical particles over the years [43-47]. Unfortunately, it is almost impossible to solve Maxwell's equations analytically in the presence of arbitrarily-shaped nanoparticles

due to complexities of the electromagnetic field in such cases. On the other hand, there are various numerical methods for investigating arbitrary geometries by solving Maxwell's equations self-consistently on a spatial grid using appropriate boundary conditions.

Discretized computational methods were first introduced by Purcell and Pennypacker in 1973 using the discrete dipole approximation (DDA) to simulate optical field distributions near more complex structures [44]. This field was not given much attention until 15-20 years ago [48]. However, the past decade has witnessed an incredible improvement in the understanding and control of the optical response of small metal particles [49-51]. This has been driven by the rapid development of many computational algorithms such as finite-difference time domain (FDTD) [52, 53], the boundary element method (BEM) [54, 55], finite element method (FEM) [56-58], etc. On the other hand, there has been tremendous improvement in chemical synthesis as well as other fabrication techniques to make various sizes and complex shaped metal particles [9, 59-62].

2.8 AFM Tip

The atomic force microscope (AFM) probes used in scattering type NSOM microscopes are generally sharp and elongated in structure, as shown in Figure 2.7. There are a large number of commercial tips available with various apex geometries such as conical, pyramidal, triangular, etc. These tips are made of different materials such as Si, SiN, diamond, metal (Au, Al, Pt), or metal coated on silicon. Selection of the particular tip depends on the type of experiments we want to perform. In this work, we mainly used a gold-coated metal tip with a tip apex radius of less than 25 nm. The gold coating has a

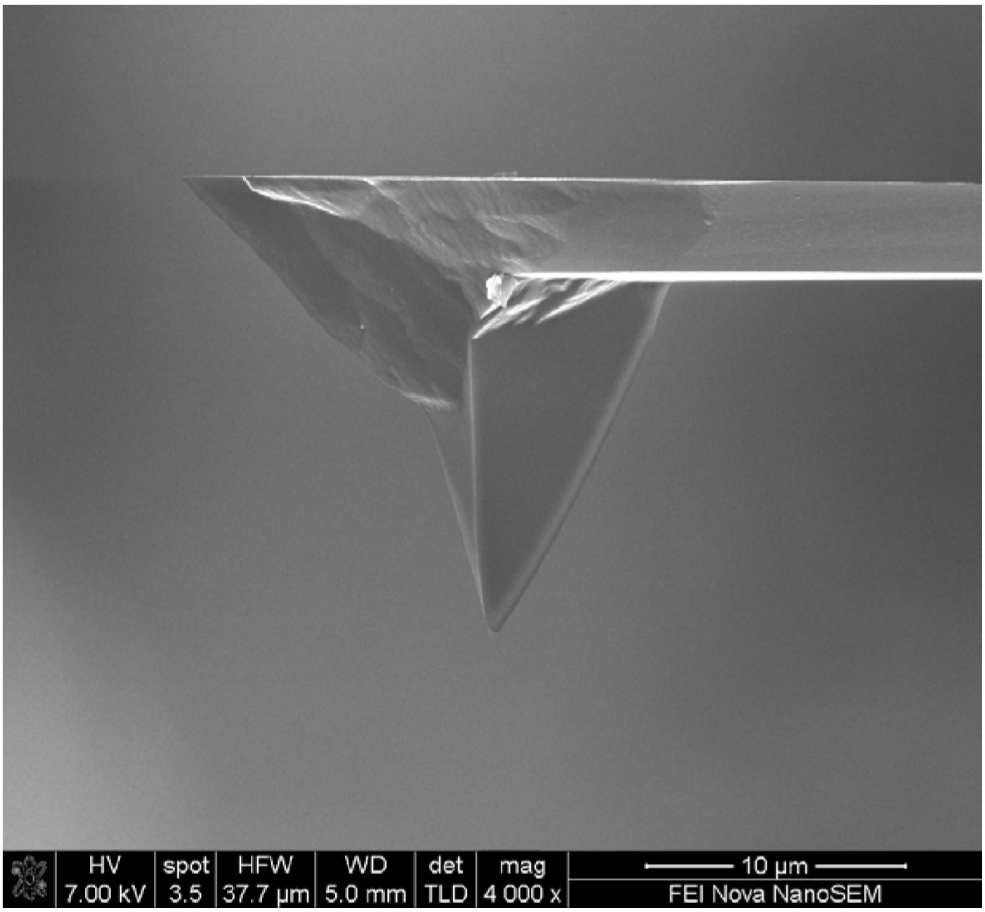

Figure 2.7 Scanning electron microscope image of a typical AFM (Si) tip.

thickness of ~70 nm, which is about double the penetration depth of gold for visible light.

2.9 Scattering from Gold Tip

The theoretical treatment of the scattering of light from a realistic shape such as an elongated tip is too complicated to solve analytically [63]. Over the years, there have been numerous numerical methods developed to compute the field distribution near scattering-type tips [7, 64-69]. For qualitative calculation, Hillenbrand showed that an elongated tip can be approximated by the sphere inscribed in its apex. This system is equivalent to an image dipole at the center of the sphere with the dipole aligned along the

tip axis [70].

The semi-infinite geometry of the tip does not support localized surface plasmon modes because the plasmon polaritons decay as they propagate away from the apex [71]. Due to the elongated geometry of the tip, the light scattering is polarization dependent, as illustrated in Figure 2.8. For a plane wave incident on a sharp gold tip with the polarization along the tip axis, a strongly enhanced near-field is observed at the apex of the tip (Figure 2.8b). In the case of incident wave perpendicularly polarized to the tip axis, the near-field at the apex is reduced (Figure 2.8a). Due to the symmetric geometry of the sphere, the near-field distribution rotates with the polarization, but does not change intensity.

As we discussed in the previous sections, the near-field distribution has some relation to the distribution of far-field scattered light. The scattered field from a sufficiently small (< 20 nm) nanosphere can be considered as radiation from an

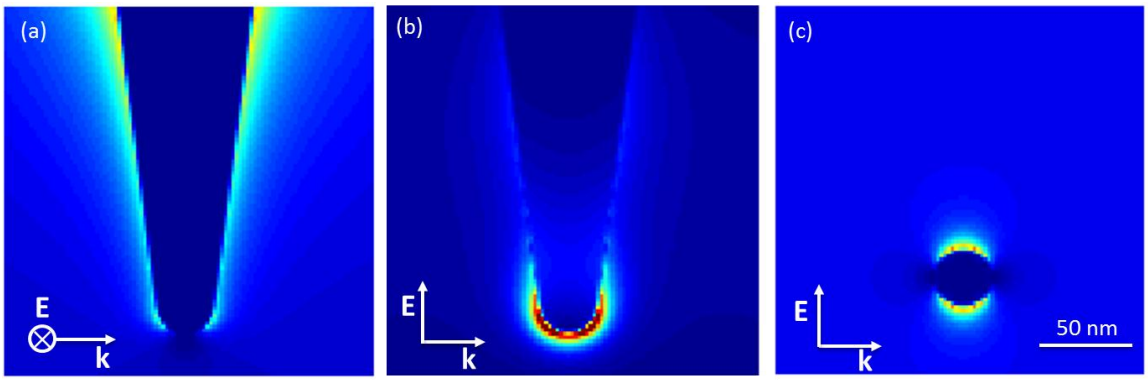

Figure 2.8 Near-field distribution with a plane wave excitation (λ = 605 nm). Conical gold tip with (a) polarization perpendicular and (b) polarization parallel to the tip axis. (c) Spherical gold particle. The tip and sphere have a 15 nm radius with a full cone angle of 15 degrees for the tip. The intensity in Figure (a) and (c) is enhanced six times more than the intensity in (b) for visual clarity.

oscillating dipole; in fact, the near- and far-field distributions from a small nanosphere are very similar to that from a point dipole (c.f. 2.8(c) and 2.2(a)). In contrast to a nanosphere, the near-field distribution for a sharp tip depends very strongly on the polarization of the excitation light: the tip polarizability is predominately along the tip axis while the symmetric sphere is equally polarizable in all direction. Thus, while a small nanosphere can emulate a point dipole with any orientation, a sharp tip is most accurately represented by a vertically-oriented dipole.

More specifically, since the scattering and absorption response of any particle is related to its polarizabilty, we can approximate the tip with a simple model of a quasi-static sphere with an anisotropic polarizability tensor [72]. In this model, the dipole moment of the tip in the presence of an oscillating external field $\mathrm{E}_0(\omega)$ can be expressed as:

$$p(\omega) = \begin{bmatrix} \alpha_\perp & 0 & 0 \\ 0 & \alpha_\perp & 0 \\ 0 & 0 & \alpha_\parallel \end{bmatrix} \mathrm{E}_0(\omega) \tag{2.23}$$

where $\alpha_\perp$ is the transverse polarizability (perpendicular to tip axis) of the sphere that inscribes the tip apex (given by Equation 2.19) and $\alpha_\parallel$ is the longitudinal polarizabilty of the tip (parallel to tip axis), which is related to the field enhancement along the tip axis. For a tip with a radius of 15 nm, based on FDTD simulation for the wavelength of 605 nm, $\alpha_\parallel$ is an order magnitude higher than $\alpha_\perp$ (ratio of maximum intensity enhancement between tip and sphere ~100).

So far, we have discussed the gold tip in free space. However, the near-field distribution is modified due to the presence of the sample and substrate on which the sample is lying. A numerical approach must be used to study the influence of the surface.

The modification of the local field in the presence of the surface modifies the polarizability of the tip and the surface, which is known as *effective polarizabilty*. It has been shown that the effective longitudinal polarizability of the tip gets enhanced due to presence of a dielectric surface near the sharp tip [66].

2.10 Near-Field Scattering from Gold Tip

As we discuss in the previous section, when a plane polarized light is incident on the sharp tip, the scattering from the elongated tip is polarization-dependent. It is very interesting to see how the tip behaves as if a tip is placed in the near-field of an emitter instead of a plane wave excitation. The near-field of an emitter constitutes both radial and transverse electric field (Equation 2.4 and 2.5). Depending upon the orientation of emission dipole and tip, the tip will experience electric near-field both in longitudinal and transverse direction of the tip axis. However, the elongated tip is mainly polarized parallel to the tip axis as compared to perpendicular to the tip axis. Thus, the scattered field from the tip mainly consists of dipolar field along the tip axis as it is represented by the schematic Figure 2.9a. Furthermore, the far-field radiations consist of both scattered light and emitted light from the source. The details of detected signal at the far-field due to the source field and scattered field are discussed in Appendix B.

In the strong coupling region ($d \ll \lambda$), the far-field radiation is dominated by scattered field from the tip. As the tip moves away from the dipole (intermediate coupling region), the emission from the dipole source is also directly radiated in the far-field and superimposed with the scattered field from the tip. At a particular distance, the far-field radiation consists equally of the field from the source dipole and scattered field from the tip. The superposition of these two fields could result in modification of angular emission

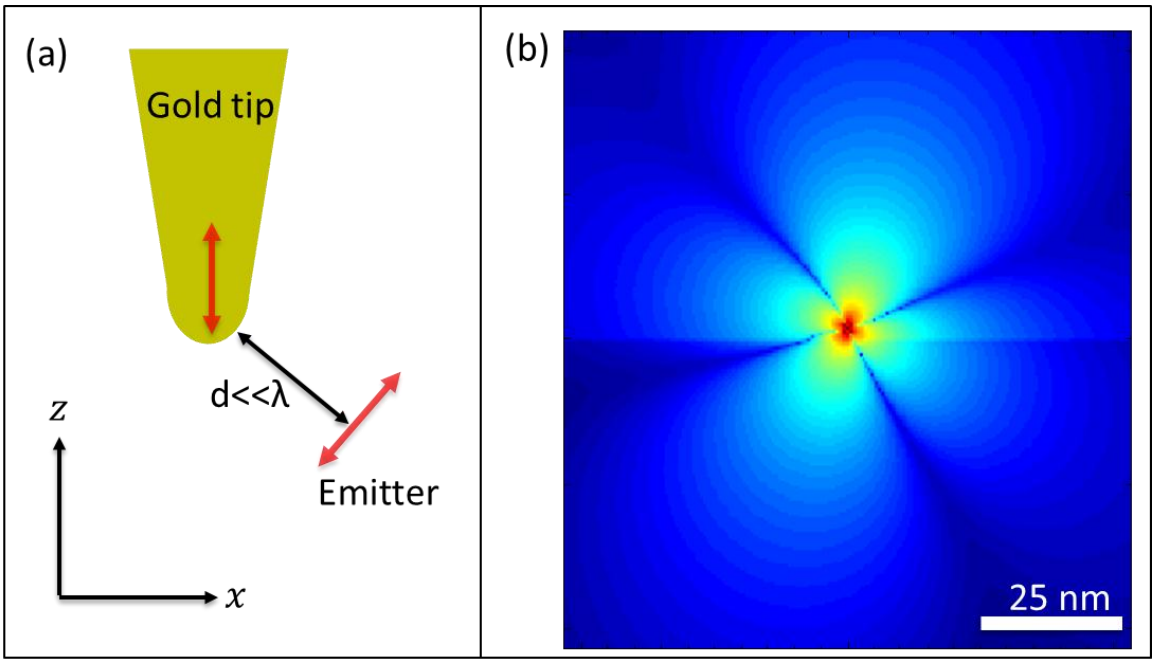

Figure 2.9 Near-field scattering. (a) Schematic of near-field interaction between an emitter and a sharp tip. Even though the emitter in the near-field consists of both radial and spherical electric field, mainly the field parallel to the tip axis will couple to the tip. This coupling creates an effective dipole along the tip axis. (b) The electric field component ($\log|E_z|$) for a 45^o dipole in the *xz*-plane. *z*-axis is aligned with the tip axis. The dipole is situated 2 nm above the air/glass interface.

and emission polarization, which is discussed in details in Chapter 5. As the tip moves further, the scattered field is weak (weak coupling region), so the far-field radiation is dominated by the source dipole.

For a sharp gold tip with semi-infinite geometry, the strong coupling region is within a few nanometers from the dipole source. As the near-field decays rapidly ($E \propto 1/r^3$), the intermediate coupling region where both source field and scattered field compete with each other is within ~10-40 nm. Beyond the intermediate region, the emitter field weakly couples to the tip. The scattered field from the tip depends on the polarizability of the tip (Equation 2.23) and polarizability depends on the wavelength of light. Thus, coupling distance (strongly, intermediate, and weakly coupled region) also

depends on the wavelength of light. Wavelength-dependent coupling is well illustrated in Section 5.4.4 of Chapter 5 of this dissertation. Besides that, the orientation of the dipole relative to the tip also determines the coupling distance as the effective polarizing field from source dipole is strongly varying in the near-field. For example, Figure 2.9b shows the E_z component for a 45^o dipole from the vertical direction. For the tip aligned along the *z*-axis, E_z component of the dipole field will contribute to polarize the tip along the tip axis. Since the sharp tip will experience strongly varying E_z field in the near-field, the coupling distances depend on relative tip-dipole position and orientation. Tip-dipole coupling as the function of dipole orientation is illustrated later in the Section 6.2.

2.11 Controlling Light with a Sharp Metallic Tip

Coupling a nanostructure to the near-field of an emitter or vice-versa is a way to increase the light-matter interaction in the nanoscale. In this next section, I will discuss how a sharp metallic can be used to manipulate, enhance, or modify the emission process from a quantum emitter.

2.11.1 Excitation and Emission Rate Enhancement

Below saturation, the emission rate of photons from a single emitter is proportional to the absorption rate of excitation photons. The experimentally measured total signal (photons) in the absence of a tip can be expressed as:

$$S = C\,\Gamma_{exe}\eta_i \tag{2.24}$$

where C is the collection efficiency of the system (i.e., the fraction of collected photons relative to total photons emitted), Γ_{exe} is the excitation rate, and η_i is the intrinsic quantum yield.

For a dipole emitter, $\Gamma_{exe} \propto |\mathbf{p} \cdot \mathbf{E}|^2$ where $\mathbf{p}$ is the dipole moment of the emitter and $\mathbf{E}$ the applied electric field at the location of the emitter. The intrinsic quantum yield can be expressed as:

$$n_i = \frac{\gamma_r}{\gamma_r + \gamma_{nr}} \tag{2.25}$$

where γ_r is the radiative rate of the emitter and γ_{nr} is the nonradiative rate (loss) within the emitter. Due to presence of a sharp metallic tip, both the excitation and emission rate is modified. The total experimentally measured photon signal (Equation 2.24) in the presence of a sharp metallic tip can be expressed as:

$$S' = C'\Gamma'_{exe}\eta' \tag{2.26}$$

where C' is the modified collection efficiency, Γ'_{exe} is the modified excitation rate, and η' is the quantum efficiency of the tip-emitter system.

If we detect all the emitted photons from the system, we can neglect the collection efficiency terms in the Equation 2.24 and Equation 2.26. Depending upon the excitation condition, a sharp metallic tip can have a strong local electric field at the tip apex (lightning rod effect), which can enhance the excitation rate by $k_{en} = \Gamma'_{exe}/\Gamma_{exe}$. Numerical simulations have shown that the excitation intensity enhancement is up to 3000 for a metal tip [73]. The modified quantum yield of a tip-emitter system can be expressed as:

$$n' = \frac{\Gamma_r}{\Gamma_r + \Gamma_{nr}} \tag{2.27}$$

where Γ_r is the modified radiative rate and Γ_{nr} is the modified nonradiative rate (which

takes into account various loss mechanisms, including energy transfer to the metallic tip, the intrinsic nonradiative relaxation of the emitter, etc.). We discussed the mechanism for modification of decay rate in Section 2.2.

The nonradative rate (Γ_{nr}) is the sum of loss rate Γ_{tip-nr} of the tip and intrinsic loss rate of the emitter γ_{nr}, i.e., $\Gamma_{nr} = \Gamma_{tip-nr} + \gamma_{nr}$. Substituting γ_{nr} in Equation 2.27 from Equation 2.25, the modified quantum yield of the tip-emitter system is related to the intrinsic quantum yield with the following relation:

$$\eta' = \frac{\Gamma_r/\gamma_r}{\Gamma_r/\gamma_r + \Gamma_{tip-nr}/\gamma_r + 1/\eta_i - 1} \tag{2.28}$$

For an emitter with $\eta_i = 1$, no intrinsic loss, the modified quantum yield reduces to:

$$\eta' = \frac{\Gamma_r}{\Gamma_r + \Gamma_{tip-nr}}. \tag{2.29}$$

Due to presence of losses within the metal tip, the modified quantum yield (η') is less than unity. However, for low η_i, the modified quantum yield can be effectively increased [74]. Again if the tip has excitation enhancement (k_{en}), the overall signal can be even enhanced. Since the modified quantum yield depends on the radiative rate enhancement Γ_r/γ_r and loss rate within the tip, Γ_{tip-nr}/γ_r, the overall signal can be enhanced or quenched depending upon which factors dominate. Due to strong loss mechanisms (short-range FRET-like energy transfer and long-range propagating surface plasmons polariton) in a semi-infinite gold tip, the overall signal gets mainly quenched as the tip approaches an emitter [71].

2.11.2 Control of Direction

The angular emission of a dipole emitter in a homogeneous medium covers a wide range of solid angle and is isotropic in the plane perpendicular to the dipole orientation (Figure 2.2c). The presence of a metallic probe in the near-field of an emitter modifies the angular emission pattern [12, 15, 16, 18]. With the proper coupling of an emitter to a nanostructure, we can direct the emission to a narrow range of solid angles to enhance the collection efficiency of the system.

The measurement of directional radiation pattern in terms of power density is termed directivity and calculated as:

$$D(\theta, \phi) = \frac{4\pi P(\theta, \phi)}{\int P(\theta, \phi) d\Omega} \tag{2.30}$$

where the angles θ and ϕ represent the polar and azimuthal observation direction, respectively [10]. The directivity is 1 for an isotropic emitter. For a dipole in a free space, the maximum directivity is 1.5.

Another way of quantifying asymmetries in the emission/radiation pattern is by calculating directionality. Directionality is defined as the ratio of the power emitted in a direction of maximum emission to the power radiated in the diametrically opposite direction:

$$D = 10 \log\left(\frac{P(\phi_{max})}{P(\pi + \phi_{max})}\right). \tag{2.31}$$

The directionality is used when the emission in only measured in one half space, e.g., the back-focal plane of a microscope objective, as shown in Figure 2.10. The detail of

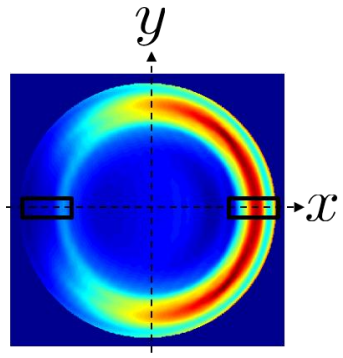

Figure 2.10 Directionality measurement on a back-focal image. The intensity ratio between two diametrically opposite directions in the back-focal image are related to directionality using Equation 2.31.

directionality and back-focal image is discussed in Section 5.4.2 later in Chapter 5.

2.11.3 Control of Polarization

The polarization of an emitter depends on the relative orientation of a dipole to the observation direction. The near-field coupling of an emitter to a sharp metal tip modifies the emission polarization in both near- and far-field. In the strong coupling region, the far-field polarization is dominated by the "tip" (or antenna) mode [12, 75]. In the near-field, a sharp metal tip can convert one polarization state into another local polarization of the evanescent fields. The relative orientation and position of the tip to the emitter have a significant role in determining the polarization state in the far-field. The detail of polarization control is discussed in Section 5.4.1 later in Chapter 5.

2.12 Optical Antennas

Antennas are used mainly in radio and microwave regions to manipulate electromagnetic fields, controlling them on the subwavelength scale and interfacing efficiently between propagating radiation and localized fields [76]. In analogy to the radio or microwave antenna, optical antennas are defined as a devices that efficiently localize

the propagating optical radiation into the subwavelength region or vice versa [10, 77].

Many studies are currently dedicated to adapting established radio and microwave antenna theories into the optical region. Some difficulties arise since the electrical and optical properties of metals at nanometer scales and at optical frequencies are different compared to lower frequencies and macroscopic sizes. The penetration depth of a metal can be of the same order magnitude as the antenna size at optical frequencies, so that for a particular frequency/wavelength, the resonance condition occurs for shorter antenna lengths. Javier Aizpurua and co-workers have shown that the length of a linear dipole antenna is significantly shorter than predicted for an ideal conductor using classical antenna theory [78].

Recent research in near-field optics and plasmonics has generated substantial interest in the optical antenna. Many different optical antenna geometries have been theoretically proposed and (due to improvement in fabrication abilities) many have recently been experimentally demonstrated [11, 21, 79, 80]. An example of bowtie antenna is shown in Figure 2.11 which was fabricated in P. James Schuck's group at Lawrence Berkeley National Laboratory.

By coupling an emitter to an optical antenna in the near-field, the emitter interacts with light through the antenna mode. The properties of the emission are thus determined by the antenna mode. If an optical antenna does not support plasmon resonances, the emission properties can be dominated either by the emitter or the antenna, or both contribute equally depending on the coupling strength.

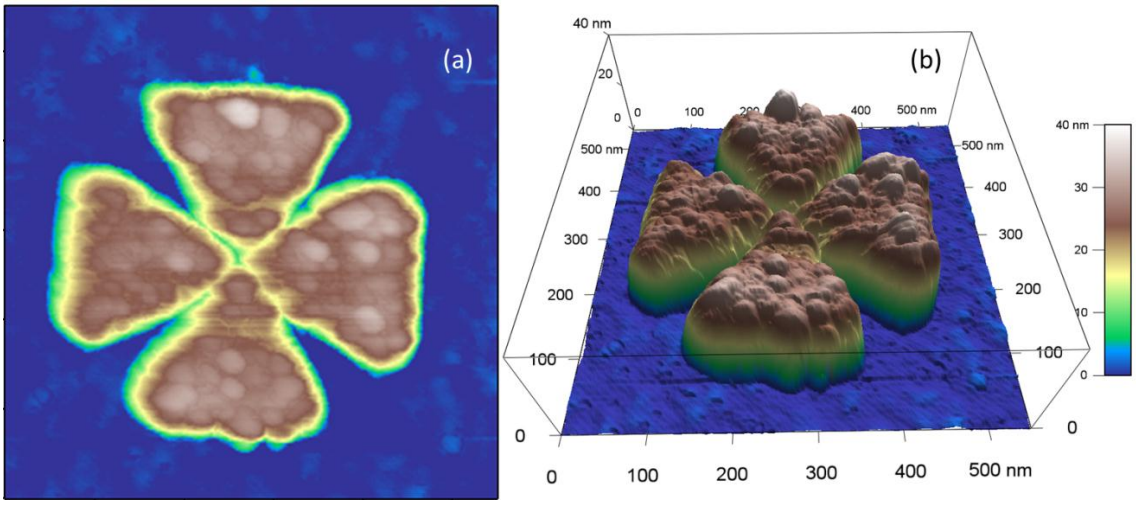

Figure 2.11 An example of an optical antenna. The bowtie antenna was fabricated at Lawrence Berkeley National Laboratory by James Schuck's group. An AFM scan was performed in our lab using a single carbon nanotube tip. (a) and (b) are the 2D and 3D images of the same bowtie, respectively. This unique design enables for nano scale color-sorter and for steering of optical fields [81, 82].

CHAPTER 3

EXPERIMENTAL SETUP

Near-Field Scanning Optical Microscopy (NSOM) is a technique that deals with the interaction between light and matter of the nanometer scale. Near-field refers to the length scales associated with the structures that are much smaller than the diffraction limit ($\lambda/2$).

Over the years, the microscope system in our lab has been modified for multipurpose use, adding functionality for different microscopy tasks while also adding complexity to the system. We have the ability to use an inverted confocal microscope for both sample scanning and laser scanning. The Atomic Force Microscope (AFM) can be operated independently or along with a scattering type Near-Field Scanning Optical Microscope (s-NSOM). Moreover, with small modifications to the detection path, we can use our system for back-focal imaging as well as hyper-spectral imaging. To understand the different modes of operation in our system, one should have a broad knowledge of near-field optics.

In this chapter, I will explain the basic layout of a near-field optical scanning microscope and then briefly characterize its uses as an inverted confocal microscope and atomic force microscope (AFM). Since the excitation scheme plays a significant role in the production of a near-field signal, the different illumination conditions are comparatively discussed. I will also discuss the alignment of an AFM tip and laser within

the diffraction limit of a confocal focal spot, which is the key to data collection in the near-field. At the very end of this chapter, the different detection schemes – polarization anisotropy measurements, back-focal imaging, and hyper-spectral imaging – are discussed.

3.1 Basic Setup

Our NSOM consists of two microscopes; an AFM and a confocal microscope, as shown in Figure 3.1. The AFM is a commercial system manufactured by Asylum Research. The confocal microscope was designed and built in our lab, and sits underneath the AFM system. Both the AFM and scanning stage of the confocal system are computer controlled using software developed by Asylum Research. I will discuss the AFM system and confocal system separately.

3.1.1 AFM System

The AFM includes an AFM head with a high precision piezo-actuated *xy* scanning stage. A cantilever (AFM tip) is attached to the AFM head, which vibrates vertically and additionally can be positioned vertically above a sample surface using two independent piezoelectric actuators. Most commercial cantilevers or scanning probes can be used in our AFM system.

Figure 3.2 shows a schematic of an AFM system. A sharp-pointed tip protrudes at the apex of the cantilever to scan surfaces. The cantilever moves in a vertical direction and the scanning stage moves in a lateral direction. With these two directional motions, we have a complete 3D scanning system. A laser reflects on the back of the cantilever at the far end of the cantilever arm. Most of the cantilever is coated with metal (Au, Al) to create a highly reflective surface. The laser reflected from the cantilever reaches a

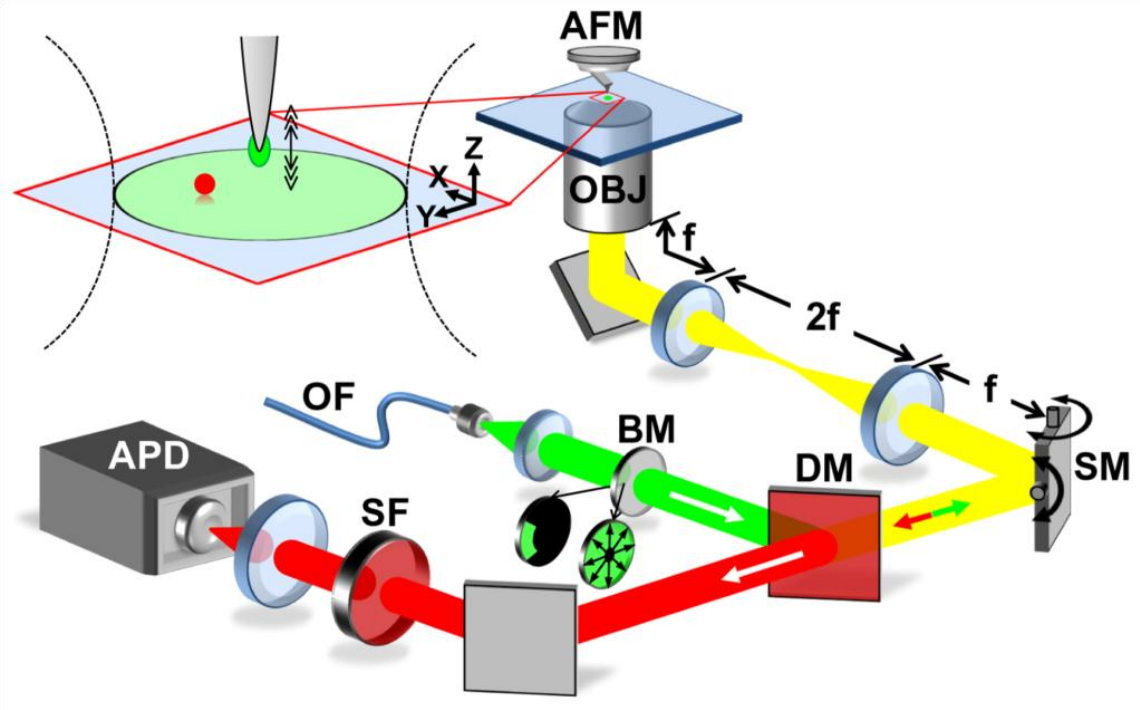

Figure 3.1 An experimental setup for the fluorescence near-field optical microscope. An excitation beam is decoupled through an optical fiber (OF) and gets collimated. Then, it goes through a beam mask (BM) in either a wedge or radial configuration. The excitation beam gets reflected by a dichroic mirror (DM), followed by a scanning mirror (SM), before being focused through a microscope objective (OBJ). The emission signals from the sample are collected back through the yellow path and directed onto an avalanche photodiode (APD) via red path. The emission is spectrally filtered using an appropriate spectral filter (SF).

quadrant photodiode (A, B, C, and D). The voltage recorded in each segment of the photodiode is proportional to the intensity of the laser that falls on it. The total voltage ($V_A + V_B + V_C + V_D$) is called the sum signal. A larger sum signal will impart better sensitivity to the movement of the cantilever. The reflected laser beam is configured as an optical lever so that even a small deflection on the cantilever leads to a measurable displacement of the laser spot on the quadrant photodiode. The difference of voltages ($V_A + V_B - V_C - V_D$), also called the deflection signal, measures the movement of the tip in a vertical direction. Due to its phenomenal sensitivity, an AFM is very useful tool to

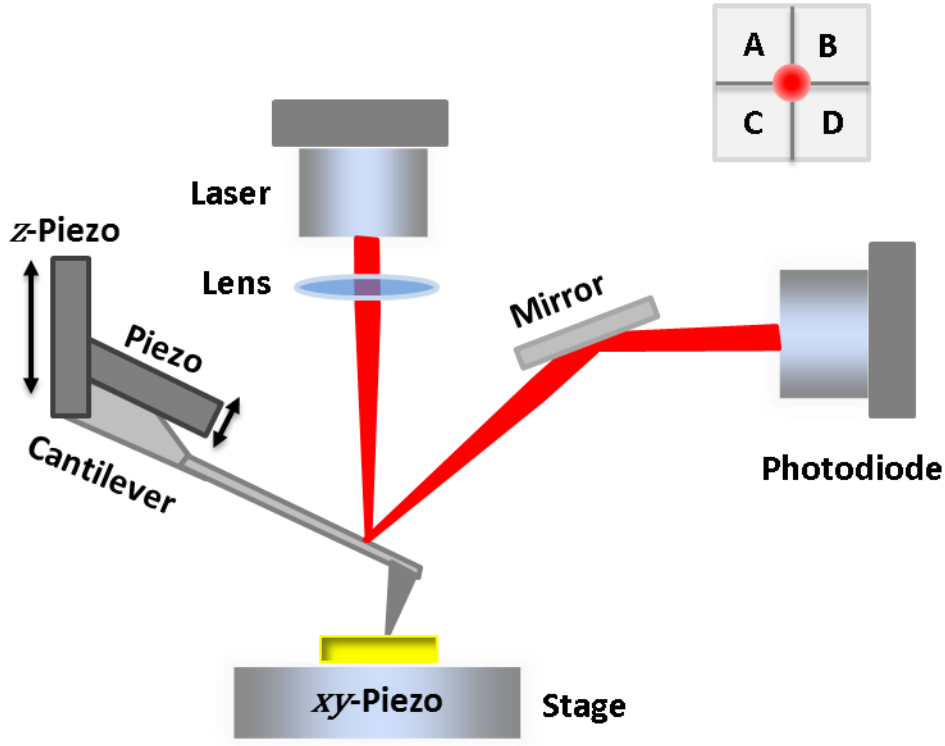

Figure 3.2 Schematic of AFM system. A deflection laser is reflected on the back of the cantilever and reaches to a sensitive photodiode. The photodiode has four detector segments as shown in the inset. These segments are labeled A, B, C and D. The cantilever is attached with two piezoelectric actuators. One piezo will create oscillation on the cantilever and other will moves the whole cantilever in vertical direction.

measure the atomic-scale interaction forces between tips and the sample surface, and it can also be used to map/record the detailed surface morphology with high precision limited primarily by the sharpness and shape of the tip. AFM is shown to be robust to differentiate the surface morphology of very thin layers (~10 nm) of different samples [83].

Primarily, AFM is operated in two different scanning modes: contact mode and tapping mode (also called AC or intermittent contact mode). In contact mode, the tip is in contact with the surface with a constant force while the stage is scanned to measure the topography of the surface. In contrast, for tapping mode, the cantilever is driven near its

resonance frequency and the motion of the tip is described by a simple harmonic oscillator. During tapping mode, the tip is lowered to the surface and driven to oscillate with a specified amplitude using the AC voltage from the quadrant photodiode to define a particular set point. The oscillation amplitude in volts can be converted into a physical oscillation amplitude with proper calibration.

Tapping mode is more advantageous for our studies than contact mode. In tapping mode, the tip is less damaging to the sample as it intermittently contacts the sample during oscillation. More importantly, we can study the optical contrast as a function of the tip-height above the sample plane. Combining tapping mode with the *xy* scanning stage and the confocal microscope enables us to study the optical interaction between the tip and the sample in the 3D space above the sample plane.

3.1.2 Confocal Microscope

The confocal microscope system was designed and assembled in the laboratory and sits just beneath the AFM. The excitation path in the optical train is portrayed as the green path, as shown in Figure 3.1. The excitation laser is outcoupled from a single-mode, polarization preserving optical fiber and subsequently collimated using a microscope objective lens ($10\times$, NA 0.25). The collimated beam passes through various optics such as a polarizer, a wave-plate, a wedge-shaped beam mask, etc. to produce different excitation/illumination conditions. The excitation laser is reflected by the dichroic mirror and then a scanning mirror. The excitation light is focused by a high numerical objective lens (NA = 1.4) onto the sample plane. In between the scanning mirror and the objective lens, there are two identical achromatic lenses separated by the sum of their focal lengths (f_0). The scanning mirror and the back-focal plane of the

objective are positioned one focal distance from either lens so that the total length between the scanning mirror and the back-focal plane of objective is ($4f_0$). With this arrangement, the plane of the scanning mirror is conjugate to the back-focal plane of the objective.

A schematic ray diagram for a ($4f_0$) scanning system is shown in Figure 3.3. When the scanning mirror is at a $45°$ degree angle relative to the optical axis, the light follows the path shown by the red lines. As the scanning mirror tilts slightly, the excitation path is deflected, and the light follows the path indicated by the green lines, leading to a small displacement of the excitation spot. In practice, we use a labview program to move the scanning mirror in a controlled way so that we can raster scan the excitation spot on the sample. Since light rays obey the reciprocity theorem, the emission coming from a particular excitation region will retrace the same path. This $4f$ arrangement ensures that the optical signal emitted from the confocal excitation volume is "descanned" once it reflects from the scanning mirror, thereby allowing for a single-pixel (pointillist) detection system such as a photon counting module, i.e., an avalanche photodiode (APD). The emission is separated from the backscattered/reflected excitation light using a dichroic mirror and specific spectral filters.

3.2 Types of Illumination

The excitation polarization plays an important role in our experimental measurement. Since our near-field tip (the AFM tip) is elongated in a vertical direction, vertically-polarized excitation light induces a polarization of the tip along its axis, which typically results in strong field enhancement at the apex [4, 5, 72, 84]. On the other hand, when the excitation light is polarized perpendicular to the tip axis (see Section 2.9), there

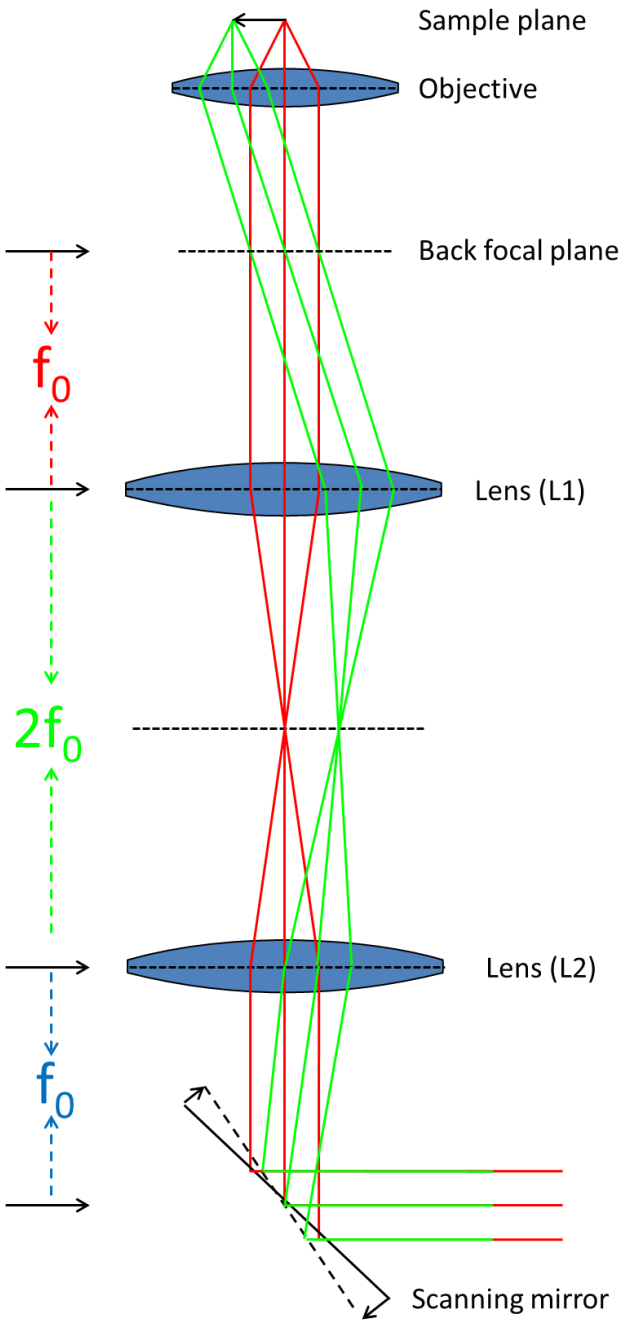

Figure 3.3 Schematic of ray diagram for a 4*f* scanning system. Two identical lenses (L1 and L2) are separated by $2f_0$ distance, f_0 being the focal distance for each lens. The L2 lens is f_0 distance from the center of the scanning mirror, and the L1 lens is f_0 distance from the back-focal plane of the objective lens. The red lines represent the ray diagram for the excitation/emission light in the $4f_0$ system. The green lines represent the same ray diagram when the scanning mirror is tilted slightly in one direction.

will be no field enhancement, and there might even be a reduction of field intensity [1]. The shape of the excitation focus at the sample plane can also alter the near-field optical signal. In the following section, I will discuss the two illumination conditions utilized in our system, Gaussian, and Wedge for the basic physics and their potential application in microscopy.

3.2.1 Gaussian Illumination

Most commercially available lasers produce the fundamental transverse mode, also known as the TEM_{00} mode. The TEM_{00} mode has a Gaussian beam profile. If conventional optics are utilized, a Gaussian source distribution remains Gaussian at every point along its path of propagation through the optical system since the Fourier transform of a Gaussian is another Gaussian; only the width and the amplitude of the Gaussian function are modified. The time-averaged intensity distribution of the Gaussian beam is defined by the following equation:

$$I(r,z) = I_0 \left(\frac{\omega_0}{\omega(z)}\right)^2 exp\left(-\frac{2r^2}{\omega(z)^2}\right) \tag{3.1}$$

where I_0 is the intensity at the beam waist (ω_0) and $\omega(z)$ is the beam diameter at the axial distance z.

The light from a laser source is coupled into a polarization maintaining single mode optical fiber using a fiber incoupler. The laser emerging from the other end of the fiber is strongly divergent. It is collimated by placing a short focal length lens at the output of the optical fiber. In our lab, we use a microscope objective lens (Olympus 10x) as an outcoupler. The objective lens is positioned on a linear translational stage and the

optical fiber is placed in an *xy*-stage so that the beam emerging from the back aperture of the objective is fully collimated and directed parallel to the optical table. The advantage of using a relatively achromatic compound objective lens rather than a conventional lens is that the output collimation is preserved for a broad range of wavelengths.

The diameter of the output beam is determined by the numerical aperture (NA) of both the fiber and objective lens for the particular wavelength. To adjust the beam diameter for different wavelengths, a couple of achromatic doublet lenses are used. The beam size is adjusted to overfill the back aperture of the microscope objective. I will discuss in detail the importance of overfilling the back aperture in Section 3.2.2.

We use an oil immersion objective with a high numerical aperture (NA=1.4, 100x), which is capable of focusing light to a very tight spot; the effective focal length of the objective is short (2 mm). Due to the high converging capability of the microscope objective, the focal spot contains a mixed polarization even though the linearly polarized light is focusing through this objective. The beam profile at the focal plane of an objective with NA = 1.4 and an index of refraction for the medium (glass) of $n = 1.518$ is shown in Figure 3.4. While the incident light is polarized solely along the *x*-axis, the focus spot contains components along the *x*, *y* and *z* axes. The intensity of electric field components *y* and *z* are multiplied by 256 and 8, respectively, to create a color scale similar to that of component *x*. The incident light is absorbed most efficiently by a molecule when the polarization of light aligns with the orientation of the absorption dipole moment of the molecule (Excitation rate $\propto |\boldsymbol{p}.\boldsymbol{E}|^2$). Using a high NA objective with the linearly polarized light, it is always possible to excite an emitter with all possible dipole orientations. It is interesting to notice that with increasing field confinement at the

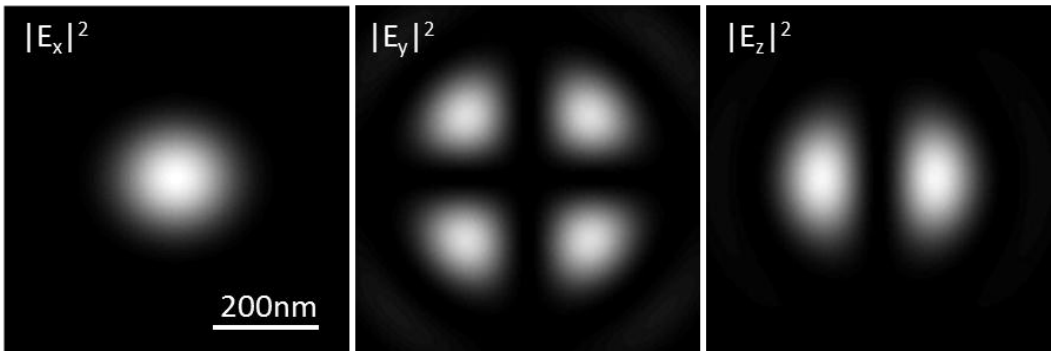

Figure 3.4 The intensity of the Gaussian beam at the focal plane (*xy*-plane) for NA = 1.4, n = 1.518. The intensity scale for *y* and *z* components is magnified by 256 and 8 times, respectively. The incident light is polarized along *x* direction before focusing.

focus, the focal spot becomes more and more elliptical. The focal spot is elongated in the direction of polarization. This can be well-illustrated in the diffraction-limited emission pattern for a sample of randomly oriented molecules, as shown in Figure 3.5.

3.2.2 Wedge Illumination

Wedge illumination utilizes the total internal reflection condition with the creation of evanescent field at the interface (see Appendix C for detail). This condition is easily achieved for some portion of the converging light through a high NA objective. For an objective with NA $=$ 1.4, the maximum incident angle for the excitation beam is given by the relation:

$$NA = \eta \sin \theta_{max} \tag{3.2}$$

For the glass/air interface ($\eta = 1.5$), the calculated θ_{max} is 68.96^o. The light incident in the range of $\theta_c > \theta > \theta_{max}$ will be totally internally reflected with creation of evanescent field at the interface.

To get the maximum incident angle for an objective, the back aperture of an

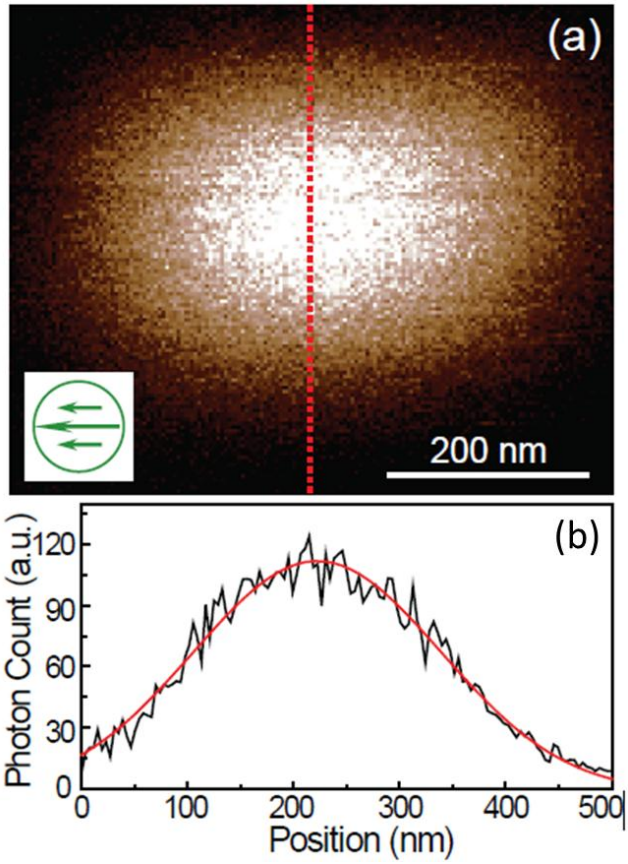

Figure 3.5 Fluorescence image of a 20 nm polystyrene bead under linearly polarized Gaussian mode. The focal spot has a Gaussian profile with elongation along the polarization direction. The black line in (b) is the intensity profile across the red dotted line from (a). The red continuous lines in (b) are the fitted Gaussian function to the data. Reprint with permission from reference [85] (© 2008 IEEE).

objective has to be completely filled. The diameter of the back aperture of the objective can be calculated as:

$$D = 2\,f\,NA, \qquad f = f_{TL}/mag \tag{3.3}$$

where f is the front-focal length, f_{TL} is focal length of the tube lens, and *mag* is the magnification. For an objective of NA = 1.4, *mag* = 100× and f_{TL} = 200 mm, the diameter of the back-focal aperture is calculated to be 5.6 mm. Using Equation 3.2 and 3.3, we can

calculate the diameter of the back aperture corresponds to critical angle as:

$$D_c = 2\, f\, \mathrm{NA_c} \tag{3.4}$$

where $\mathrm{NA_c} = \eta \sin\theta_c$. Based on the definition of critical angle, $\sin\theta_c = 1/\eta$, $\mathrm{NA_c}$ should equal one. The calculated D_c equals 4 mm.

By avoiding the laser beam that passes through the center of the objective within 4 mm diameter, only the supercritical beam is allowed to incident on the glass surface, producing an evanescent field at the air/glass interface. However, the polarization of the evanescent field will not be axial because the vertical components originating on the opposite side of the beam will cancel each other, resulting mainly in plane components on the surface [86]. To overcome this situation, a beam mask with 60^o degree opening is used to block the subcritical beam. The design of this beam mask is shown in Figure 3.6a. The 60^o opening angle ensures that there is a net vertical component at the focus for p-polarized excitation. For s-polarized excitation, only in-plane polarization exists at the focus on the sample plane.

In practice, the beam mask is made up of an opaque metallic plate. This metallic plate is precisely cut in a circular shape with a wedge-shaped window as shown in Figure 3.6a. The mask is placed in the excitation path and aligns at the center of the laser beam. By observing the power transmitted to the upper and lower portion of beam, as well as checking the symmetric pattern in the camera, we can iterate the position of the mask at the center of the excitation laser. Once the mask is placed at the center, one portion of the opening is blocked by an opaque object.

The main drawback to wedge-shaped beam excitation is that the power

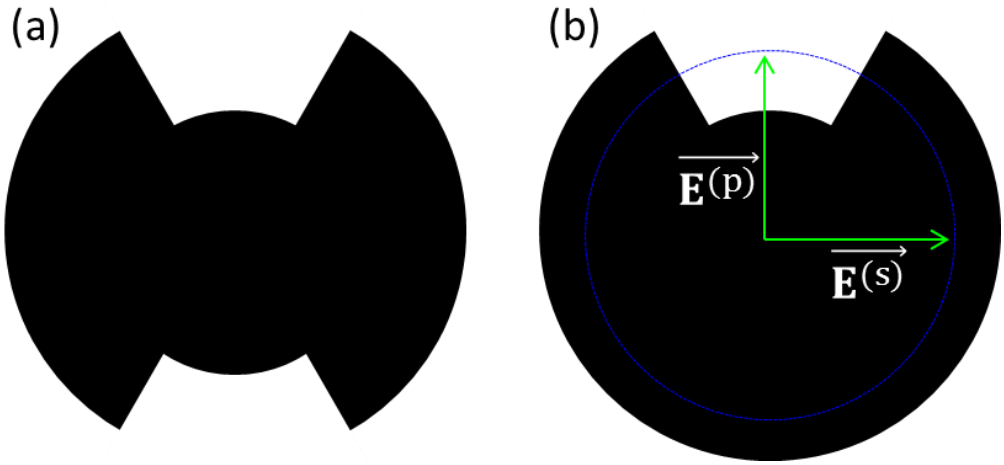

Figure 3.6 Design of beam mask for wedge illumination. (a) Wedge-shaped on both vertically opposite sides. (b) The blue colored ring corresponds to the size of the back aperture of the objective. The inner wedge curve corresponds to the critical diameter (Dc). The green arrows represent the polarization of light incidence on the beam mask. The polarization state (s- or p-polarized illumination) at the sample plane is determined by the polarization state at the beam mask.

transmitted through the small opening is very low for the Gaussian beam. The power transmitted through a circle of radius r is given by the expression:

$$P(r,z) = P_0[1 - exp(-2r^2/\omega^2(z))] \tag{3.5}$$

where $P_0 = 1/2\,\pi I_0 \omega_0^2$, the total integrated power over the beam profile. For a beam waist equal to the size of the back aperture $r = \omega(z) = D/2 = 2.3\,mm$, the total power transmitted without a beam mask will be $P = P_0[1 - e^{-2}] \approx 0.8647P_0$. The integrated power corresponding to the critical diameter $r_c = D_c/2 = 2\,mm$ is equal to $P = P_0[1 - e^{-2\times 2^2/2.3^2}] \approx 0.7796P_0$. The power transmitted from the 60° wedge opening is equal to $P_{wedge} = P_0/6[0.8647 - 0.7796] \approx 0.0142P_0$. As a result, only ~1.42% of total power will be used to excite the sample when a wedge-shaped beam is used. One easy way to increase the power in wedge excitation is to expand the beam size so that the

Gaussian beam profile is spread over a larger area. For example, when the beam waist is twice the size of the back aperture, the transmitted power from the same 60^{o} degree opening will be $\sim$12.91%, an order of magnitude higher in excitation power.

3.3 Tip-Laser Alignment

As we discussed in Section 3.1, our experimental system includes two microscopes, an atomic force microscope and the confocal microscope. The AFM tips are fabricated with the tip hidden below the cantilever, as shown in Figure 3.2. The AFM tips are very sharp, on the order of 10 nm diameter at the apex. We can see the edges of the cantilever from both the top and bottom optics and roughly estimate the location of the tip within 10-15 microns by looking at the manufacture's specification of the tip. Obviously, for accuracy, this estimation requires a lot of experience. The laser spot at the focus is on the order of $\sim$250 nm, but depending upon the excitation condition, this value may vary. The biggest challenge for our experimental measurement is to align the tip ($\sim$10 nm) with the laser focus ($\sim$250 nm). By looking at the tip from above and below, we can estimate the location of the tip apex within the uncertainty of 10-15 microns.

To achieve high precision alignment, the tip and laser are first coarsely aligned with top-bottom view optics. Then, we create a diffraction pattern by side illumination of a laser of wavelength 785 nm. This wavelength was chosen such that it is spectrally distinct from the AFM laser (860 nm) and is far enough in the red as not to interfere with other optical measurements typically performed in the lab. The side laser creates a very distinct diffraction pattern around the apex of the tip, as shown in Figure 3.7. The microscope objective collects both a diffraction pattern and the laser spot at the focus. A beam pick-off is inserted into the detection path to pick-up 4% of the light and is imaged

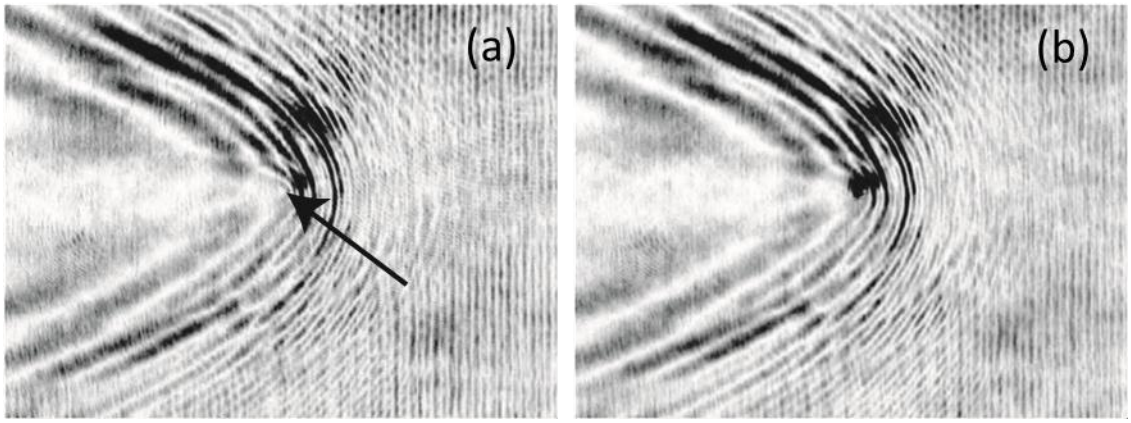

Figure 3.7 Diffraction pattern around the tip under side illumination captured from camera. (a) The arrow indicates the tentative location of the tip apex, which is estimated based on the pattern recognition. (b) The same pattern with the excitation laser (vertical wedge illumination).

by a camera. By overlapping the laser focus with the center of the diffraction pattern, the tip and laser are aligned within a few microns. This is as far as we can align the laser with tip without using sample as the reference.

To further the alignment, we need a reference sample. In general, we deposit a fluorescent sample (latex beads or quantum dot) onto the coverslip by drop casting method. The density of the sample is very dilute so as to allow 1-2 microns sample separation. We image the surface by both binning fluorescent photons and scanning topographically using the AFM. We first scan a large sample area ($\sim$20 μm^2) and look at only the fluorescence image. Then, we zoom into a region (2-3 μm^2) of less sample density to isolate an individual sample.

Next, we scan topographically to find the sample that corresponds to the fluorescent image. This detection can be tricky if there is more than one topographically similar structure seen in the image. Prior knowledge of the size of the sample is always helpful when attempting to identify the right sample. The tip is moved on the top of the

sample, using the piezo-controlled stage. While the tip is sitting on the top of the sample in the AFM image, the laser is raster scanned using the labview program across a few micron sizes to create the fluorescent image. Since the diffraction-limited fluorescent image of the sample is observed, we can manually move the laser to the center fluorescent image. We keep the AFM tip sitting just above the sample and we move the excitation laser to the same spot. In this way, we can align the tip and laser within the diffraction limit.

In practice, there is always the chance of choosing one sample in topography and choosing a different sample in the fluorescent image. This situation can happen more often if the density of the sample on the substrate is high. An optimal density to avoid confusion of the AFM image and fluorescence image is ~ 5 samples per 20 square microns. This sample-dependent alignment technique required the sample surface to be as contaminant-free as possible. Extra precaution has to be taken during sample preparation and cleaning the cover glass.

To make sure the alignment is perfect, we have to check the near-field effect. The AFM tip is allowed to oscillate directly on the top of the sample while the fluorescent signal is constantly monitored as a function of the tip-height. If there are near-field effects when the tip is close to the sample, we can monitor these effects by observing the fluorescent signal. In general, for a metal-coated tip, the fluorescent signal is reduced as the tip was lowered to the sample. For a silicon tip, the effect was either signal enhancement or reduction depending upon the excitation condition. Again, prior knowledge of near-field interaction is required to understand the nature of the signal while measuring the photon counts as the function of tip-height (approach curve). If there

are near-field signals, this effect proves that the tip and laser are aligned. In some cases, there may be not enough near-field effects; hence, a new sample-independent aligning technique is required to deal with this experimental condition.

The relative movement of the tip and laser can be accomplished independently in our system, enabling a feasible tip-laser alignment. The AFM head sits on the lower layer of the scanning stage, which can be moved with a pair of picomotor piezoelectric linear actuators. These actuators enable us to move the tip as well as the whole AFM head in the *xy*-plane with respect to the stationary laser. On the other hand, the scanning mirror can be used to move the laser focus on the sample plane with respect to the tip. The scanning mirror used in our system is a Fast-Scanning Mirror (FSM) manufactured by Optics in Motion. It is remotely controlled via a labview program. This mirror has an angular resolution of <2 µrads, which corresponds to a linear displacement of the laser by 4 nm on the sample plane. We have calibrated the scanning mirror system so that, for a desired displacement, a value is entered in the labview program that will deflect the mirror in a direction corresponding to a certain voltage ($10.2\ \mu m \leftrightarrow 1V\ \hat{x}, 14.57\ \mu m\ \leftrightarrow 1V\ \hat{y}$).

The scanning stage has two structural layers. The upper layer is the piezo controlled scanning stage, which moves relative to the second layer. The upper layer is controlled via the IgroPro software. This layer moves independently to the tip and laser; once the tip-laser is aligned, it will remain aligned as the stage is raster scanned. The maximum scanning area for our system is 90 µm × 90 µm. The alignment should be checked regularly as the thermal and mechanical drift destabilizes the alignment over time. Thermal drift depends on many factors, mainly the nearby environment. Running the scanning system for a while without taking actual data might help the system obtain a

stable condition. Experience will definitely help when troubleshooting a tip-laser that has fallen out of alignment. If the system is misaligned, we can realign it by following the sample-dependent alignment. More information regarding the tip-laser alignment can be found in [86].

3.4 Types of Detection

Light collected through the objective follows the same excitation path shown in Figure 3.8. The collected light includes fluorescent light from the sample, the AFM laser (860 nm), and the backscattered excitation laser. The side laser only needs to be turned on when aligning the tip and laser. The dichroic mirror reflects approximately 99% of the excitation laser while wavelengths longer than a cut-off frequency are transmitted. In the detection path, the AFM laser is filtered by an 810 nm short pass filter. Before the light reaches the detector, a beam pick up will reflect 4% of light into an imaging camera (Watec 902H3). A converging lens of focal length 200 mm (focal length of tube lens) is used for imaging so that the magnification (100× the objective) will be maintained. The image produced by the camera is displayed on a TV to allow us to monitor the laser focus. After the beam pickup, the light is mainly reflected from the mirror and sent to the detectors. Depending upon the experimental requirement and the nature of detector, we use a three-way detection configuration as described in the following sections.

3.4.1 Polarization Anisotropy Measurement

The fluorescence from an emitter, with a defined transition dipole, generates an emission pattern. The projection of this transition dipole on the sample plane determines the polarization of the collected light [87]. There are different ways to measure the

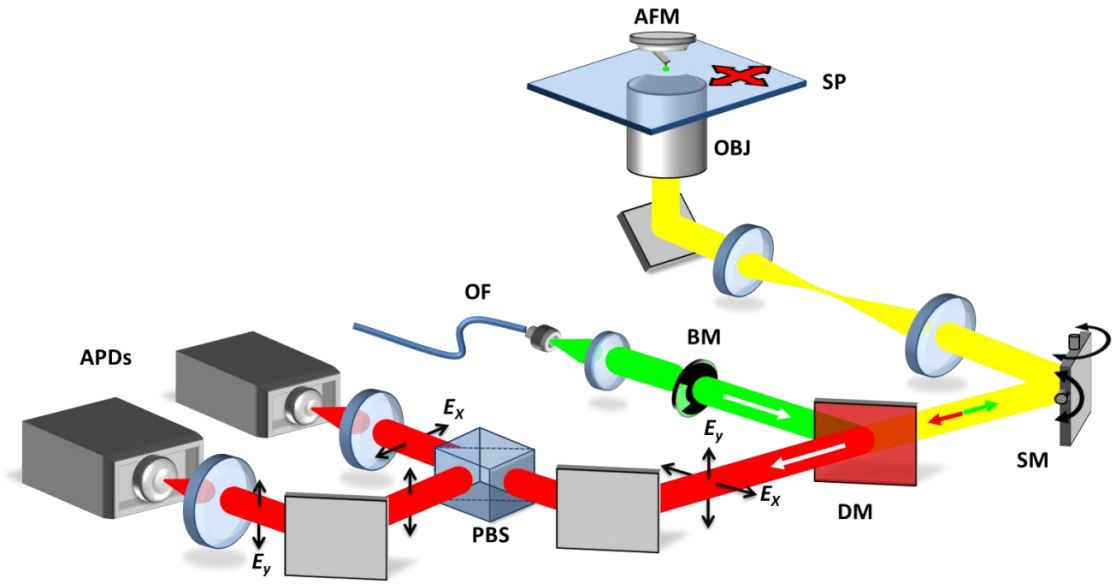

Figure 3.8 Experimental setup for polarization anisotropy measurement. After being spectrally filtered from excitation, the fluorescence signal is passed through the polarizing beam splitter (PBS). Each polarization channel is collected in identical APDs.

polarization anisotropy of the emission: a rotating polarizer or a polarizing beam splitter [88, 89]. The polarization beam splitter is used to implement the polarization anisotropy measurement in our lab. The schematic of the experimental setup is shown in Figure 3.8. The fluorescence in the detection path is incident to a polarizing beam splitter, which separates the emitted photons into two orthogonally (*x*- or *y*-) polarized emission channels. The normalized difference in two polarization intensities measures the polarization anisotropy. The fluorescence signal in each polarization path focuses at the core of multimode fiber using a lens with a focal length of +10 mm. The output of the multimode fiber is connected to the APDs for the purpose of time stamping. Reference [10] has details how each photon is time-stamped and correlated with the relative position of the tip and the sample.

3.4.2 Back-Focal Imaging

The rays that leave the object plane at the same angle of inclination meet on a plane at the back of the objective, as shown in Figure 3.9. This plane is named the back-focal plane. The back-focal plane is also known as the Fourier plane because the emission pattern at the back-focal plane is mathematically the Fourier transform of the object plane [90-92]. The back-focal image shows the angular dependence of the emission pattern [11, 93, 94]. In this detection scheme, the intensity pattern at the back-focal plane is directly recorded by a digital CCD camera. In the 4*f*-microscope system, the plane of the scanning mirror is a conjugated plane with the back-focal plane, as shown in Figure 3.3. If we image the plane of the scanning mirror, it will be the same as the back-focal plane of the objective. The microscope objective consists of many lens systems and locating the actual

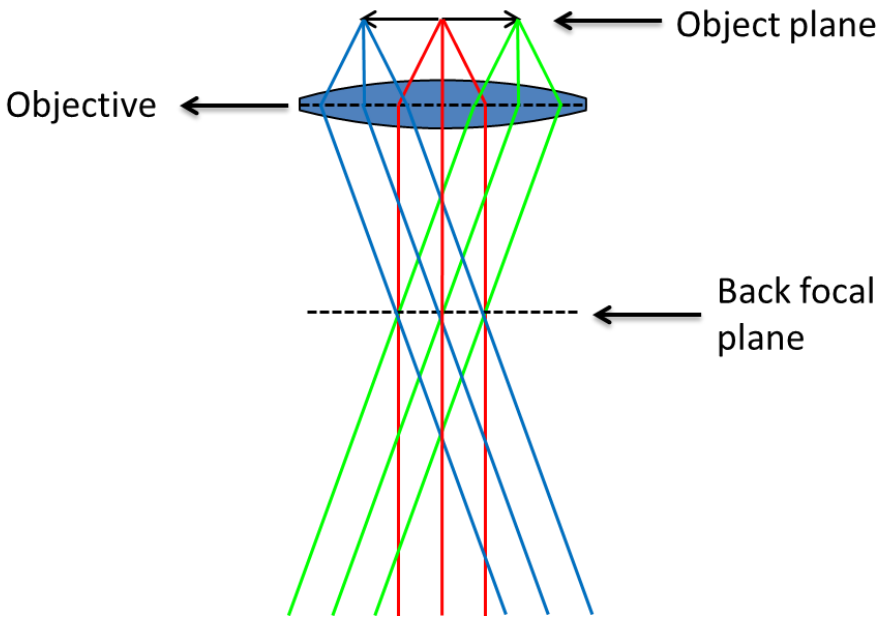

Figure 3.9 Schematic showing the back-focal plane (BFP) for an objective. For an infinity corrected objective, all the rays originating from the object plane at the same incident angle meet at the back-focal plane.

position of back-focal plane on these objectives can be quite difficult. Generally, it lies close to the back aperture of the objective. The objective we use in our lab, the Nikon plan APO 100× VC, has a back-focal plane at 47.55 mm from the front-focal plane including a 0.17 mm thickness of the cover slip. The distance from the face of the nosepiece to the back-focal plane is calculated by subtracting the 47.55 mm from Parfocal length (60.06 mm), as shown in Figure 3.10.

A lens with a focal length of f is positioned at 2f position from the scanning mirror. This allows the image of the back-focal plane to be recorded on the CCD chip at a distance of 2f from the lens with unity magnification. A flip mirror is inserted into the detection path in between the lens and the dichroic mirror (Figure 3.1). This flip mirror diverts the detection path from the confocal detection in the APD to the back-focal imaging system. The adjustment of optics is performed by putting a transparent target (with some pattern) at the exact location of the back-focal plane and imaging it on the camera. The fine adjustment focusing on the target's pattern can be done by attaching the translation stage to the camera or lens.

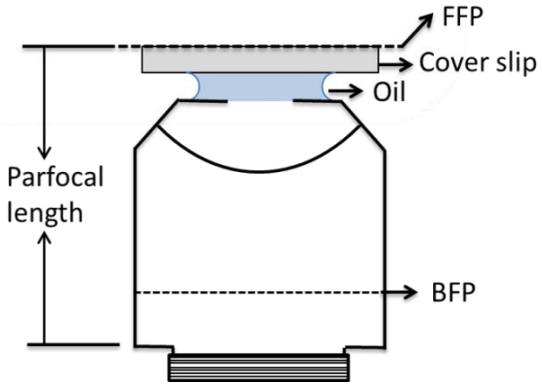

Figure 3.10 Schematic of an oil-immersion objective. The sample is placed on the front-focal plane (FFP). The distance between the nosepiece and the front-focal plane is the Parfocal length. The back-focal plane (BFP) lies near the back aperture of the objective.

3.4.3 Hyper-Spectral Imaging

An APD or CCD detects the photons, but the wavelength associated with each detected photon cannot be distinguished. For this reason, we put an appropriate spectral filter before these detectors. Spectrum resolved emission signal can be recorded using a spectrometer system. We have a spectrometer system with a fiber coupled input. In our general confocal setup (Figure 3.8), the polarizing beam splitter is replaced by a $50/50$ beam splitter. One channel of the detection path is connected to the spectrometer system while other channels are still connected to the APD.

Our AFM system was manufactured by *Asylum Research* and the spectrometer system was designed by *Princeton Instruments*. Each system is independent and controlled by its own software. While the AFM system raster scans pixel by pixel, the spectrometer system is synchronized with the AFM scanning system so that spectral data can be recorded on each pixel. Integrating the spectrum of interest on each pixel is equivalent to creating the fluorescence image using the APD with a given spectral band. The imaging system, which includes the spectrum information on each pixel, is known as hyper-spectral imaging [95]. The detail of implementation of hyper-spectral imaging is given in Appendix D.

CHAPTER 4

FINITE-DIFFERENCE TIME DOMAIN (FDTD) TECHNIQUE

4.1 Introduction

In recent years, the Finite-Difference Time Domain (FDTD) technique has been proven to be one of the most effective numerical methods to solve electrodynamics problems with arbitrary geometries. Kane Yee proposed this technique for the first time in 1996 [96]. As FDTD is a direct solution to the Maxwell's equations, it is easy and straightforward to calculate the electromagnetic field even in complex structures. The simulation domain is discrete in the spatial grid and electromagnetic field quantities are solved in each grid by propagating a wave in the time domain. As FDTD is a time domain solver, a single simulation can be done for a wide range of frequency bands at once. Due to its use as a dynamic computational tool, FDTD has been implemented in many applications, including microscopy, nanophotonics, plasmonics, metamaterial, and nonlinear optics. In this chapter, I will discuss the FDTD formalism, boundary conditions, and near-field to far-field projection in detail.

4.2 FDTD Formulation

The FDTD technique is a numerical solution of the time-dependent Maxwell's equations. To understand how the algorithms work, we will begin with the time-dependent Maxwell's equations without a source [31]:

$$\frac{\partial \mathbf{B}(\mathbf{r},\mathrm{t})}{\partial t} = -\nabla \times \mathbf{E}(\mathbf{r},\mathrm{t}) \tag{4.1}$$

$$\frac{\partial \mathbf{D}(\mathbf{r},\mathrm{t})}{\partial t} = -\nabla \times \mathbf{H}(\mathbf{r},\mathrm{t}) \tag{4.2}$$

$$\nabla \cdot \mathbf{D}(\mathbf{r},\mathrm{t}) = 0 \tag{4.3}$$

$$\nabla \cdot \mathbf{B}(\mathbf{r},\mathrm{t}) = 0 \tag{4.4}$$

For linear isotropic media, the fields E/B and D/H are related through the constitutive relations:

$$\mathbf{D} = \epsilon \mathbf{E} = \epsilon_0 \epsilon_r \mathbf{E} \tag{4.5}$$

$$\mathbf{B} = \mu \mathbf{H} = \mu_0 \mu_r \mathbf{H} \tag{4.6}$$

Equation (4.1) to Equation (4.4) are the first-order partial differential equations in space or/and in time. Mathematically, a first-order differential equation can be approximated with a *central-difference,* which is second-order accurate. The FDTD is based on the central-difference approximation applied in Maxwell's equations in both space and time.

The simulation domain is discrete in a regular spatial grid with the electric and magnetic fields calculated at every location of the grid. As time progresses, the values of electric fields on each grid are updated on the basis of the values of the magnetic field on the previous time-step and vice versa. The field at a given position is represented by a Yee Cell, named after Kane Yee who developed this technique [96]. Figure 4.1 shows a

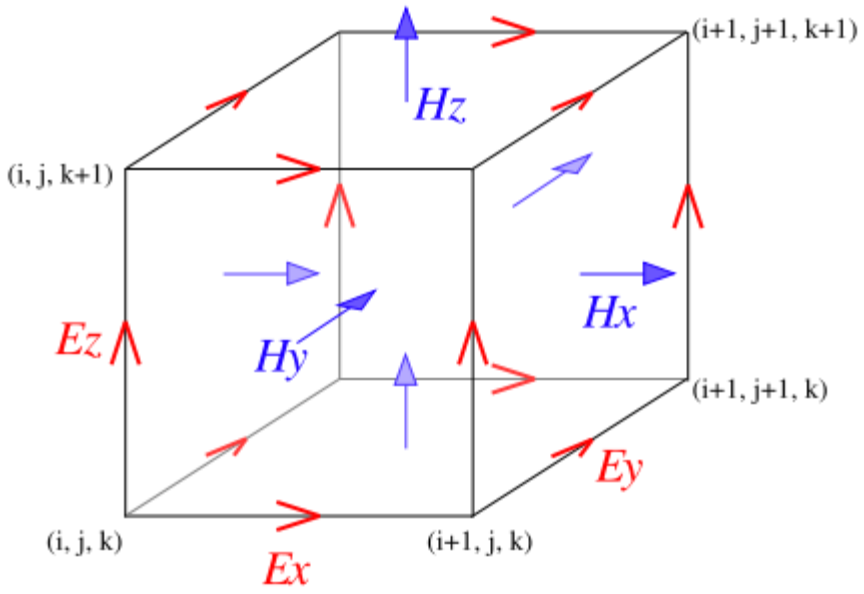

Figure 4.1 Position of various field components at Yee cell [96]. The electric fields are located in the middle of the cube edge with the magnetic fields shifted half steps from electric fields on the faces of the cube. The direction of magnetic fields is normal to the faces of the cube.

Yee unit cell in which electric and magnetic field components are distributed in different parts of a cube voxel. The electric field components form the edges of the cube, whereas the magnetic field components are normal to the face of the cube in half unit distant increments from the electric field components.

To correlate the Yee cell directly to Maxwell's equations, we will specify the spatial location of the Yee cell. Suppose the origin of Yee cell is at (0,0,0). E_x, E_y, and E_z components are located at (δx/2,0,0) , (0,δy/2,0) and (0,0,δz/2), respectively, where δa (a = x,y,z) is the grid size in each Cartesian direction. The magnetic fields are shifted by a half-integer-grid-size in each direction. That means magnetic field components H_x, H_y and H_z are on the face of the Yee cell at (0,δy/2,δz/2,), (δx/2,0,δz/2), and (δx/2, δy/2,0), respectively. The **E** and **H** field are arranged in Yee cells in such a way that if we want to

update H_y, according to Equation (4.1), we need the curl of E_z and E_x which lies on the same plane perpendicular to the *y* direction. This arrangement simplifies the numerical calculations and makes it faster to update.

Consider a simple one-dimensional plane wave propagating in a homogenous medium along the *z*-direction with the electric field plane polarized in the *x*-direction, i.e., $E_y = H_x = 0$. Equations (4.1) and (4.2) can then be written as:

$$\mu \frac{\partial H_y}{\partial t} = -\frac{\partial E_x}{\partial z} \tag{4.7}$$

$$\epsilon \frac{\partial E_x}{\partial t} = -\frac{\partial H_y}{\partial z} \tag{4.8}$$

Using the central–difference approximation on these two equations creates a discrete form:

$$\mu \left\{ \frac{H_y^{n+1/2}(k+1/2) - H_y^n(k+1/2)}{\delta t} \right\} = -\left\{ \frac{E_x^{n+1/2}(k+1) - E_x^{n+1/2}(k)}{\delta z} \right\} \tag{4.9}$$

$$\epsilon \left\{ \frac{E_x^{n+1/2}(k) - E_x^{n-1/2}(k)}{\delta t} \right\} = -\left\{ \frac{H_y^n(k+1/2) - H_y^n(k-1/2)}{\delta z} \right\} \tag{4.10}$$

where time and space is discretized as $t = n\delta t$ and $z = k\delta z$, respectively [97]. It is seen from Equation (4.9) that the central–difference approximation for the spatial differential of E_x is second-order accurate on the face center of the Yee cells. At this point the normal magnetic field H_y is situated. By staggering the electric and magnetic fields in time, the time-derivatives of fields are also second-order accurate. As a result, Equations

(4.9) and (4.10) are second-order accurate in both space and time.

It is assumed that the initial values of the discrete fields are known over all space, and as time progresses, the electric and magnetic fields keep updating by iteration. For example, if we know H_y^n and $E_x^{n+1/2}$ in Equation (4.9) in all spatial samples, we can update $H_y^{n+1/2}$ with the following relation:

$$\mu H_y^{n+1/2}(k+1/2) = \mu H_y^n(k+1/2) - \delta t \left\{ \frac{E_x^{n+1/2}(k+1) - E_x^{n+1/2}(k)}{\delta z} \right\} \quad (4.11)$$

Similarly,

$$\epsilon E_x^{n+1/2}(k) = \epsilon E_x^{n-1/2}(k) - \delta t \left\{ \frac{H_y^n(k+1/2) - H_y^n(k-1/2)}{\delta z} \right\} \quad (4.12)$$

Equations (4.11) and (4.12) are the recursive relations for a plane polarized wave propagating in the *z*-direction. Using a similar approach, one can generalize such a recursive relation for all components of the fields if they exist. Equations (4.11) and (4.12) are representative of Yee's algorithm, which is the foundation of FDTD technique.

4.3 Stability

As we discussed in the previous section, the FDTD algorithms are based on the evolution of time-steps. For the given simulation, the size of the time-step required to be a stable solution has some limit, known as Courant-Fredrichs-Lewy (CFL) stability limit [52]. The stability criterion on the basis of CFL limit is:

$$\delta t < \frac{1}{c} \frac{1}{\sqrt{\frac{1}{\delta x^2} + \frac{1}{\delta y^2} + \frac{1}{\delta z^2}}} \tag{4.13}$$

where c is the velocity of light. Equation (4.13) gives the restriction on the choice of time-steps for Yee algorithm in three-dimensional simulation domains. For a structure having more than one medium, the speed of light is not constant which modifies the stability criterion. Since the minimum time-step should be implemented, the general expression for stability limits is:

$$\delta t < \frac{1}{c_{max}} \frac{1}{\sqrt{\frac{1}{\delta x^2} + \frac{1}{\delta y^2} + \frac{1}{\delta z^2}}} \tag{4.14}$$

where c_{max} is the maximum speed of light in the given simulation domain.

In the stability equation (4.14) , we see only the upper bound in the time-steps. In the practical case, we have to choose the time-steps closest to the CFL limit. The stability equation can be expressed in terms of the stability factor:

$$\delta t = \frac{1}{c_{max}} \frac{stability\ factor}{\sqrt{\frac{1}{\delta x^2} + \frac{1}{\delta y^2} + \frac{1}{\delta z^2}}} \tag{4.15}$$

where the “stability factor” is chosen to be 0.99 in all of our simulation work.

4.4 Boundary Conditions

In general, the size of a computational problem is nearly infinite and it is impossible to implement such an unbound structure in the simulation domain. To overcome this inconvenience, the simulation domain should be truncated at a reasonable

size with appropriate artificial boundary conditions. The size of such simulation domains should be large enough to enclose the structure of interest. On the basis of the nature of the problem, there are many different boundary conditions such as perfectly electric conductor (PEC), perfectly metallic conductor (PMC), periodic boundary condition, Bloch's boundary conditions, etc. Among the typical boundary conditions employed in FDTD simulation is a perfectly matched layer (PML) absorption boundary condition. The PML was originally developed by Berenger [98] and it has been improved over the years. The idea of using a PLM boundary condition is to match the impedance (dielectric constant) between medium and in the PML layers so that the electromagnetic wave falling on PML layers will not encounter different mediums as it propagates.

The PML represents the open boundary condition in which the given material can be thought of as if extended to infinity. The simulation domain is surrounded by the PML with the layers of absorbing material so that the radiation will decay abruptly on each layer with minimal reflection. The number of layers on each side of simulation domain should be large enough so that the fields become sufficiently attenuated within the PML before reaching the exterior boundary. The consecutive parameters of the PML are chosen in such a way that it is perfectly matched to complex media such as lossy, dispersive, inhomogeneous, and even anisotropic media. Because of such flawless properties, the PML absorption boundary condition is an effective way of terminating the discrete FDTD lattice [99].

Figure 4.2 shows the schematic of the simulation domain. A plane wave source and a structure of interest are enclosed within the PML. Both the source and the arbitrary structure lie in a homogenous medium. The PML extends this homogenous medium to

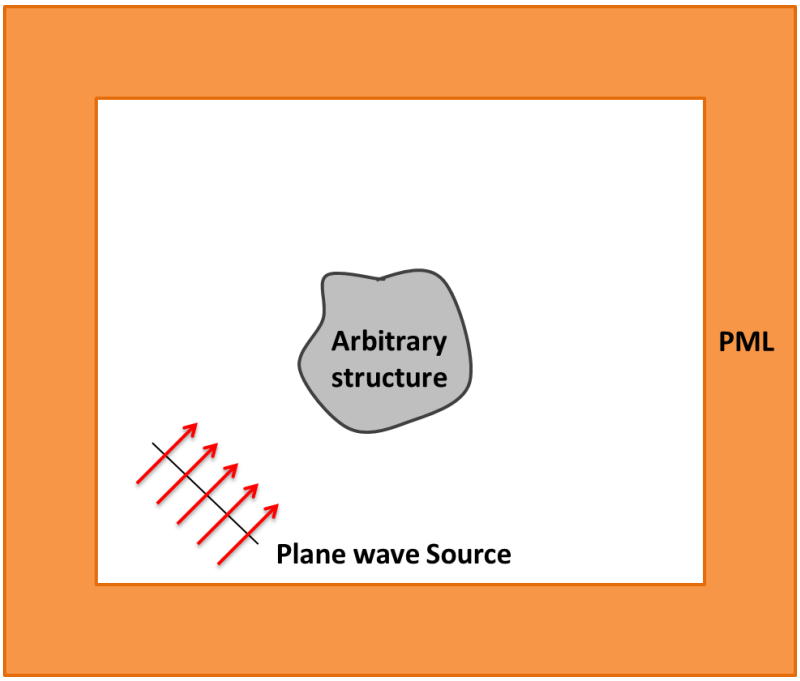

Figure 4.2 Schematic of a simulation domain. The PML surrounds the simulation region in which an arbitrary structure is within a homogenous medium. An electromagnetic plane wave is incident from a corner of the box.

infinity in all directions. In this schematic problem, we can study the interaction of plane wave with the structure, for example, the scattered field from an arbitrary particle.

4.5 Near-Field to Far-Field Projection

Even though the computational capability of the modern computer has been improved over many years, we still have limitations for solving real sized problems. As the computation time and required memory grows with the square of total number of grid points for a given simulation, the simulation needs to truncate to a finite size. Fortunately, the FDTD data solved near the structure of interest can be projected to the far-field ($d \gg \lambda$) easily and accurately.

The far-field transformation technique is based on the surface equivalence theorem. The original foundation of this equivalence theorem is from Huygens's principle

[52]. The surface equivalence theorem can be generalized as follows. All the sources including the objects of interest are enclosed by a closed surface. On that closed surface, a fictitious equivalent source is calculated which is an equivalent of real sources.

Figure 4.3 is a schematic diagram conceptually portraying the surface equivalence principle. The dotted red surface S contains the equivalent source and the black surface contains the observation points. Once the equivalent sources are found, the electric and magnetic vector potentials due to equivalent sources are calculated. Then, the electric and magnetic field at the observation point (far-field) is calculated from the vector potentials [52].

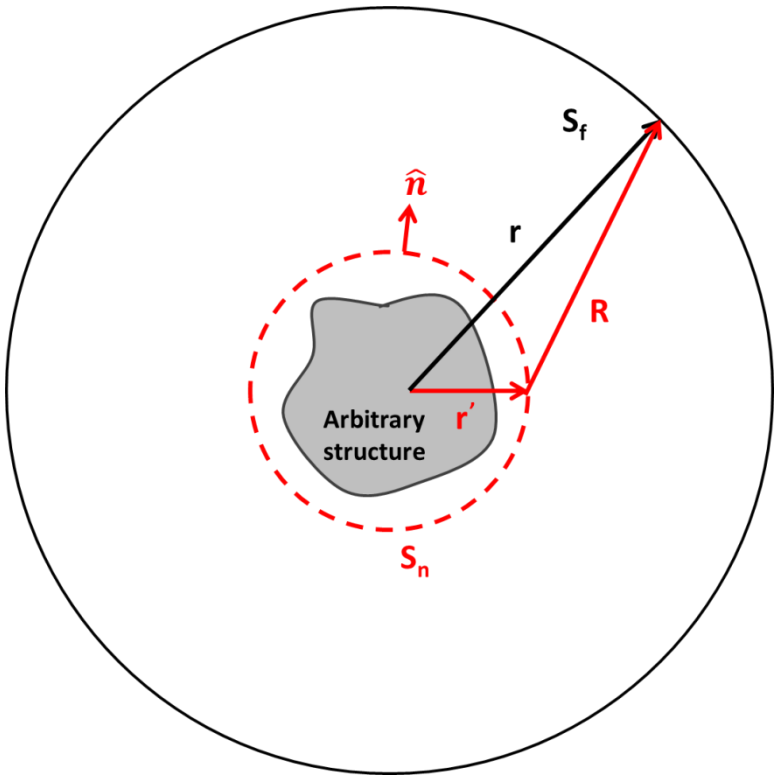

Figure 4.3 Schematic of equivalence theorem. All the sources including the structure of interest are enclosed by an equivalent surface (red-dotted circle). The fields are transferred to the outer surface (black circle) from the inner surface.

The surface equivalence theorem can be applied in three-dimensional problems in the same way. Besides that, if we know the electric and magnetic field on a 2-D plane (provided that the fields decay on the edges of plane), we can project an electric and magnetic field at any point beyond the plane, as depicted in Figure 4.4 [52].

4.6 Lumerical Solutions

There are many commercial or freely available FDTD solvers for electrodynamics problems. I used Lumerical Solutions [100], a commercial FDTD solver, to study the emission pattern due to a sharp metallic tip scanning near a single emitter. In the previous section, I discussed some of the basic foundations of FDTD technique, stability condition, boundary conditions, and a special case for near-field to far-field transformation. In practice, a simulation involves designing the experimental conditions as accurately as

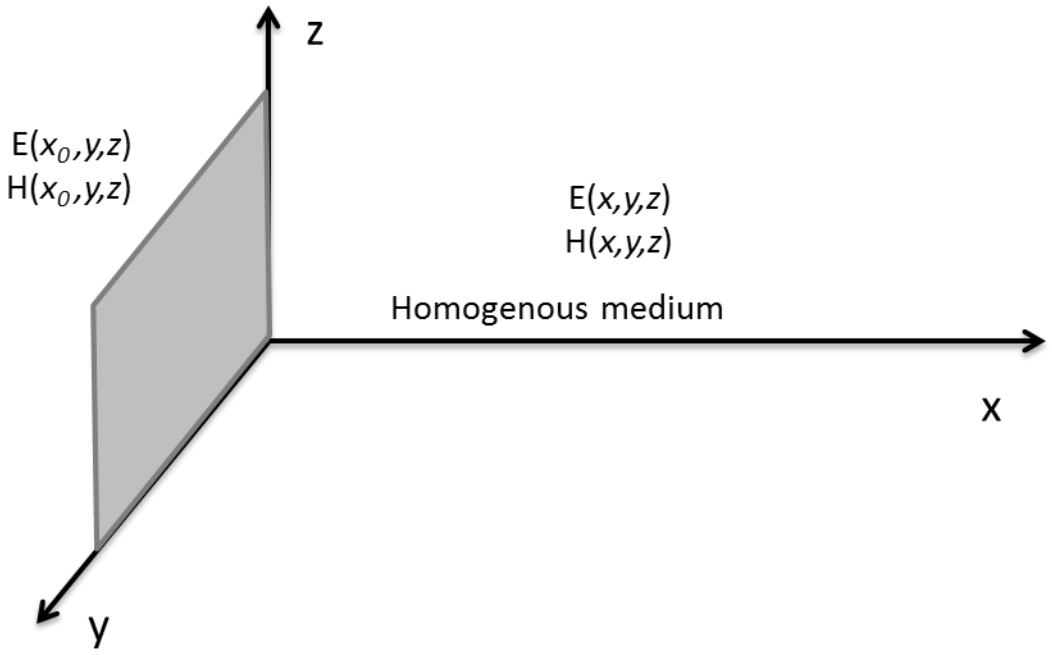

Figure 4.4 Far-field projection from a plane. If we know electric and magnetic field on a plane, we can calculate electric and magnetic field at any point beyond the plane. The size of the plane should be big enough such that the fields are zero everywhere beyond the edge of the plane.

possible, defining the material properties for all structures, introducing the source to excite the system, defining the boundary conditions, and placing monitors (objects on which fields are calculated in the simulation domain) on the region of interest. An example simulation I used for a gold tip near a tilted dipole just above the air/glass interface is shown in Figure 4.5.

4.7 Conclusion

The FDTD method is widely used to solve electromagnetic systems because it is simple to implement numerically. It provides flexible means for directly solving

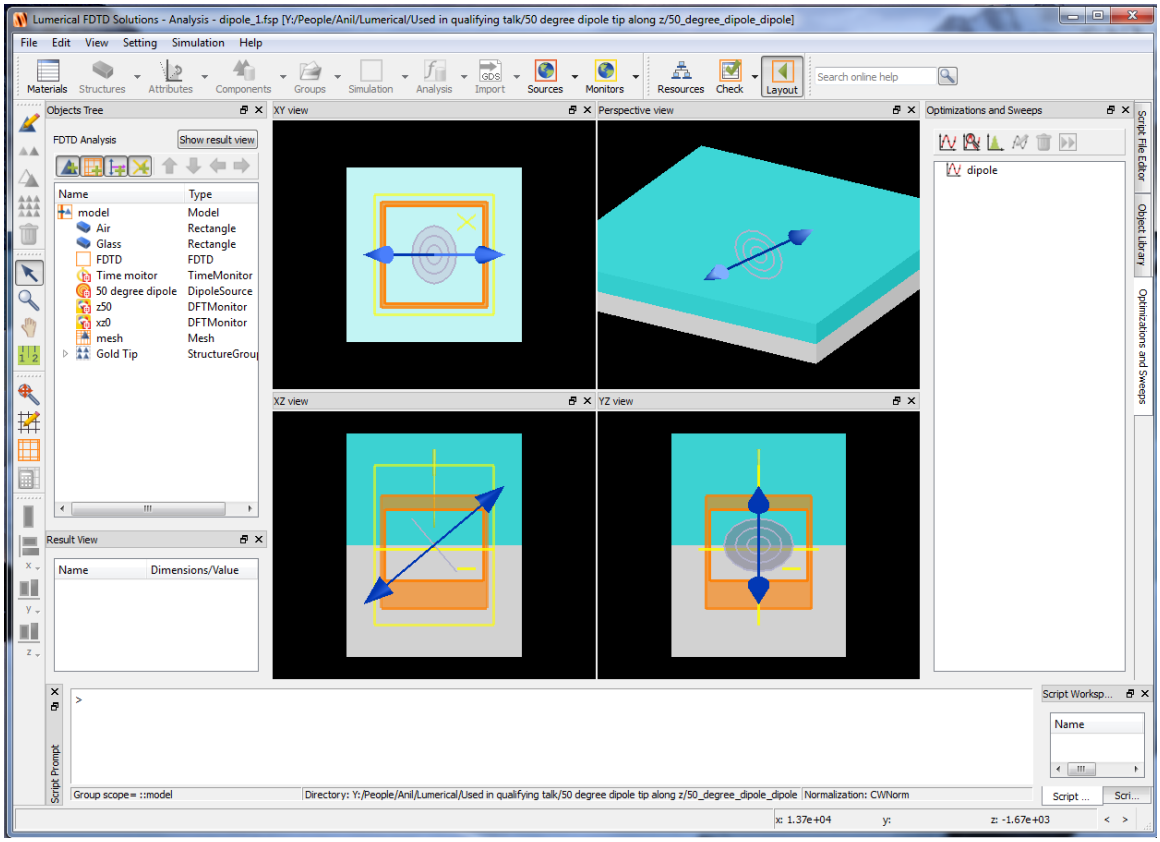

Figure 4.5 Screen-shot for an example simulation for a gold tip near a tilted dipole sitting just above the air/glass interface.

Maxwell's time-dependent equations by using central-differences on a discrete lattice. It can be used to solve various types of electromagnetic problems, including microscopy, photonics crystals, nonlinear optics, antenna, etc. In this chapter, I reviewed the fundamentals of the FDTD method, Yee's algorithms for a simple problem on a spatial and temporal grid, important boundary conditions, and the PML. I briefly discussed how near-field can be transferred to far-field, which is a useful tool to study the radiation pattern far from an antenna. I also introduced Lumerical Solution, a FDTD solver which I used throughout this work.

CHAPTER 5

USING A SHARP METAL TIP TO CONTROL THE POLARIZATION AND DIRECTION OF EMISSION FROM A QUANTUM DOT

A sharp metallic Atomic Force Microscope (AFM) tip can act as an optical antenna as the diameter of the apex (d ~ 50 nm) is comparable to the size of an optical antenna. Our unique data acquisition technique is used to explore the optical interaction between a tip-antenna with an emitter and its usefulness to control the emission properties like polarization and direction of emitted photons in the single photon limit. To the best of my knowledge, these studies are the first such dynamic measurement of polarization and directional control of emission using AFM tip.

This work is published in the Scientific Reports at Nature Publishing Group (Sci. Rep. 4, 6456, 2014). This chapter is fully adapted from this paper. Section headings are inserted and adjusted to make a flow of the chapter. Supplementary information from the paper is added as an additional section.

5.1 Abstract

Optical antennas can be used to manipulate the direction and polarization of radiation from an emitter. Usually, these metallic nanostructures utilize localized plasmon resonances to generate highly directional and strongly polarized emission, which is determined predominantly by the antenna geometry alone, and is thus not easily tuned. Here we show experimentally that the emission polarization can be manipulated using a

simple, nonresonant scanning probe consisting of the sharp metallic tip of an atomic force microscope; finite element simulations reveal that the emission simultaneously becomes highly directional. Together, the measurements and simulations demonstrate that interference between light emitted directly into the far-field with that elastically scattered from the tip apex in the near-field is responsible for this control over polarization and directionality. Due to the relatively weak emitter-tip coupling, the tip must be positioned very precisely near the emitter, but this weak coupling also leads to highly tunable emission properties with a similar degree of polarization and directionality compared to resonant antennas.

5.2 Introduction

The function of an optical antenna is to reduce the impedance mismatch between propagating (far-field) radiation modes and nonpropagating (near-field) evanescent modes, which allows an emitter to absorb and/or emit light more efficiently [9, 62]. A consequence of the coupling between an antenna and an emitter is that the radiation pattern and/or polarization can be strongly modified [11, 12, 16-21, 79, 101, 102]. This phenomenon is fundamentally interesting, and forms a basis for developing single photon sources for quantum information applications [22-24]. Optimally, antennas would provide simultaneous control over the direction, phase, and polarization of individual photons emitted from a source, requiring a comprehensive understanding of the emitter-antenna coupling. Here, we demonstrate that the sharp, nonresonant tip of an atomic force microscope (AFM) can be used to simultaneously control the polarization and direction of emission from individual quantum emitters. In contrast to resonant antennas where the large local density of optical states (LDOS) leads to emission properties dominated by the

antenna modes, the much smaller LDOS values for nonresonant tips leads to an emission pattern and polarization that depend very sensitively on the position of the tip and the orientation of the emitter. When separated by an intermediate distance, the emitter and tip contribute roughly equally to the emission properties, and we show that maximum control over the emission direction and polarization is achieved in this intermediate zone, with performance similar to resonant antennas but with much better tunability.

In one of the earliest demonstrations, Gersen *et al.* used the annular disk of an aperture-type near-field probe to control the emission pattern from single molecules [16] and later, this group used a similar setup with polarization analysis to demonstrate reversible polarization control [17]. Other work falls mostly into two general categories: nonscannable but highly directional antennas [11] and scannable resonant antennas, which include both linear [12, 103] and spherical [13, 14, 101] geometries. In the first category, Curto *et al.* used a multielement Yagi-Uda antenna to generate highly directional, strongly polarized emission from a single QD, but because that QD was painstakingly positioned lithographically, it was difficult to study the emission properties as a function of the QD position. In the second category, Taminiau *et al.* and Neumann *et al.* used scanning single-element dipole antennas to strongly modify the emission pattern, which was dominated by the resonant dipolar modes of the antenna, and was thus neither highly directional nor very tunable [12, 103]. Kuhn *et al.* used a resonant gold nanosphere (50 nm diameter) attached to the end of a glass fiber to control the emission polarization and directionality as the sphere was scanned in the vicinity of isolated emitters [13, 14, 101]. Kuhn *et al.* also attempted to use nonresonant sharp tips, but no change in the emission pattern was detected [14], most likely because without a resonance, these tips

must be brought much closer to the emitter to control emission properties, which leads to strong quenching of the fluorescence (nonradiative energy transfer). This problem is exacerbated when the emission is imaged directly (as was done by Kuhn *et al.*), since the scarce photon signal is then spread over the face of the camera, resulting in very low signal-to-noise ratios. Here, we employ a novel single-photon counting technique [104] coupled with polarization anisotropy measurements and finite-difference time domain (FDTD) simulations to show that despite strong quenching, sharp nonresonant tips can be used to generate highly directional and strongly polarized emission from isolated QDs.

5.3 Experimental Section

A schematic of the experimental setup is shown in Figure 5.1. The overall design has a commercial AFM (Asylum Research MFP3D) sitting atop a homebuilt inverted confocal optical microscope. A laser beam is incident on a beam stop (BS) that passes only supercritical rays through a high numerical aperture (NA = 1.4) objective lens creating a focused, vertically polarized evanescent field at the sample plane. The AFM tip is aligned into the center of the focal spot and a single CdSe/ZnS QD ($\lambda \sim 605\ nm$ from Invitrogen) is then positioned near the tip. The emitted fluorescence is collected by the same objective lens, and a polarization beam splitter (PBS) separates the emission into two orthogonal channels, each of which is monitored by an avalanche photodiode (APD). The detected photons are timestamped, and the arrival times are subsequently correlated with the lateral position of the tip and its height above the sample surface. Since the AFM tip oscillates vertically and the sample is scanned laterally, the photon count rate for each channel is measured as a function of the tip position in the three-dimensional half-space above the sample plane [104]. Separating the collected fluorescence into two orthogonal

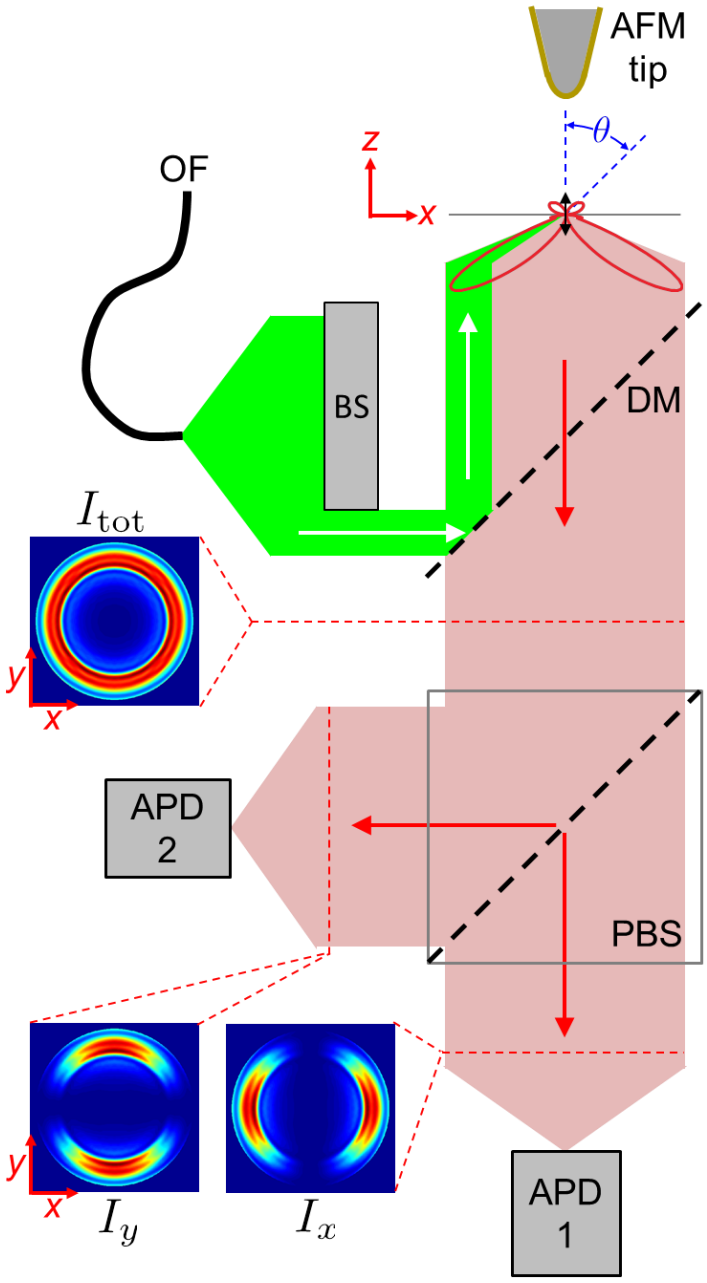

Figure 5.1 Schematic of experimental setup. Laser light from an optical fiber (OF) is collimated, directed through a beam stop (BS), and then reflected from a dichroic mirror (DM). An oil-immersion microscope objective (NA =1.4) focuses the laser beam and collects emitted fluorescence. An AFM tip is positioned near an illuminated QD; the fluorescence emission passes through the DM and is incident on a polarization beam splitter (PBS). The *x*- and *y*- polarization components are measured separately using two avalanche photodiodes (APD). A simulated polar plot of emission intensity for a *z*-oriented dipole at the air/glass interface is shown at the sample plane to help illustrate the geometry. Simulated back-focal images for the same *z*-dipole are shown just after the objective (I_{tot}) and in the two legs of the polarization analyzer (I_x and I_y).

polarization channels allows the emission polarization to be monitored continuously, photon by photon, as the relative position between the tip and QD is controlled with ~ 1 nm precision. To quantify the anisotropy between the two channels, we define the degree of polarization (DOP):

$$\mathrm{DOP} = \frac{I_x - I_y}{I_x + I_y} \tag{5.1}$$

where I_x and I_y are the signal intensities (in counts/s) in the *x* and *y* channels, respectively. The value of the DOP lies between -1 and +1, with the extremes signifying linearly-polarized emission perfectly aligned with one channel or the other.

5.4 Results

5.4.1 Polarization Control

Figure 5.2 shows experimental measurements of the total fluorescence signal (panel A: sum of *x* and *y* channels) and DOP (panel B: as per Equation 5.1) from a QD as a function of the position of a gold-coated tip within an *xz*-plane that cuts through the center of the QD. The pixel values in panel A are normalized column-by-column to the average photon count rate for $z > 50$ nm, after the background count rate has been carefully subtracted from each polarization channel. The emission from the QD is strongly quenched in the near-field of the tip mainly due to nonradiative energy transfer [71]. The DOP image shown in panel B is calculated using background-subtracted count rates from the corresponding pixels on each channel. Clearly, the DOP decreases for small tip distances directly above the QD, indicating the emission polarization has equal *x* and *y* components. In contrast, when the tip is on either side of the QD, the DOP value

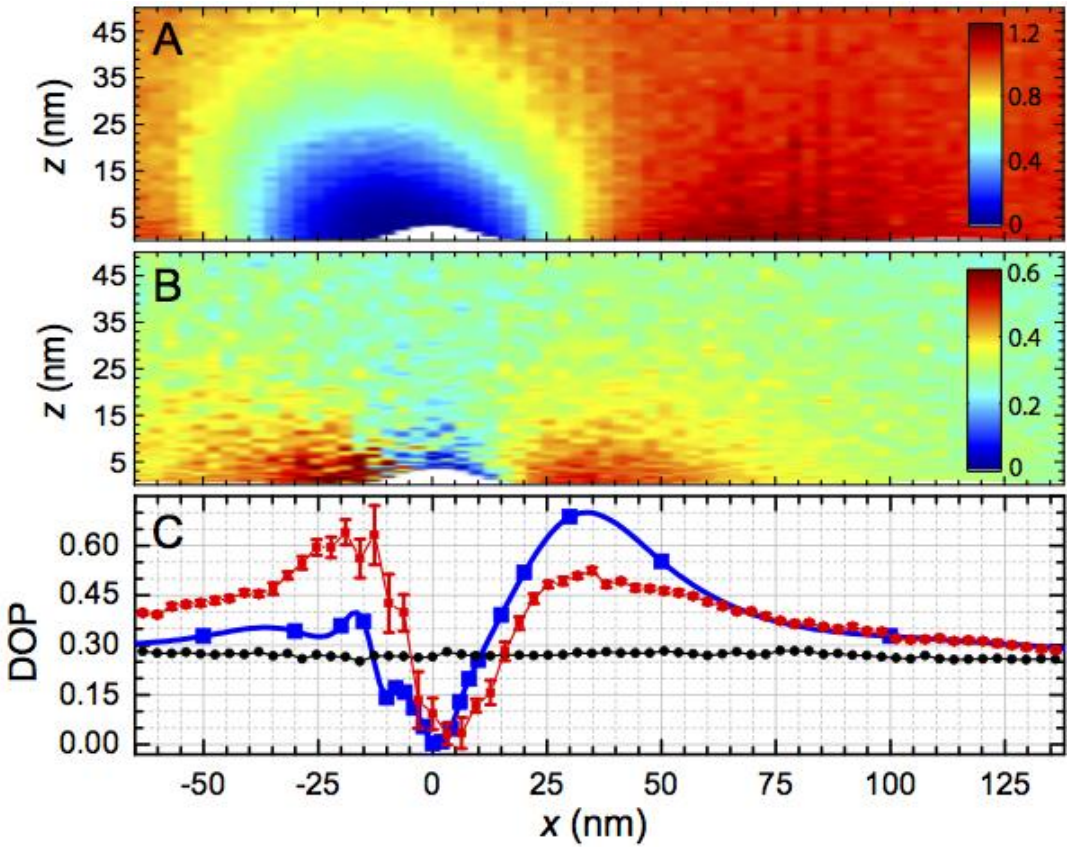

Figure 5.2 High-resolution measurements of tip-induced polarization changes. A) Fluorescence intensity from a QD (Ix + Iy) as a function of tip position in an xz-plane through the center of the QD. The color bar gives the intensity normalized to the far-field intensity (z > 50 nm) at each lateral (x) position of the tip. B) Corresponding DOP image calculated using Equation 5.1. C) Section plots from panel B for z > 50 nm (black symbols) and z < 2 nm (red symbols). Blue squares depict the simulated DOP for a gold tip (with 15 nm radius of curvature) 2 nm above the air/glass interface and a dipole emitter tilted by $\theta = 45^{o}$ relative to the vertical in the *xz*-plane. The white space in panels A and B represent the AFM height trace and the blue line in panel C is a guide to the eye.

increases, indicating that the emission becomes strongly polarized along the *x* direction. We have performed ~40 DOP measurements on >25 QDs and the data shown here are very representative of the observed trends even though each QD measured exhibits a different DOP value in absence of the tip due to orientational variations. For example, all QDs measured exhibit an increase in the DOP magnitude when the tip is on either side of the QD, and a decrease in magnitude when the tip is just above the QD, as illustrated in

Figure 5.3 and Figure 5.4. These observations are consistent with previous work using different tip/antenna geometries [17, 18].

Comparing Figure 5.2A and 5.2B reveals a clear difference in the length scales associated with changes in the total fluorescence signal and DOP as well as a difference in how they depend on the location of the tip apex. When the tip approaches the QD from directly above, fluorescence quenching initiates when the tip is ~ 60 nm above the QD whereas the emission polarization is not affected until the tip approaches to within ~ 10 nm, as demonstrated by the red curves in Figure 5.3. Furthermore, when the tip approaches the QD from the side, the DOP initially increases reaching a peak value when the tip is 20-35 nm on either side of the QD, whereas the total fluorescence signal decreases fairly monotonically as the tip approaches. Interestingly, when a single carbon nanotube (CNT) is used as an AFM probe [85, 105, 106], it does not affect the polarization at all even though the CNT strongly quenches the QD emission (black curves in Figure 5.3).

When the tip is laterally displaced from the QD (along *x* in Figure 5.2C), we observe a substantial increase in the DOP indicating predominantly *x*-polarized signal photons. We have also acquired DOP data when the tip is scanned in a *yz*-plane, and the resulting images exhibit similar features to those shown in Figure 5.2B and C, but the DOP values are negative, indicating the signal photons are predominantly *y*-polarized, which is discussed in Section5.6.5. Thus, as the tip is scanned laterally in the vicinity of the QD, the emission polarization can be controlled such that it follows the direction separating the QD and tip apex.

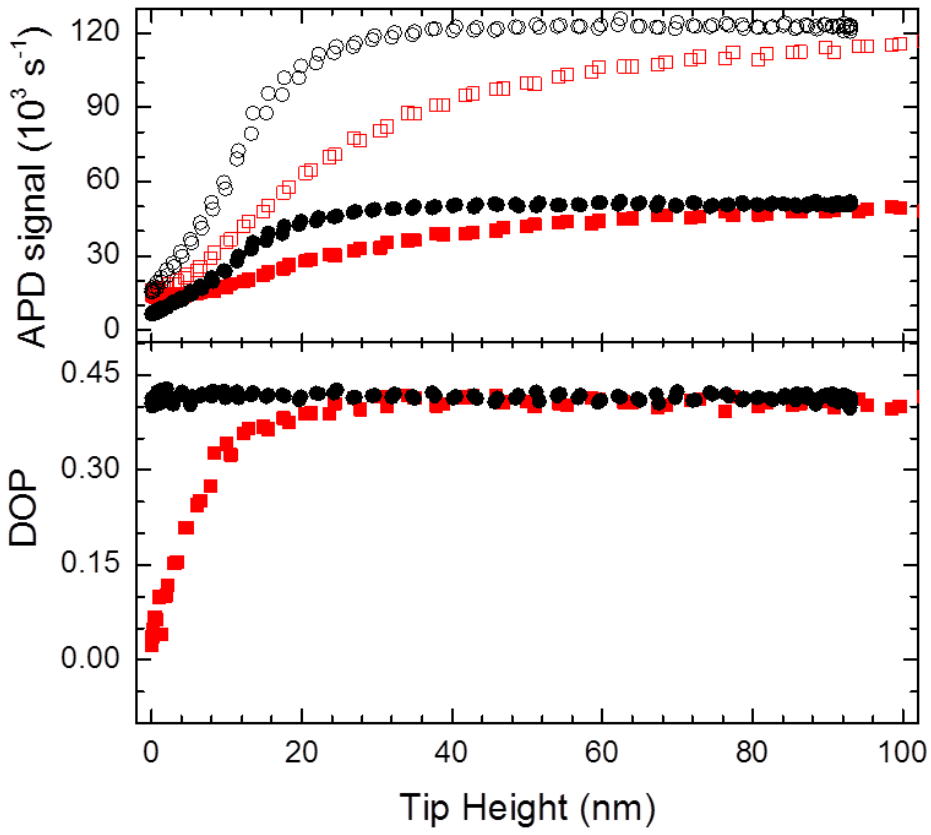

Figure 5.3 Vertical DOP approach-curve measurements for a carbon nanotube tip (black circles) and a gold tip (red squares). These measurements were performed on two different QDs that have the same asymptotic DOP value. Upper: The open (closed) symbols correspond to photon count rates on the *x* (*y*) APD channel as the tip is lowered onto a QD from above. Lower: DOP values computed from the data in upper panel.

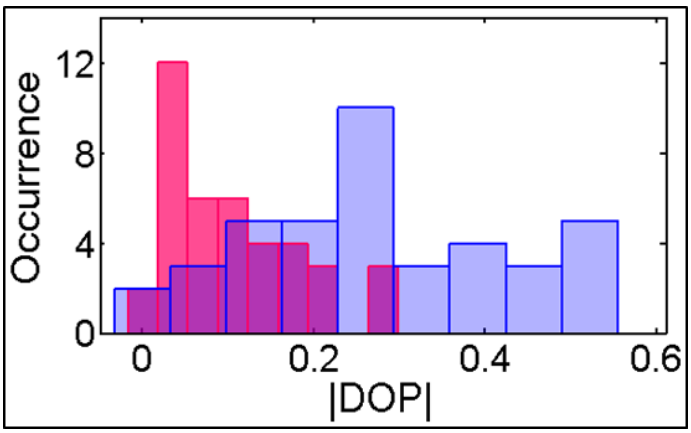

Figure 5.4 Histogram of ~ 40 DOP measurements when a gold tip is far above the QD (blue bars) and within 2 nm of the QD (red bars).

5.4.2 Directional Control

To investigate directional control of the emission pattern, we used rigorous finite-difference time domain (FDTD) simulations (Lumerical, Inc.) to generate polarization and directional maps of the collected far-field emission. Although it would be ideal to measure the emission pattern directly using, e.g., back-focal imaging as the tip is scanned over an isolated QD, such a direct measurement is difficult to achieve in combination with the high-precision photon counting technique employed here. The simulation is used to generate the emission pattern (back-focal images) and the emission directionality (D_x) is quantized as the ratio of emission intensity at two diametrically opposite points in the back-focal images, either along the *x*-axis (D_x) or the along the *y*-axis (D_y):

$$D_x = 10\log\left[\frac{I_{+x}}{I_{-x}}\right] \tag{5.2}$$

$$D_y = 10\log\left[\frac{I_{+y}}{I_{-y}}\right] \tag{5.3}$$

D_x and D_y are measured in decibels and also referred to as front-to-back ratios. To compute I_{+x} (or I_{-x}), we summed the simulated back-focal intensities within an angular window defined by an azimuthal range $-2^o < \phi_{+x} < 2^o$, ($178^o < \phi_{-x} < 182^o$) and a polar range $38^o < \theta < 68^o$; more than 80% of the total emission falls within this range of polar angles. I_{+y} and I_{-y} are computed in a similar fashion with the azimuthal ranges rotated by 90^o. This procedure for extracting emission patterns from polarization anisotropy measurements using FDTD simulations is similar to that employed by Taminiau *et al.* [12].

The simulated and experimental measured DOP curves in Figure 5.2C qualitatively agree with each other, which validates the simulations of emission patterns and directionality. The quantitative difference in magnitude and asymmetry between the simulated and measured DOP values are due to the simplified model for the QD (linear instead of 2D degenerate dipole [87, 89]) and also our simplified model for the tip as a vertically-oriented cone instead of a tilted and asymmetric pyramid; nonetheless, the strong qualitative agreement yields critical insights into the pertinent physics. Details of the simulations and postprocessing are described below in the Simulation details.

Figure 5.5 shows a sample of simulated back-focal images for different lateral positions of the gold tip for the conditions described above. The vertical tilt angle, θ, of the dipole is adjusted to 45^{o} to give an asymptotic DOP value matching the particular QD under study (Figure 5.2C). The lower panel in Figure 5.5 quantifies the directionality of the emission for tip positions at the specified points along the *x*- (blue squares) and *y*- (green squares) axes, and the labeled points A-E correspond to five of the back-focal image panels; the sixth panel labeled ∞ shows the results of a simulation with no tip. The simulations reveal that the emission pattern can be strongly altered by the presence of the tip: photons are usually “steered" toward the tip [13, 15] with some limited regions (e.g., point A) where the photons are steered away from the tip. For the specific emitter orientation considered here ($\theta = 45^{o}$), there is an optimal tip-emitter lateral separation that produces highly directional and strongly polarized emission, as shown in Figure 5.2 and 5.5. Due to the asymmetry in the axial (*z*) component of the field near a tilted dipole (see Section 5.7.2), the tip must get closer to the emitter on one side (x = 10 nm) compared to the other (x = +20 nm) to achieve the conditions for optimal control over the emission

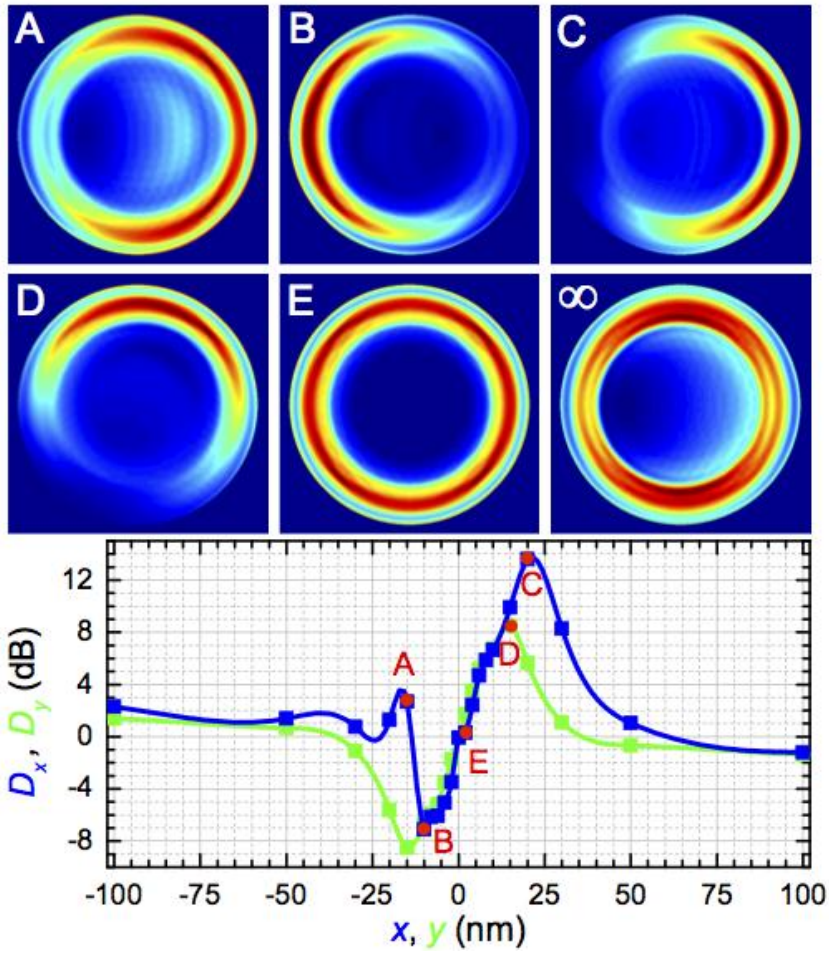

Figure 5.5 Directional control of emission from a dipole using a gold tip. In these simulations, the dipole has a tilt angle $\theta = 45^o$ and is located at (x,y,z) = (0,0,2) nm. The coordinates of the tip apex in nm are (x,y,z) = (-15,0,2), (-10,0,2), (20,0,2), (0,15,2), and (0,0,4) for points A-E, respectively. The lower panel shows the directionality as the tip is positioned along the x and y axes at the specified points. In absence of the tip (panel marked ∞), the unperturbed directionalities are D_x = 0.4 and D_y = 0. The green and blue curves in the lower panel are guides to the eye.

direction and polarization.

5.4.3 Comparing Sharp Tip with Sphere

Figure 5.6 shows the DOP (black) and directionality (red) for gold spheres with radii of 15 nm (dotted lines) and 50 nm (dashed lines), along with curves for a sharp tip with 15 nm radius of curvature (solid lines). Compared with a sphere of the same radius of curvature (15 nm), the AFM tip yields much better control over both polarization and direction. Compared with a much larger sphere (50 nm), the AFM tip yields somewhat better polarization control and much better directional control, but at the cost of requiring much better positional accuracy as the tip must be brought much closer to the emitter.

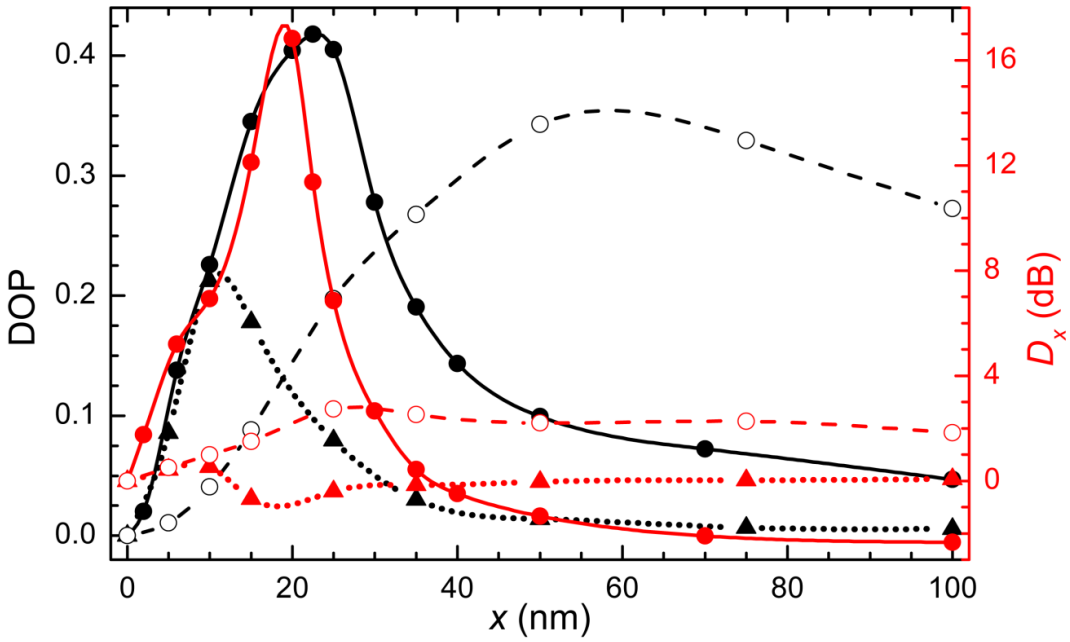

Figure 5.6 DOP (black) and directionality (red) for a vertical dipole and various nanostructure geometries: gold tip with 15-nm radius of curvature (solid lines), sphere of radius 15 nm (dotted lines), and sphere of radius 50 nm (dashed lines). The symbols represent the simulated conditions and the curves are guides for the eye.

5.4.4 Spectral Response of a Sharp Tip Compared to a Nanosphere

Figure 5.7 shows the DOP (A and B) and directionality (C and D) for a sharp gold tip with 15 nm radius of curvature and a gold nanosphere with 50 nm radius for different lateral positions of the tip/sphere relative to a vertically oriented dipole emitter. The black, red, blue, magenta, green, and navy curves represent emission wavelengths of 480, 540, 580, 605, 650, and 700 nm wavelengths, respectively. Compared with the nanosphere, the AFM tip yields much better directional control and similar polarization control over a broad wavelength range. The AFM tip also yields much better control over both polarization and direction compared with a smaller nanosphere (15 nm radius), as shown in Figure 5.6. The superior spectral response of the semi-infinite tip geometry is due, in part, to a lack of localized surface plasmon resonances, and in part to the strong vertical polarizability of the tip.

In contrast, the nanosphere has an isotropic polarizability, which prevents the formation of a strong linear dipole moment in the sphere, particularly since the near-field of the emitter decays very rapidly in space, $\propto 1/r^3$, leading to large field inhomogeneity within the sphere [1]. Furthermore, the coupling between an emitter and nanosphere is strongly modulated by plasmon resonances in the sphere (see Appendix F: plasmons resonance for a 50 nm radius gold sphere occurs at ~540 nm wavelength in free space), which have well-defined oscillation modes that generally do not lead to highly directional emission. The improved performance of the tip compared to the nanosphere requires better positional accuracy since the spatial dependence (Figure 5.7) shows sharper peaks that occur at smaller tip-displacement values, *x*.

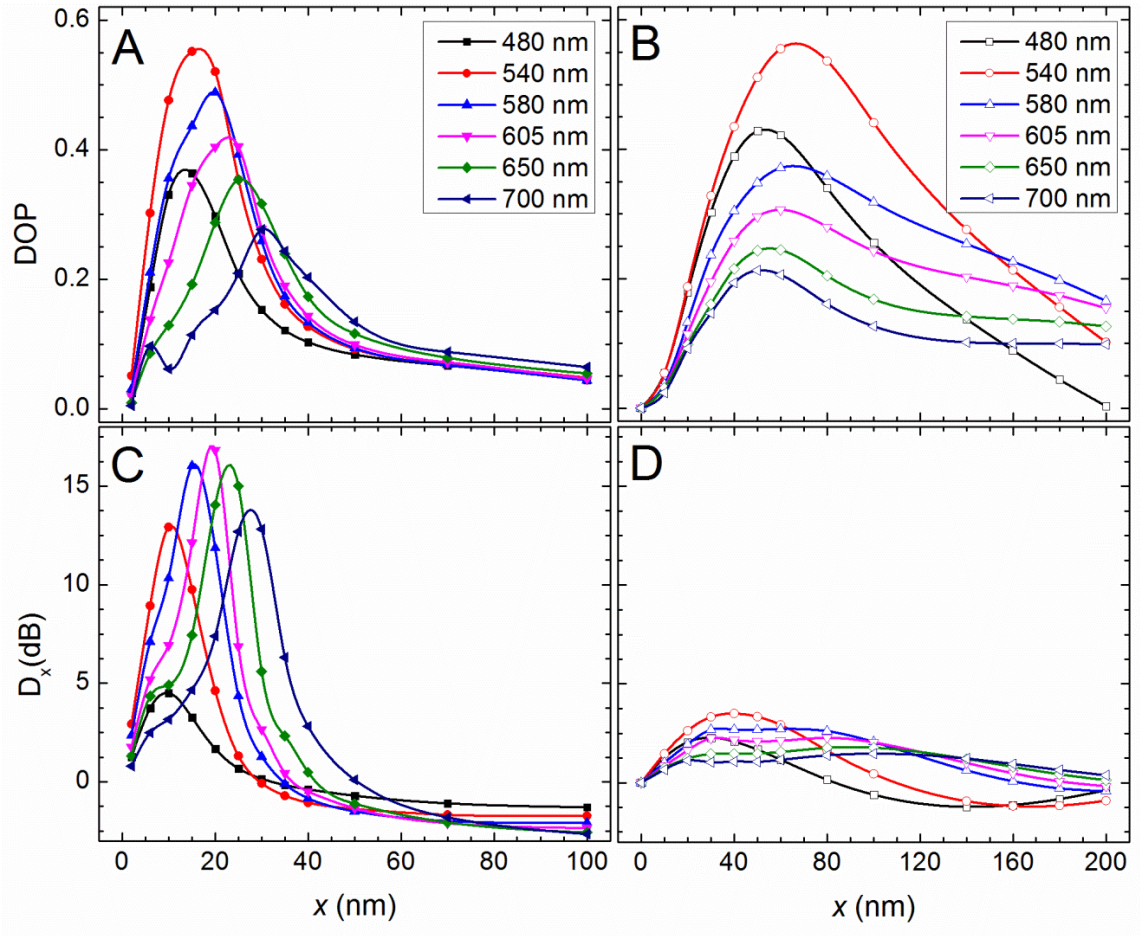

Figure 5.7 DOP and directionality (D_x) curves for a vertical dipole emitter with six different vacuum emission wavelengths. For all graphs, the black, red, blue, magenta, green, and navy curves represent emission wavelengths of 480, 540, 580, 605, 650 and 700 nm, respectively. Panels (A) and (C) correspond to a sharp gold tip with 15 nm radius of curvature and panels (B) and (D) correspond to a gold nanosphere with radius 50 nm. The horizontal axis corresponds to the lateral displacement of the tip/sphere apex relative to the dipole position (note the different scales between the right and left panels). The curves are guides for the eye.

5.5 Discussion

As the tip approaches the QD in Figures 5.2 and 5.3, the difference in characteristic length scale associated with the total fluorescence signal ($I_x + I_y$) and DOP implies that there are two different physical mechanisms responsible for quenching and polarization/directional control. Indeed, previous work has described two distinct emitter-tip coupling mechanisms: a short-range FRET-like dipole-dipole coupling and a longer-range effect associated with the generation of surface plasmon polaritons (SPPs) that propagate up the tip sidewalls [71] . We attribute the longer-range quenching in our measurements (Figures 5.2 and 5.3) mainly to the generation of propagating SPPs on the tip, while the short-range polarization/directional control is attributed to the dipole-dipole coupling mechanism. The “tip" dipole in this dipole-dipole mechanism can be considered as an image of the source (emitter) dipole at the tip apex constrained by the dominant vertical polarizability of the tip. The magnitude of the tip dipole depends on the local strength and direction of the emitter's near-field, both of which fluctuate sharply near the emitter (see Phase and Magnitude Section).

We find that control over emission polarization and directionality is optimized when the source (emitter) and image (tip) dipoles have equal magnitude, are parallel to each other (as with the Yagi-Uda antenna), and are nearly 180^0 out of phase with each other (Figure 5.8). Nanospheres used as antennas lack a well-defined linear dipole moment, particularly when driven by the local source field of a nearby emitter, so control over directionality and polarization is suboptimal (Figure 5.7). On the other hand, a vertically-oriented resonant dipole antenna has the requisite linear dipole moment, but due to strong plasmon resonances, it must be kept further from the emitter to achieve a

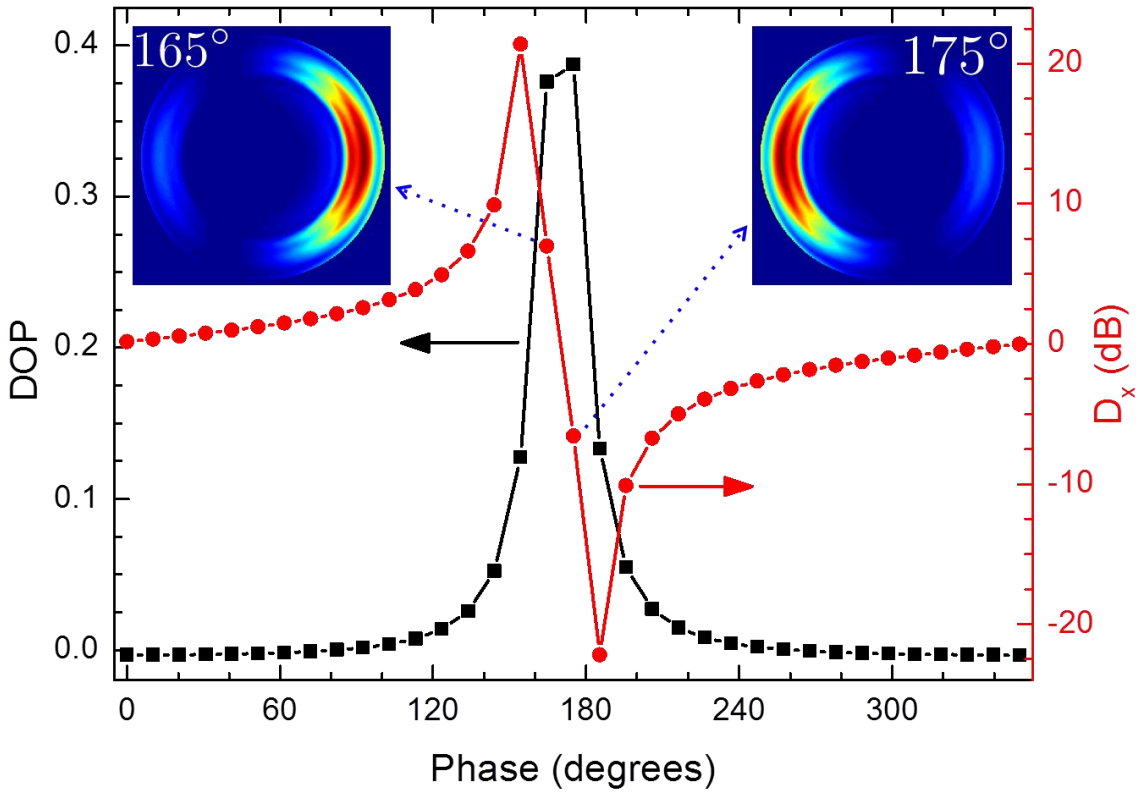

Figure 5.8 Simulated DOP and directionality for two identical vertical dipoles at x = 0 and x = 20 nm. Both dipoles are 2 nm above the air/glass interface. The phase of the dipole at x = 20 nm is varied with respect to the other. The insets show simulated back-focal images for phase angles of 165^{o} and 175^{o}.

similar dipole magnitude; this leads to a suboptimal phase relationship between the source and tip dipoles, resulting in less directional emission [12, 18]. The sharp metallic tips used here possess a strong vertical dipole moment, and since they are nonresonant, they must be brought closer to an emitter to achieve a similar dipole magnitude; this leads to near optimal phase and magnitude relationships between the source and tip dipoles and strong control over emission polarization and directionality.

This dipole-dipole model suggests that the far-field radiation can be understood as the superposition of two source fields, one from the emitter and one scattered from the tip [1, 13, 46]. This idea is verified using a single-wall carbon nanotube (CNT) attached to an

AFM probe since CNTs are strong fluorescence quenchers [106], but not strong light scatterers. As Figure 5.3 demonstrates, the CNT does not alter the emission polarization, nor presumably the directionality, when it approaches a QD. In contrast, the gold-coated tips used here are strong scatterers and although they strongly quench fluorescence, they also can be used to efficiently control the polarization and directionality of emission. As discussed above, the polarizability of an elongated tip is predominantly along its vertical axis [1, 107], leading to a dipole moment that by itself would produce radially polarized emission at the back-focal plane (Figure 3.1) and a DOP value near zero. Given this, it is evident from Figure 5.2 and 5.3 that when a gold tip is lowered onto the QD from directly above, the collected signal is predominantly composed of photons scattered from the tip, while when the tip is displaced laterally by more than ~5 nm, the collected signal is the superposition of photons scattered from the tip and those emitted directly by the source.

5.6 Summary

In conclusion, we have demonstrated that the emission polarization and direction can be manipulated dynamically using a simple, nonresonant AFM probe. The mechanism responsible for this control is the interference between light emitted directly into the far-field with that elastically scattered from the tip apex. Furthermore, due to the relatively weak emitter-tip coupling, the tip must be precisely positioned very close to the emitter, but this weak coupling also leads to highly tunable emission properties. Overall, the semi-infinite geometry of the tip yields superior polarization and directional control compared to either a metallic sphere or a resonant dipole antenna, and performs similarly to lithographically fabricated, highly-directional antennas. The ability to control the polarization together with the direction of emission could have important implications for

the development of integrated nanophotonic devices and single photon sources.

5.7 Additional Information

5.7.1 Tip-Induced Rotation of Emission Polarization

Figure 5.9 shows an experimental DOP measurement, similar to Figure 5.2, but the tip scanning axis is rotated by 90^{o}: the tip is scanned in the *yz*-plane rather than the *xz*-plane. Figure 5.9A shows the total fluorescence signal summed in both polarization channels when the tip was scanned over a QD: the background signal in each polarization channel was subtracted separately. The data column corresponding to each lateral position of the tip was normalized to the average signal for large tip-heights ($z > 50$ nm) at that lateral position. The calculated DOP is shown in Figure 5.9B. In both Figure 5.9A and 5.9B, the delineated white region is the overlaid topography of the QD obtained from the AFM data. The blue line in Figure 5.9C shows the DOP as a function of lateral tip position when the tip is very close to the sample surface ($z < 2$ nm), while the green line is the DOP when the tip is far above the sample plane ($z > 50$ nm).

The fluorescence signal is reduced when the tip is near the QD, as demonstrated by the colorscale in Figure 5.9A. The quenching of fluorescence is mainly due to energy transfer from the QD to the gold tip [108]. When the tip is far above the QD, the DOP has a constant value of ~ 0.1, as indicated by the green line in Figure 5.9C: this positive DOP value indicates that the QD emission is more strongly polarized along the *x*-axis than the *y*-axis. When the tip approaches the QD on either side, the DOP value becomes negative, indicating that the polarization has been rotated toward the *y*-axis: this is clearly demonstrated by the blue line in Figure 5.9C. FDTD simulations demonstrate that this polarization rotation is caused by redirection of the QD emission toward the tip.

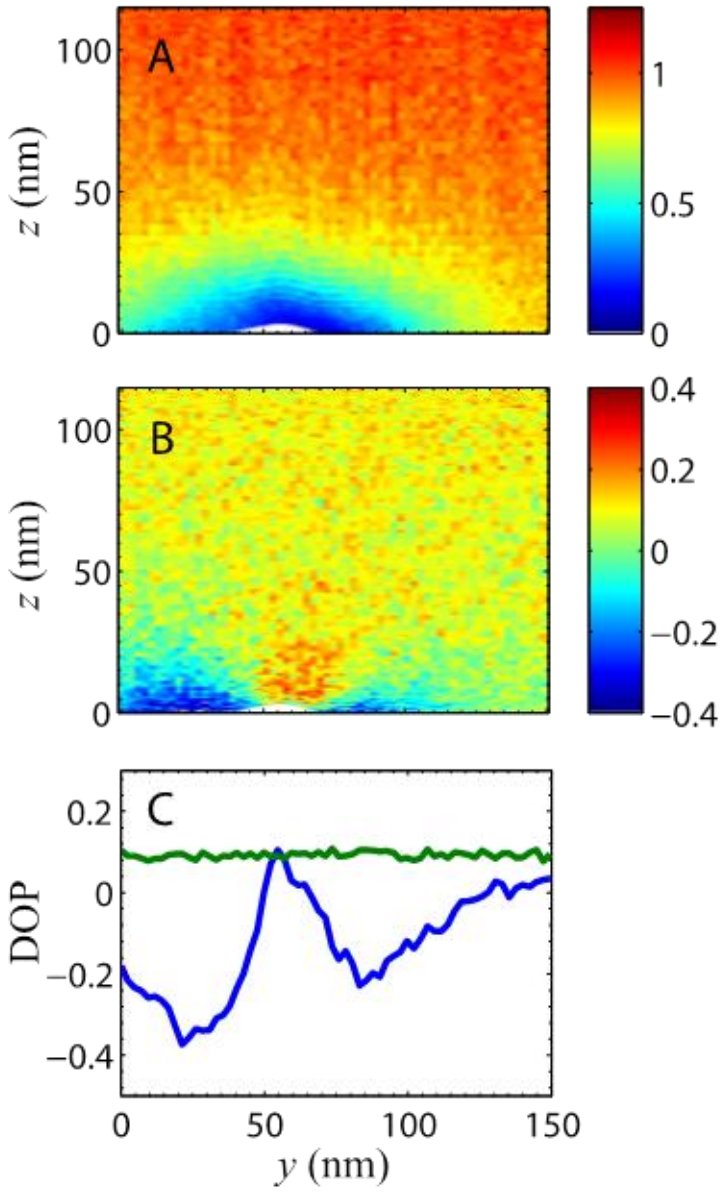

Figure 5.9 Rotation of QD emission polarization due to a gold AFM tip. A) Total fluorescence signal (summed in both polarization channels) as a function of the AFM tip position in a *yz*-plane that cuts through a QD. The color scale represents the total signal normalized to the average signal when the tip is far from the sample ($z > 50$ nm) for each lateral position of the tip. B) Calculated DOP using Equation 5.1. C) Green line: DOP values when the tip is high above the sample ($z > 50$ nm); blue line: DOP values when the tip is close to the surface ($z < 2$ nm).

5.7.2 Phase and Magnitude of E_z in the Near-Field

Figure 5.10 shows the phase and magnitude of the vertical field component, E_z for a simulated dipole tilted by 45^o relative to the vertical, which is same orientation as that used in Figure 5.2 and Figure 5.5. This simulation demonstrates that the phase of the optical field relative to the oscillation phase of the dipole depends very sensitively on the location of the field point being sampled in the near-field zone. For the tilted source dipole represented in Figure 5.10, the optical phase (and magnitude) pattern is also tilted, which provides an explanation for the asymmetry in the simulated directionality and DOP values in the $+x$ vs. $-x$ directions (cf. Figure 5.2 and Figure 5.5).

In the electrostatic limit (neglecting retardation effects), the induced dipole in a nanoparticle sitting in the phase zones marked I and III will have a dipole moment that is anti-aligned (out of phase) with the source dipole whereas a nanoparticle sitting in the phase zone II will have a dipole moment aligned (in phase) with the source dipole. These conditions exist only when the size of nanoparticle is small enough to be within each phase zone. Although the scanning tip we use has a semi-infinite geometry, which perturbs the phase in a complicated way, these plots provide a qualitative explanation for the asymmetry observed in Figures 5.2 and 5.5. Note that a tilt and asymmetry in the tip geometry will also quantitatively change the DOP and directionality curves.

5.7.3 Simulation Details

We used the finite-difference time domain (FDTD) simulation package from Lumerical Solutions Inc. to model our experimental measurements and predict emission patterns both in the presence and absence of a gold tip. A schematic of the simulation geometry is shown in Figure 5.11A. In the simulation, a linear Hertzian dipole was

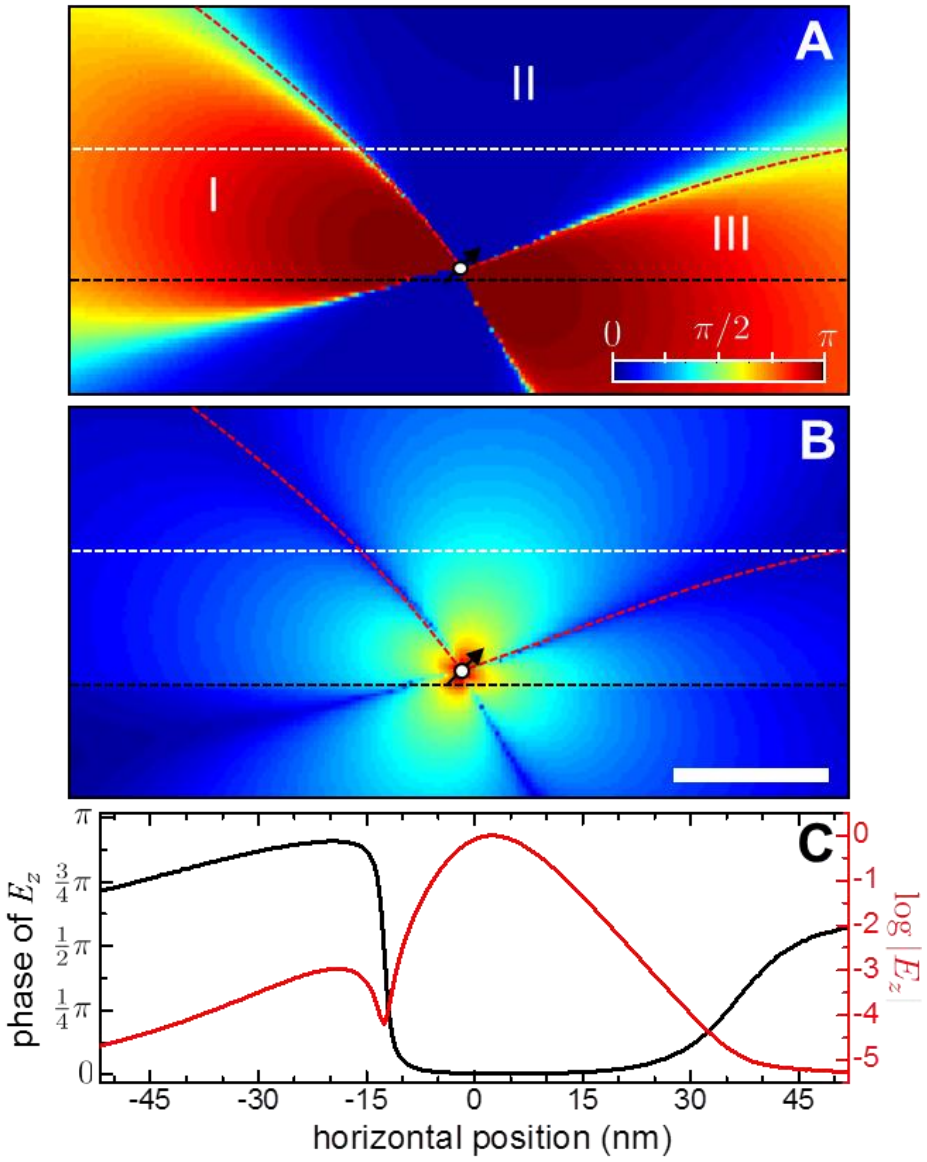

Figure 5.10 Vertical field, E_z, in the near zone of a Hertzian dipole positioned above an air-glass interface. A) Phase of E_z relative to the dipole oscillation $\phi_z = \text{atan}[\Im(E_z)/\Re(E_z)]$. B) Magnitude of E_z plotted on a log scale (color scale not shown for simplicity). Panels A and B measure 100×50 nm, and the scale bar in panel B is 20 nm in length. The dipole is positioned 2 nm above the interface (represented by the black dashed line) and is tilted by 45°. The red dashed lines delineate the phase boundary in the near-field. C) The phase (black curve) and the magnitude of E_z plot across the white line (z = 17 nm) in panel A and B, respectively.

situated 2 nm above an air/glass interface representing the sample plane. A solid cylindrical gold cone with a 15 nm radius of curvature and full open-angle of 15^o was used to represent the AFM tip. The actual AFM probes used in the experiments were commercially available Budget sensors gold-coated tips (part no: Multi75GB-G). The simulation domain was enclosed by a perfectly matched layer (PML) boundary to prevent reflections and backscattering from the domain edges.

The real and imaginary parts of the refractive index for the gold tip were taken as n = 0.23 and k = 3.02, respectively, for a free-space wavelength of 605 nm [109, 110], and the refractive index of glass was taken as n = 1.5 for all simulations. A near-field monitor (NFM) was placed 50 nm below the interface within the glass to capture the field components required to project the far-field radiation pattern: the near-field components are projected into the far-field in polar coordinates ($E_r, E_\theta, and\ E_\phi$) onto a hemispherical surface of radius 1 meter within the glass medium, as shown in Figure 5.11B. In the near-field, the magnitude of E_r cannot be neglected and is in fact sometimes the dominant field component; in the far-field, however, E_r is parallel to the propagation direction, and its magnitude is negligible. The infinity-corrected objective lens refracts the emitted light, thereby flattening the wavefronts and collimating the collected emission. Thus, the field components E_θ and E_ϕ are transformed to the components E_x and E_y, which are transverse to the optic axis and aligned with the two polarization channels of the detection system:

$$E_x = -\frac{E_\phi sin\phi + E_\theta cos\phi}{\sqrt{cos\theta}} \tag{5.4}$$

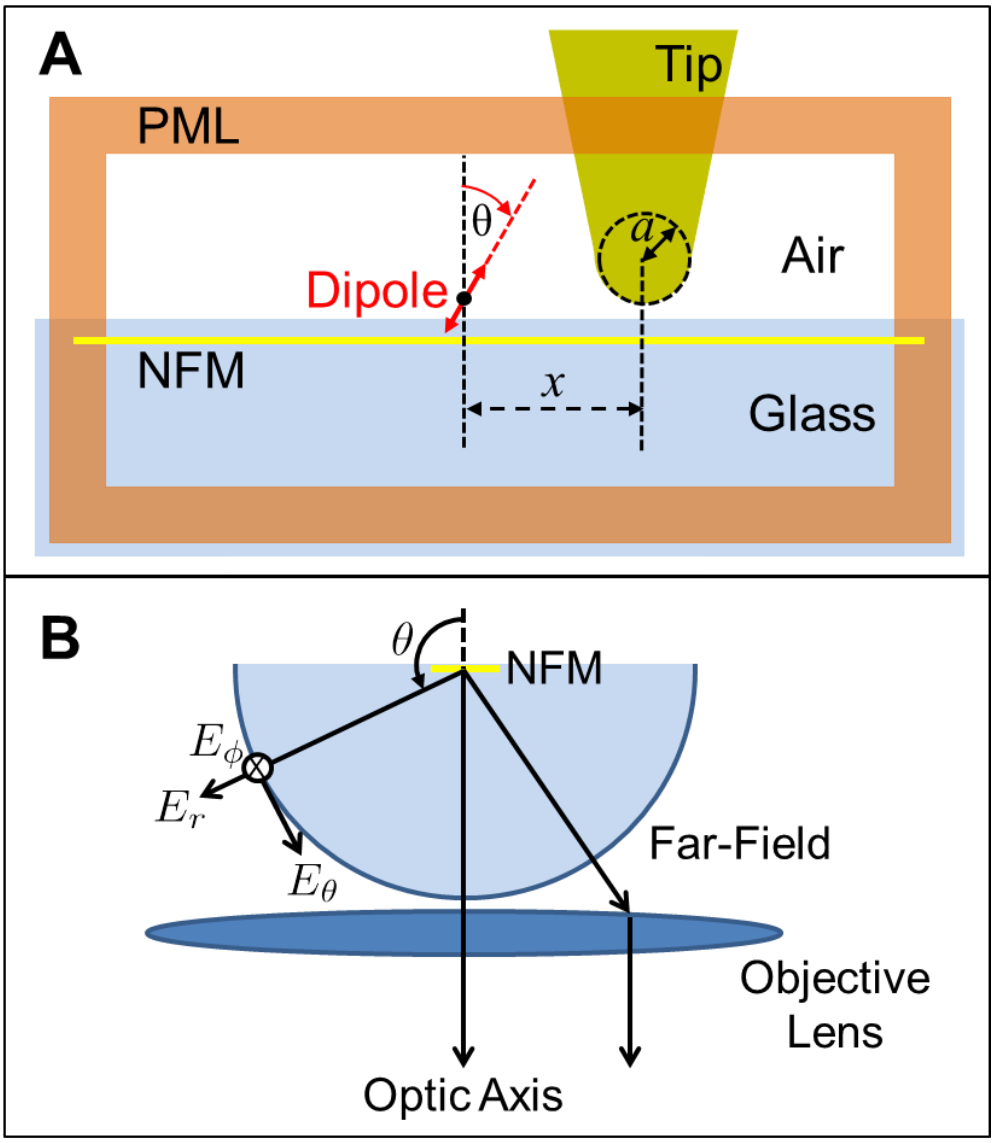

Figure 5.11 Simulation and far-field projection geometries. A) A PML boundary confines the simulation domain. A conical gold tip is situated on the air side of the interface and extends beyond the PML boundary. A Hertzian dipole source is situated 2 nm above the air/glass interface and a near-field monitor (NFM) is situated 50 nm below the interface on the glass side. B) The field from NFM is projected onto a hemispherical surface of radius 1 meter, and the objective lens transforms the spherical field components, E_θ and E_ϕ, into transverse components aligned with the two polarization channels, E_x and E_y.

$$E_x = \frac{E_\phi cos\phi + E_\theta sin\phi}{\sqrt{cos\theta}} \tag{5.5}$$

The factor $1/\sqrt{cos\theta}$ is required to conserve energy as the light passes through the lens. In our simulations, we take into account the maximum propagation angle that can be collected by the objective lens (NA = 1.4).

5.7.4 Resonance Effects from a Dipole Antenna

Figure 5.12 shows the DOP (A) and directionality (B) for a rounded cylindrical antenna with 15 nm radius of curvature, and 100 nm long (shown in Figure 5.12B) for different lateral positions relative to a vertically oriented dipole emitter. The black, red, blue, magenta, and green curves represent emission wavelengths of 480, 580, 605, 660, and 700 nm wavelengths, respectively. In contrast to the AFM tip, the dipole antenna supports plasmons resonance with resonance scattering occurs at ~ 660 nm wavelength for the dipole antenna we used here (see Appendix F). Due to the resonant scattering of dipole antenna, the directionality gets enhanced again at 660 nm wavelength (magenta curve in Figure 5.12B) with poor polarization control. Compared with dipole antenna (Figure 5.12), a sharp tip yields much better directional control and polarization control over a broad wavelength range (Figure 5.7A and C).

5.7.5 Comparing Redirection for Gold and Aluminum Tips

Figure 5.13 shows the simulated back-focal images for gold (Au) and aluminum (Al) tips for a dipole tipped by 45^o in the *xz*-plane when the tip is located at x = +20 nm and x = +50 nm relative to the dipole location. The Au and Al tips are identical in geometry. For the Au tip, the maximum directionality (D_x = 12 dB) occurs when the tip is

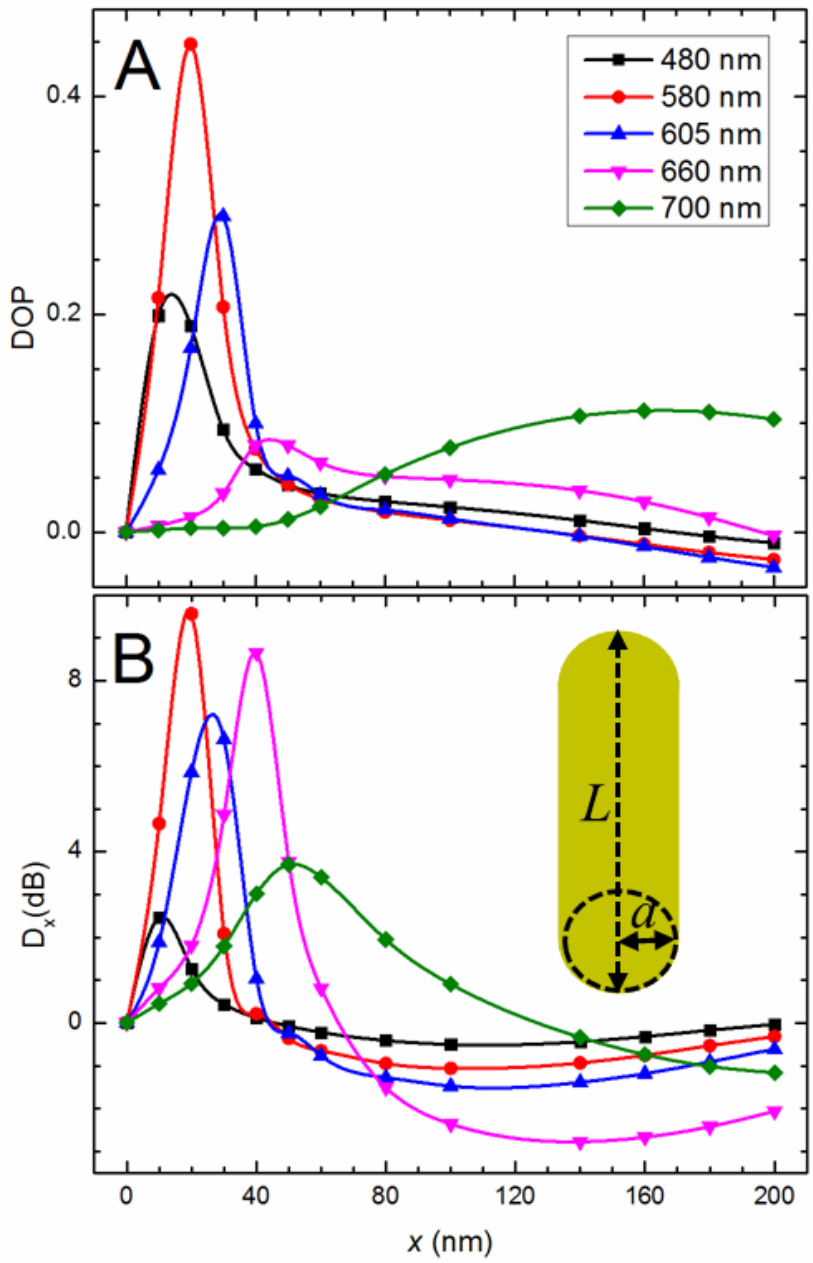

Figure 5.12 DOP and directionality (D_x) curves for a vertical dipole emitter with five different vacuum emission wavelengths. For both graphs, the black, red, blue, magenta, and green curves represent emission wavelengths of 480, 580, 605, 660, and 700 nm, respectively. Panels (A) and (B) correspond to DOP and directionality for a gold cylindrical dipole antenna with a = 15 nm and L = 100 nm, respectively. The horizontal axis corresponds to the lateral displacement of the rounded-cylinder apex relative to the dipole position. The curves are guides for the eye.

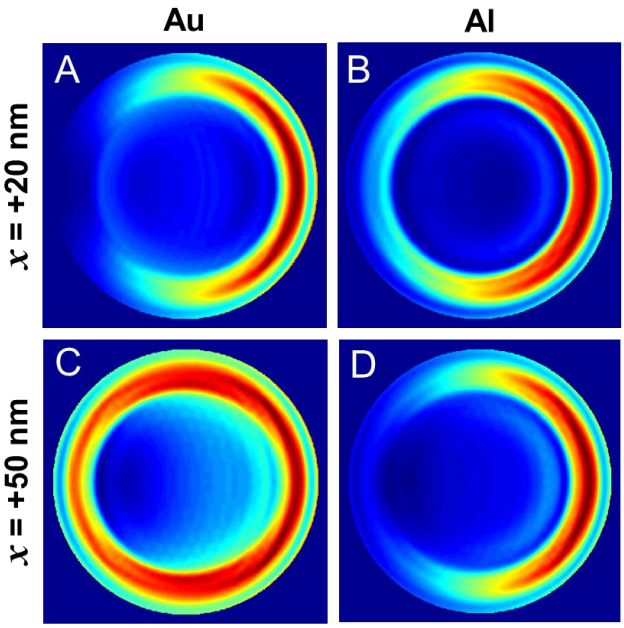

Figure 5.13 Comparing simulated back-focal images for Au and Al tips. In all simulated images, the source dipole is tilted by $\theta = 45^o$ in *xz*-plane. In panels A and B, the tip is located at x = +20 nm to the side of the dipole. In panels C and D, the tip is located at x = +50 nm.

at x = +20 nm, which corresponds to the highly asymmetric emission pattern shown in Figure 5.13A. At this same location (x = +20 nm), the Al tip induces less directionality (Figure 5.13B): due to its larger charge density, the image dipole in Al is stronger than in Au, so at this distance, the pattern more closely resembles that of a vertical dipole (i.e., scattering from the tip). On the other hand, at x = +50nm the emission pattern is highly directional for the Al tip (D_x =10 dB), as shown in Figure 5.13D, while the pattern for the Au tip (Figure 5.13C) closely resembles the pattern resulting from a 45^o dipole in absence of a tip (Figure 5.5∞). At this larger distance, the strength of the source and image dipoles is similar in Al, but the image dipole in Au is much weaker. The larger charge density also causes a change in the phase lag between the source and image dipoles for the Al tip compared to the Au; this also affects the resulting emission pattern.

5.7.6 Repeatability of DOP Measurements with Different Tips

Figure 5.14 shows seven different DOP approach curve measurements. Each measurement was made on a different QD using a different gold-coated AFM tip, and the measurements clearly demonstrate repeatability across a variety of tips. Since the distribution of DOP values when the tip is far above the sample is determined by the orientation of the QD emission dipole, the distribution of starting (large tip-height) DOP is broad (e.g., Figure 5.4), and includes both positive and negative values depending on whether the effective dipole moment lies in the *xz*- or *yz*-plane, respectively. As each tip approaches a QD from above, the DOP is driven towards zero since most of the emission is then scattered from the tip, which has a vertical effective dipole orientation, as described in the manuscript. The repeatability of these measurements across several different tips demonstrates that the particular tips used to acquire 2D DOP maps (Figure 5.2 and Figure 5.9) are not special in any way, but rather quite representative.

To characterize the "sharpness" of the tips used in this work, we performed a simple calibration whereby we assumed the AFM tip had a radius R and the QD a radius r, where $r<R$, as shown in Figure 5.15. In this model, when the tip is scanned over a QD to make an AFM image, the measured height ($H=2r$) and lateral dimension (w) of the QD are related to the tip radius according to the relation $w^2=8RH$ [111]. Using this relation, we determined the radius of curvature of the tips in this work to vary from 14 to 25 nm; this agrees with the specifications for these tips provided by the manufacturer: tip radius <25 nm with a gold coating thickness of ~ 70 nm, and a half-cone angle of 10^o at the tip apex. The particular tips used for Figure 5.2 and Figure 5.9 both had $R\sim 16\pm 3$ nm.

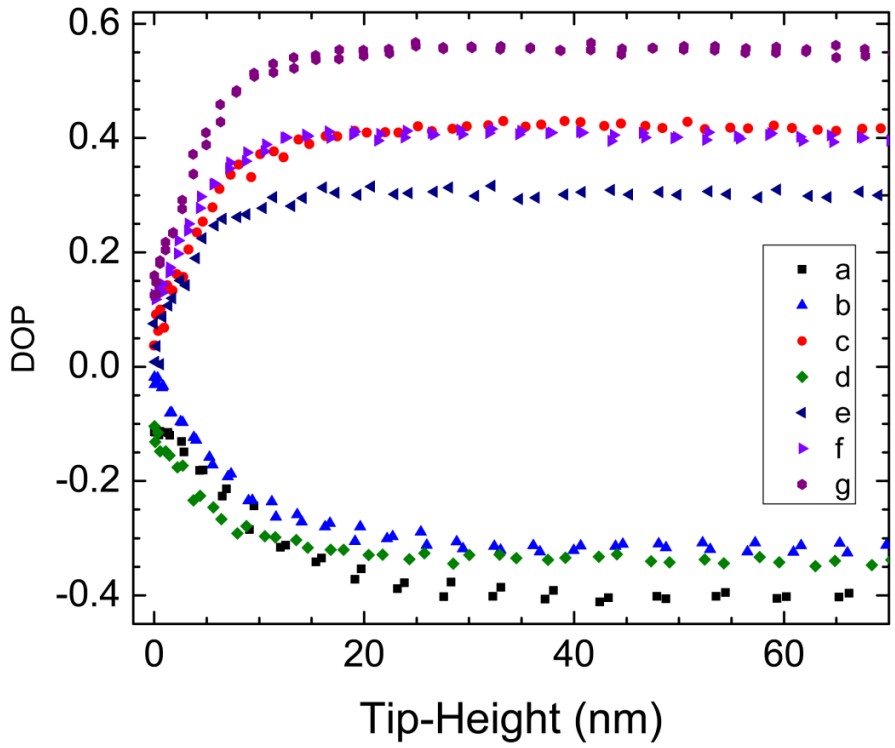

Figure 5.14 Vertical DOP approach-curve measurements for seven different gold tips. These measurements were performed on different QDs. The length scale, shape, and consistent suppression of DOP magnitude for all tips demonstrate that the tips used to produce the 2D DOP maps shown in Figure 5.2 and above were not particularly special, but rather represent typical data.

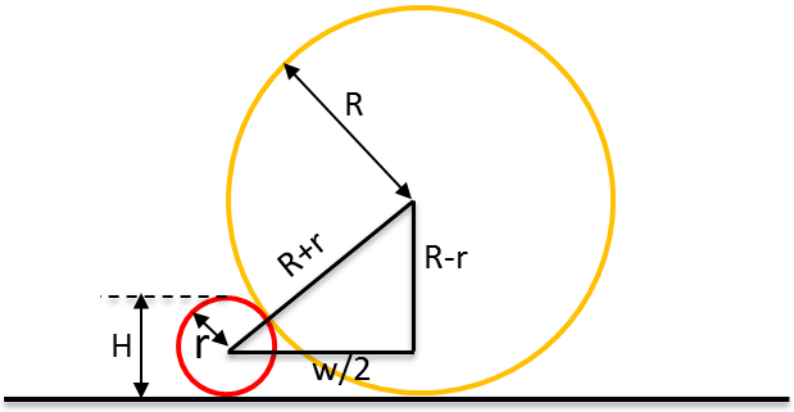

Figure 5.15 Indirect measure of tip radius using measured height (H) and contact width (w) in an AFM image of a spherical sample.

CHAPTER 6

ANGULAR EMISSION PATTERN FROM A SINGLE EMITTER

6.1 Introduction

In the previous chapter, I mentioned the difficulty of implementing experimental back-focal imaging as a function of the tip-sample distance. As the atomic force microscope tip is oscillating with the high frequency (60-70 kHz), the emission pattern will be averaged over the oscillation cycle. Since the tip spends most of its time more than 10 nm from the sample surface, this averaging makes it difficult to obtain back-focal images with sufficient signal-to-noise ratio. To capture a clean back-focal image, we could fix the tip at a specific height on a particular location. This is not possible with the cantilever-based AFM in our lab, but would be using an AFM with shear force feedback. Emitter-antenna systems have been studied previously using an antenna attached to a shear-force microscope and observing the radiation pattern as a function of the antenna height [12, 13, 72, 93, 107]. As we have demonstrated, when using sharp tips, the polarization and directional control occurs only when the tip is within a few nm of the sample. The drawback to using a shear force microscope is that it cannot reproducibly approach the sample to within 2-3 nm. In contrast, our cantilever-based system can approach the sample to within 1 nm, but cannot be maintained at a specific height.

In this chapter, I will discuss the motivation for experimental back-focal imaging. The progress in the development of experimental techniques towards back-focal imaging

and some results are discussed. Finally, I discuss efforts and limitations to implement back-focal imaging into our system as well as the future outlook.

6.2 Motivation

In the previous chapter, it has been shown that the emission pattern, in general, is steered toward the tip when the tip lies on the side of the emitter. When the tip is approaching directly above a dipole emitter, the resulting emission pattern highly depends on both the orientation of dipole relative to the tip and relative distance between the tip and dipole. Figure 6.1 illustrates that when the tip is at $z = 2$ nm above the dipole, the directionality (described by Equation 5.2) is very small and the emission pattern for the different dipole orientation is radially symmetric (not shown here). As the tip moves up, the emission pattern becomes more directional (increasing directionality) and reaches a maximum at a particular height that depends on the dipole polar angle. An example of a back-focal image as a function of tip-height for a particular dipole orientation is shown in Figure 6.2.

Figure 6.2 shows the back-focal image for a 68^{o} degree dipole at different tip-heights. At $z = 2$ nm, the emission pattern is highly symmetric (Figure 6.2b). The emission pattern becomes asymmetric and directional as the tip moves up (Figure 6.2d, e, $z = 8, 12$ nm). When $z = 20$ nm, the directionality decreases and the emission pattern evolves as if there was not a tip (Figure 6.2∞). Such dynamic modification of the emission pattern with the height of the tip directly above a dipole emitter is fundamentally interesting. This simulated result is not discussed in literature so far as we know. Thus, this result motivates us to investigate the development of an experimental technique for back-focal imaging as a function of tip-height using nanometer precision.

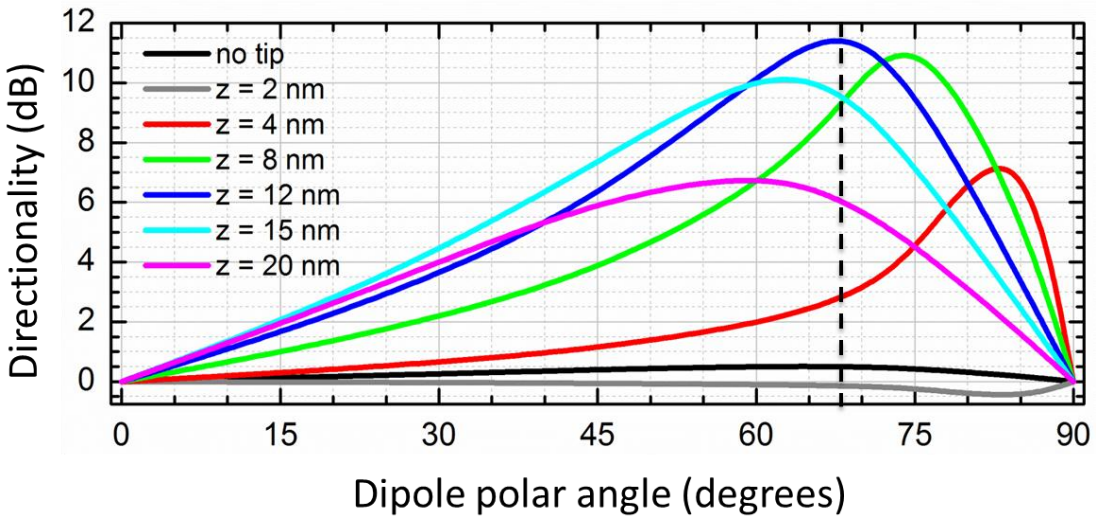

Figure 6.1 Directionality for different dipole orientations in the xz-plane. The color represents the tip-height where the black curve represents the result without a tip. The maximum directionality is achieved when the orientation of the dipole is at ~68° (black dotted line) with a tip-height of ~12 nm.

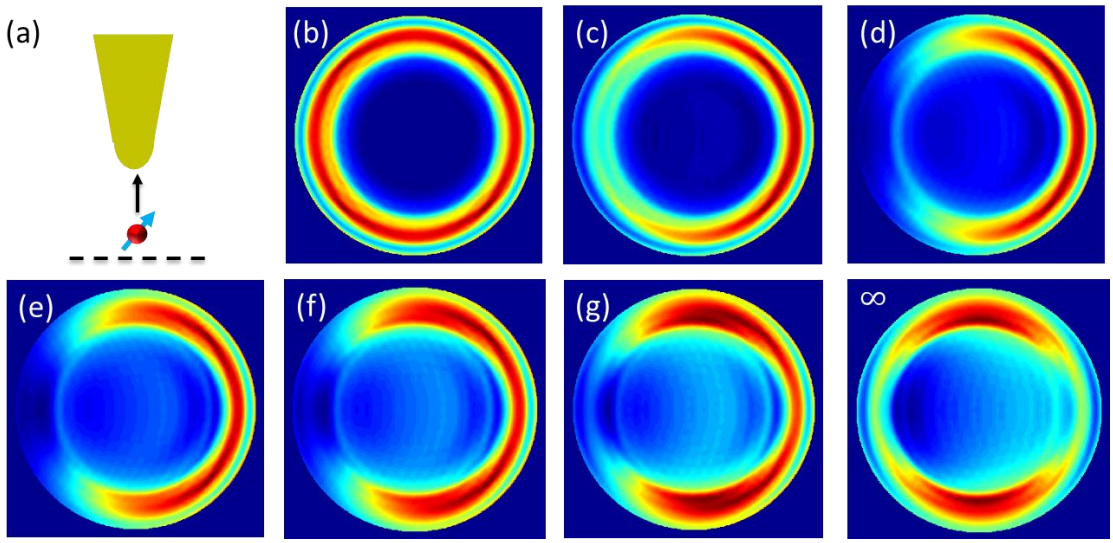

Figure 6.2 Back-focal images for 68° dipole in *xz*-plane. (a) Schematic of a gold tip and a tilted dipole. Images (b) – (h) represent the back-focal image when the tip is at 2, 4, 8, 12, 15, and 20 nm above the dipole, respectively. Image ∞ represents the back-focal image without a tip. In the simulation, the dipole is situated 2 nm above the air/glass interface in the air side.

6.3 Experiment

Back-focal imaging at a specific tip-height can be achieved if we pulse the excitation laser for a fraction of the tip oscillation period. In this section, I will discuss how to create a short pulse in a continuous-wave (CW) laser synchronized with the tip's oscillation.

6.3.1 Excitation Laser Pulsing

The AFM's deflection signal is calculated by the difference between the upper and lower voltage in the quadrant photodiode (cf. Section 3.1). Therefore, the deflection signal reflects the actual vertical motion of the tip. The signal itself is an analog sinusoidal signal corresponding to the simple harmonic motion of the tip. There can be large variations in the deflection signal amplitude depending on different types of tips or the reflectivity on the back of the cantilever. Due to this variation of amplitude and some electronic phase delays within the system, it is difficult to identify the particular phase that corresponds to tip-sample contact.

To correlate the phase corresponds to tip-sample distance; the deflection was converted into a standard TTL signal using custom-built electronic circuitry. The TTL signal is compatible with the data acquisition card from National Instruments (PCIe-6340, or USB-6210). The rising edge of the TTL signal is used to generate a subsequent TTL pulse, which is used to pulse the CW laser (termed the laser pulsing signal), as shown in Figure 6.3. The duty cycle ($\Delta t/T$) of the laser pulsing signal will determine the fraction of time that the laser will illuminate the sample over the period of oscillation. The phase of the laser pulsing signal relative to TTL signal is swept over the oscillation period using a labview program.

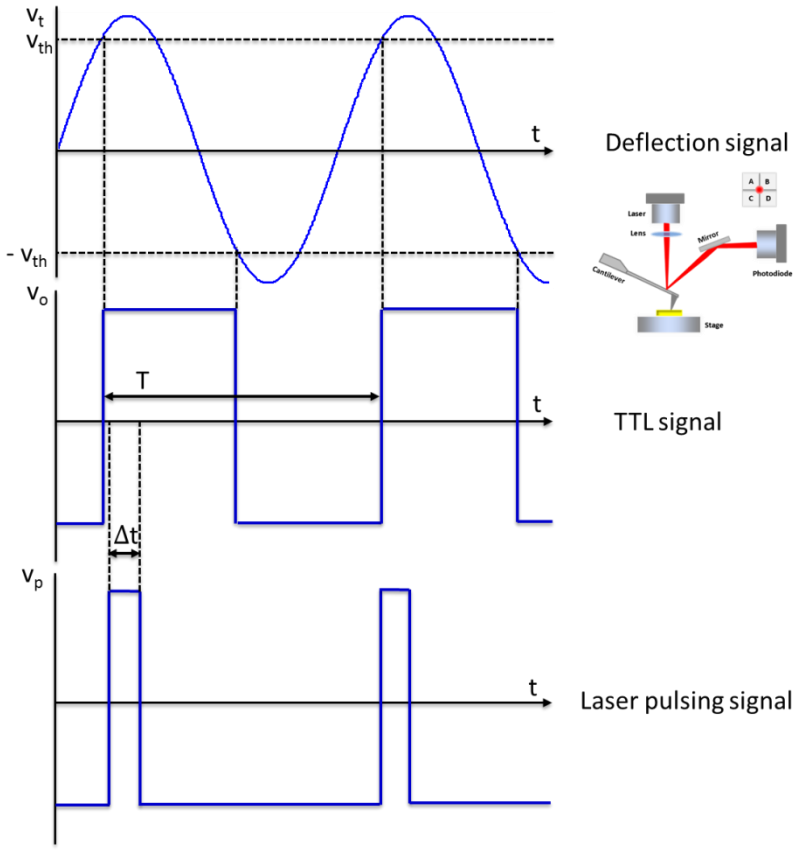

Figure 6.3 Schematic of the generation of a laser pulsing signal. The deflection signal is a sinusoidal voltage associated with oscillation of the tip. The sinusoidal wave is converted to a square wave (TTL signal) using custom built circuitry. The TTL circuit is time stamped with a high frequency (80 or 100 MHz) digital clock with subsequent generation of another TTL laser pulsing signal.

Figure 6.4 shows the schematic of the laser pulsing system. The laser pulsing signal generated from the data acquisition card is connected to the Acoustic Optics Modulator (AOM). The active laser pulsing signal will activate the controller to send the voltage to the piezo-electric transducer, which creates the pressure wave in the quartz crystal attached to it. The quartz crystal acts as a diffraction grating. The first-order diffracted beam, which is spatially separated from the zeroth order beam, is fiber-coupled and sent to the microscope system. In this configuration, the first-order diffracted laser

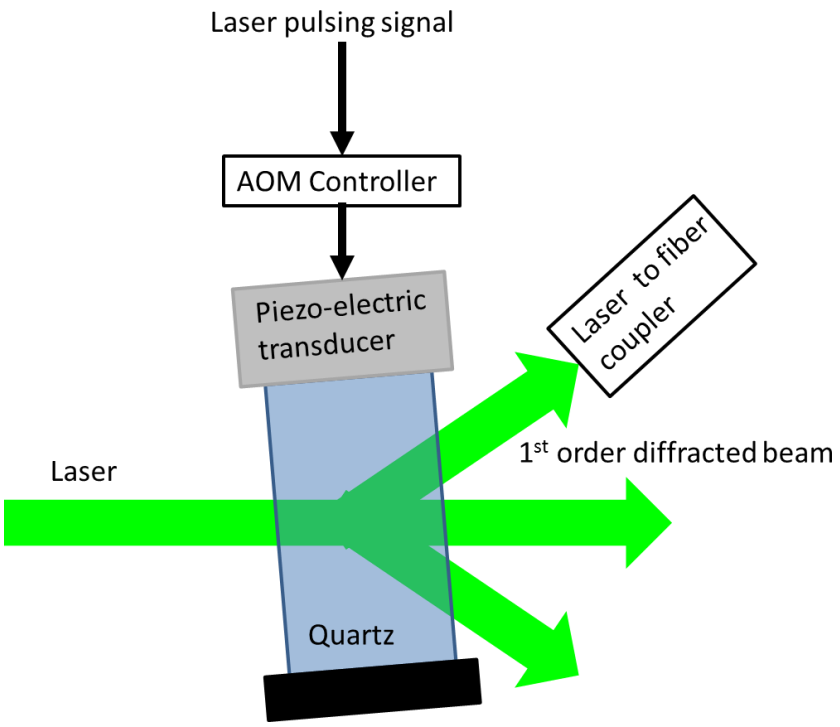

Figure 6.4 Laser pulsing layout. The high of TTL signal activates the acoustic optic modulator (AOM) controller, creating a dispersion of incident laser. The quartz crystal is slightly tilted from normal incidence so that the 1st order diffraction beam can accommodate most of the incident laser power (more than 75%).

beam will be turned on as long as the laser pulsing signal is active/high.

The AFM tip we used has an oscillation frequency of ~65 KHz. The sampling clock's frequency of the data acquisition cards are ~100 MHz. The response time of the AOM is on the order of ~20 nanoseconds; in other words, the AOM has frequency response of ~40 MHz. The oscillation amplitude of the tip can be easily divided into ~50 laser-pulsing steps ($n = T/\Delta t \sim 50$) because the frequency of the sampling clock (NI card) and frequency response of AOM are nearly three orders of magnitude higher than the oscillation frequency of the tip.

6.3.2 Phase and Tip-Height

To determine the oscillation phase (and height above the sample plane) of the tip, the interaction of the tip with an emitter is measured. Figure 6.5 shows the counts of emitted photons as a function of laser pulsing phase (relative to the rising edge of the first TTL signal shown in Figure 6.3) in terms of clock ticks of the data acquisition card. A laser pulse is swept over a complete oscillation cycle of the tip with many segments ($n = T/\Delta t \sim 30$) while the corresponding photon counts of each pulse segment are plotted with the clock number. The number of photon counts reduces when the tip gets closer to the sample due to nonradiative energy transfer from the emitter to the tip [104, 112]. The minimum photon count corresponds to tip-sample contact. By fitting a power law function, we can find the phase that corresponds to the tip-sample in contact. A sinusoidal fitting function can be used find the specific phase corresponding to a given tip-height.

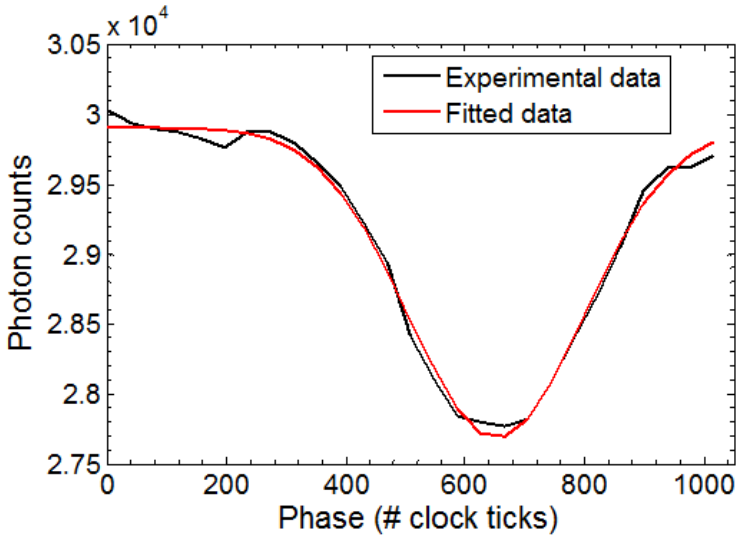

Figure 6.5 Photon counts as the function of tip-height with a gold tip oscillating on top of a single quantum dot. The minimum photon counts correspond to the tip-QD in contact. The laser pulse (pulse duration of 490 ns) sweeps over the complete oscillation of the tip with total steps (n) of ~30. The black line represents the experimental data and red line is a fitted exponentially decaying function.

6.4 Experimental Back-Focal Imaging

Back-focal imaging is a way to map the radiation pattern of a given emitter [90, 113]. The experimental setup for back-focal imaging is discussed in Section 3.9.2. In this section, I will discuss the emission pattern for an isotropic emitter, an individual quantum dot, and modification of the back-focal image due to the presence of a gold tip.

6.4.1 An Isotropic Emitter

The optical transition rate for a quantum emitter is proportional to $|\mathbf{p} \cdot \mathbf{E}|$, where $\mathbf{p}$ is the dipole moment of the transition dipole and $\mathbf{E}$ is the excitation electric field at the location of the dipole [114]. The transition dipole of a single molecule generally aligns in a specific direction, creating a linear transition dipole in both absorption and emission. Combining a large number of such single molecules with random orientation into a limited volume creates an isotropic emitter both in absorption and emission. A fluorescent bead (Carboxyl latex beads of size 20 nm diameter) consists of a large number of single molecules (up to 200). The emission pattern from such a fluorescent bead captured by a high-NA objective is radially symmetric due to the superposition of emission patterns for each single molecule, as shown in Figure 6.6. The back-focal image consists of a annular ring with an inner diameter corresponding to the critical angle for total internal reflection at the glass/air interface [30, 115]. The outer ring in Figure 6.6 corresponds to the maximum collection angle of the microscope objective.

6.4.2 Isolated Quantum Dots

Due to strong quantum-confinement effects in semiconductor nanocrystal quantum dots, photo-excited excitons behave similar to single molecules in terms of their emission properties and quantum nature. CdSe/ZnS quantum dots, particularly (nearly

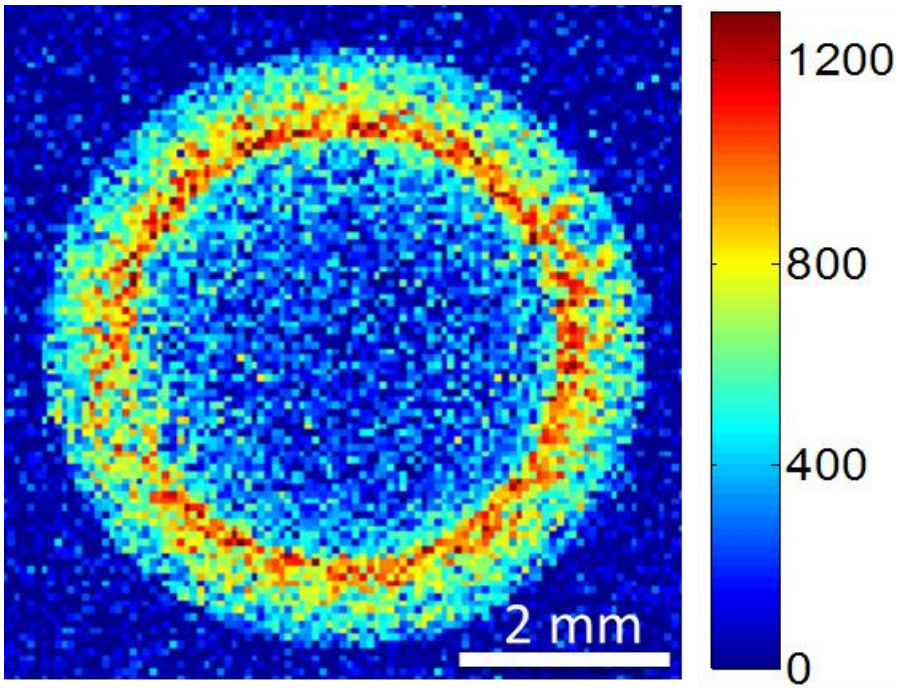

Figure 6.6 Back-focal image of a single fluorescent bead from *Molecular Probes*.

spherical ones), do have some unique emission properties: when excited above the band edge, the absorption dipole is isotropic [116] while the emission dipole is 2D degenerate [87, 88, 117, 118]. The excitation polarization is decoupled from the emission polarization in that changes in the excitation polarization lead to no observable change in the emission [117].

Figure 6.7 summarizes the structure of CdSe nanocrystals and some emission properties. The emission dipole is characterized by a "bright plane", in which the emission polarization is 2D degenerate and a "dark axis" with no emission polarized along that axis. The "dark axis" is slightly elongated and aligns along the c-axis of the wurtzite crystal whereas the "bright plane" is perpendicular to the dark axis (Figure 6.7a). The projection of the "bright plane" on the sample plane is ellipsoid. The ratio of the major to the minor axis depends on the angle between the c-axis and the *z*-axis (Figure

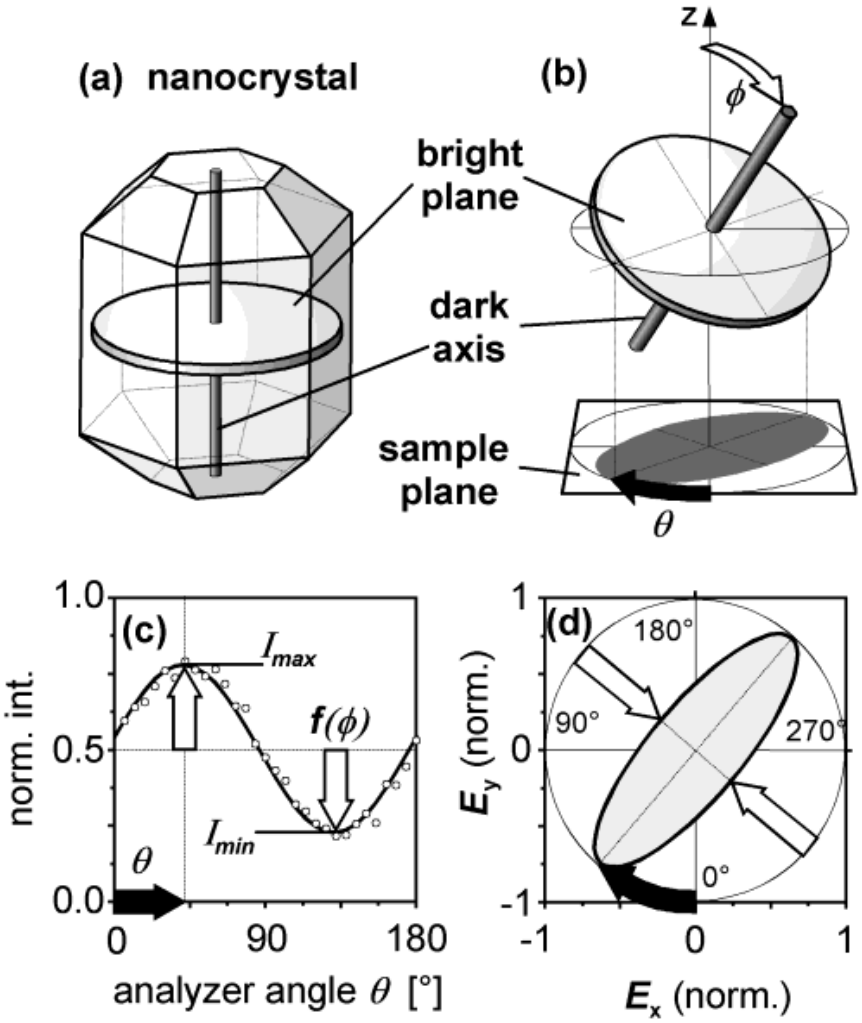

Figure 6.7 Structure and emission polarization modulation for a CdSe nanocrystal. (a) A hexagonal 3D CdSe nanocrystal has a 1D dark axis (c-axis) along the long axis of nanocrystal with a 2D transition dipole (bright plane) perpendicular to it. (b) The projection of the bright plane onto the sample plane becomes an ellipsoid with the ellipticity depending on the tilt angle (∅). (c) Modulation of the emission intensity as the function of a rotating polarizer with θ being the angle of polarizer. (d) Polarization ellipsoid calculated from the intensity modulation function drawn in c. This figure is adapted from [87]

6.7b) depicted as ϕ. When a rotating polarizer is placed in the emission path, the intensity becomes modulated as a function of polarization angle θ. The modulated intensity can be mapped to the polarization ellipsoid, specifically, the projection of the "bright plane" on the sample plane (Figure 6.7d). The polarization modulation measurement is related to the anisotropy in the polarization and is measured by the degree of polarization as discussed previously in this dissertation.

The emission patterns for the 2D degenerate dipole at the back-focal plane are different as compared to a 1D dipole. For example, the back-focal image will be radially symmetric (Figure 6.2a) when the 'bright plane" is parallel to the sample plane, corresponding to the polarization ellipsoids becoming a circle (Figure 6.7d). This emission pattern corresponds to the vertical dipole, as in the case of the 1D dipole. When the orientation of the "bright plane" is not exactly parallel to the sample plane, any other orientation leads to an asymmetric back-focal image. A comparative study of emission patterns for 1D and 2D degenerate dipoles near the dielectric interface was experimentally measured and theoretically predicted by Brokmann *et al.* [118].

Figure 6.8 illustrates the back-focal image of an individual quantum dot. In this experiment, the samples were prepared by diluting CdSe/ZnS QDs (from Invitrogen) in toluene and dispersing them on a glass coverslip. An individual QD is illuminated with a Gaussian beam (Section 3.3) at $\lambda_{exe} = 543$ nm and a back-focal image of the emitted photons was detected with the CCD. The emission peak of the QDs is at 605 nm. The back-focal images shown here demonstrate an asymmetric emission pattern and a dipolar emission pattern. The orientation of the "bright plane" varies from QD to QD so that the emission pattern of each individual QD is different.

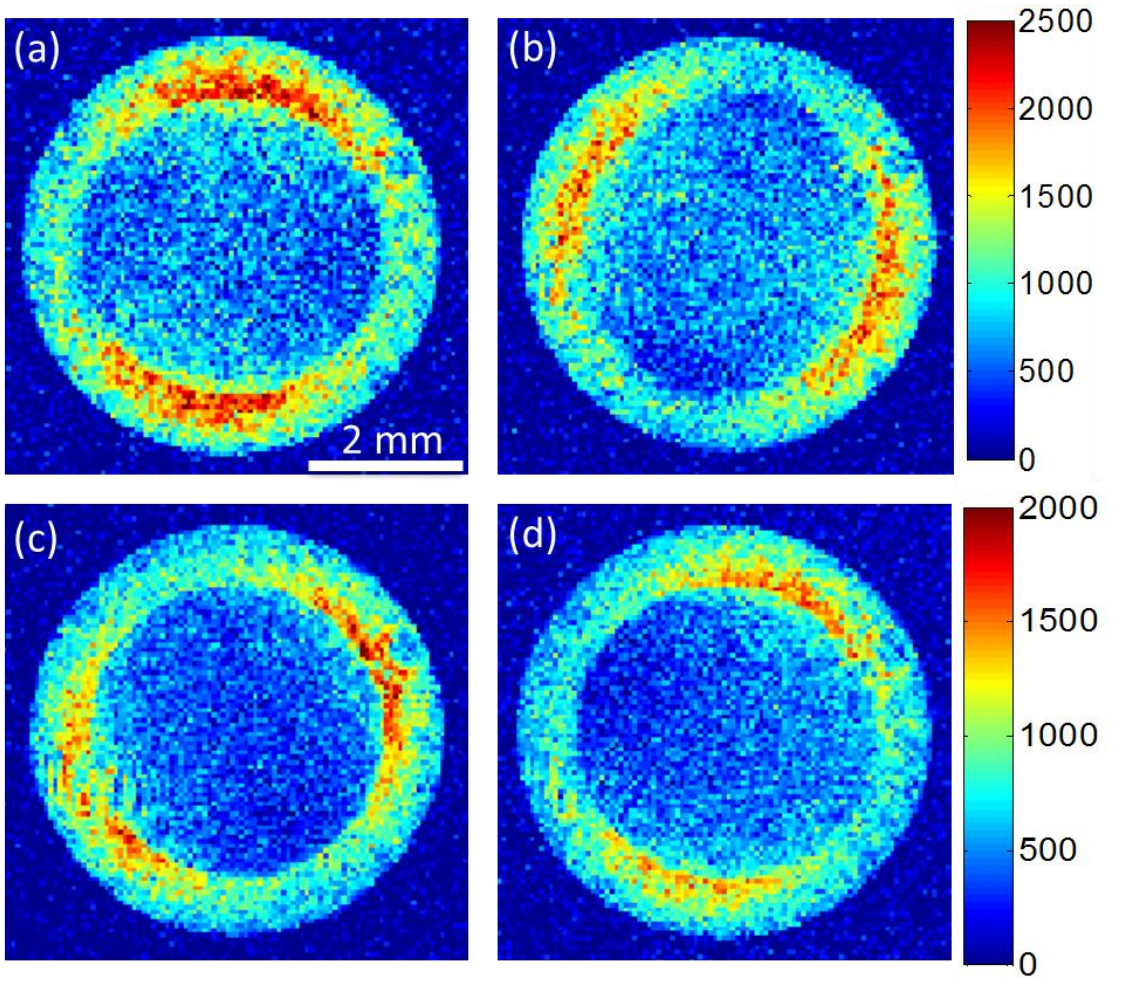

Figure 6.8 Back-focal images for four different isolated quantum dots. The orientation of the emission dipole moment on the sample plane will determine the emission pattern of QDs. The top and bottom color scale represent the intensity for (a)-(b) and (c)-(d), respectively.

6.4.3 Emission Pattern due to Presence of Tip

Figure 6.9 illustrates the effect of tip-height on the emission pattern of a QD. When a gold-coated AFM tip is far above the QD, the emission pattern is not affected (Figure 6.9a) and looks similar to the back-focal images shown in Figure 6.8. When the tip is in near-contact with the QD, the back-focal image is modified. This experiment was performed by changing from tapping mode to contact mode in the AFM system (Section

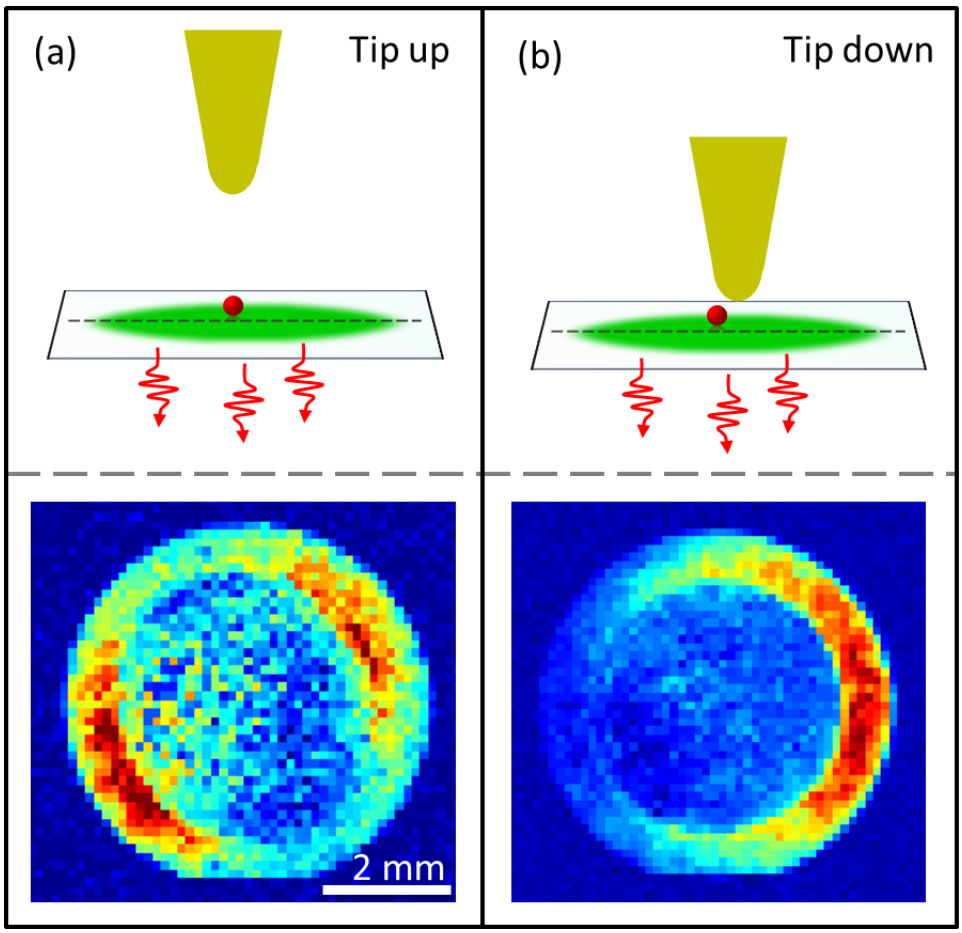

Figure 6.9 Dependence of back-focal image of QD emission on AFM tip-height. (a) A gold-coated AFM tip is high above the QD where it has no effect, yielding an emission pattern similar to those shown in Figure 6.8. (b) Back-focal image for the same QD when the tip is in near-contact with the QD. The emission pattern is modified and becomes more asymmetric, presumably due to a small lateral (rightward) offset of the tip relative to the QD center.

3.1.1) and keeping the tip on the top of a QD. Simulation results illustrate that a small lateral displacement of the tip apex relative to the QD center leads to directional emission with photons steered toward the general direction of the tip (Section 5.4.2). Figure 6.9b illustrates that the tip might be slightly displaced laterally toward the right where the emission pattern becomes directional. This measured back-focal image is an experimental demonstration of the tip-induced modification of the QD emission pattern.

6.5 Limitations of Back-Focal Imaging

I have previously discussed synchronous excitation-laser pulsing to pick out different tip-heights during the tip oscillation cycle. I also examined the experimental back-focal imaging system, and utilized this system when the AFM was operated in contact mode (which does not allow for precise control of the tip-height). Combining laser pulsing and tapping mode should allow for back-focal imaging as a function of tip-height. There are some experimental limitations that make this measurement quite challenging, including the number of photons required to acquire a back-focal image of sufficient signal-to-noise ratio. Typically, the rate of detected photons from an individual quantum dot using an APD is $\sim 10^5$ counts/sec (below saturation). The oscillation frequency of the tip we used is typically on the order of ~ 65 KHz, so the period of oscillation of tip is ~ 15 μs. With the excitation pulse of step ~ 30, the excitation laser pulse duration is ~ 500 ns. Based on the calculation, the average emitted photon from a QD per excitation pulse is less than unity ($\sim 10^5 \times 500 \times 10^{-9} = 0.05$), which is not enough signals to readout for each oscillation cycle. The CCD camera (Andor iXon Model DV885) cannot be operated with expected frame rate (~100 fps). When the measurement is performed for longer integration time, the number of photons per sec with 65 KHz frequency of the tip will be $\sim 0.05 \times 65000 = 3250$. These photons will be distributed into the CCD array (20 by 20 pixels) to form the back-focal image. Although the photons are not distributed uniformly over the whole CCD array, on average, the number of photons per pixel per second is calculated to be ~ 10, which is much smaller than the pixel noise per second (dark current, readout noise) in the CCD (~ 100). Even though the measurement is performed for many oscillation cycles

(integration time on the order of ~1 min.), the measured signal-to-noise ratio is not sufficient to form the back-focal image. Many measurements using laser pulsing techniques were unsuccessful even though the background signal is carefully subtracted. Furthermore, exciting the laser on the QD for a longer time may change the QD to a less emissive state and also to the permanent measurement nonemissive state (photobleaching) [119]. Generally, we use 1-2 μWatt power to excite a QD in our microscope system; increasing power to ~10 μWatt does not yield more photons (saturation effects) and instead, the QD turns to the nonemissive state with such high power excitation. These experimental limitations necessitate the search of a bright and more photostable quantum emitter to replace QD.

6.6 Search for Bright Source

The difficulties in imaging the back-focal plane as a function of tip-height can be overcome if the signal-to-noise ratio can be improved. One way to improve the signal-to-noise ratio is to increase the emission signal. The emission signal can be improved by choosing a brighter, more photostable emitter than a QD. The emitter for our experiment should be a dipolar (nonisotropic) single-photon source, small in size with a high quantum yield.

Recently, nitrogen-vacancy color-center in nanodiamonds has been shown to be a robust, photostable single-photon source operating at room-temperature [120]. More information about color-centers in diamond is discussed in Appendix G. I obtained samples from *Adamasnano* (USA) and *Quantum Particle* (Switzerland). The samples were first characterized for the distribution of sizes and the distribution of single emitters. The fluorescence from the sample was sent to a Hanbury-Brown-Twiss (HBT)

interferometer (schematic of HBT shown in Figure 6.10) in order to record the number of coincidental photon-detection events happening with their time difference [121] .

Figure 6.11 shows the Intensity auto-correlation function, $g^{(2)}(\tau) = \langle I(t)I(t+\tau)\rangle/\langle I(t)\rangle^2$ for the emission spectrum of a QD and a nanodiamond. This function $g^{(2)}(\tau)$ measures the correlation histogram of coincidence counts versus time difference τ. A dip below $g^{(2)}(\tau) < 0.5$ indicates a single emitter. A correlation function $g^{(2)}(\tau)$ that goes nearly to zero for the QD emission indicates a single photon source (Figure 6.11a). If the dip in the correlation function is close to 0.5 (Figure 6.11b),

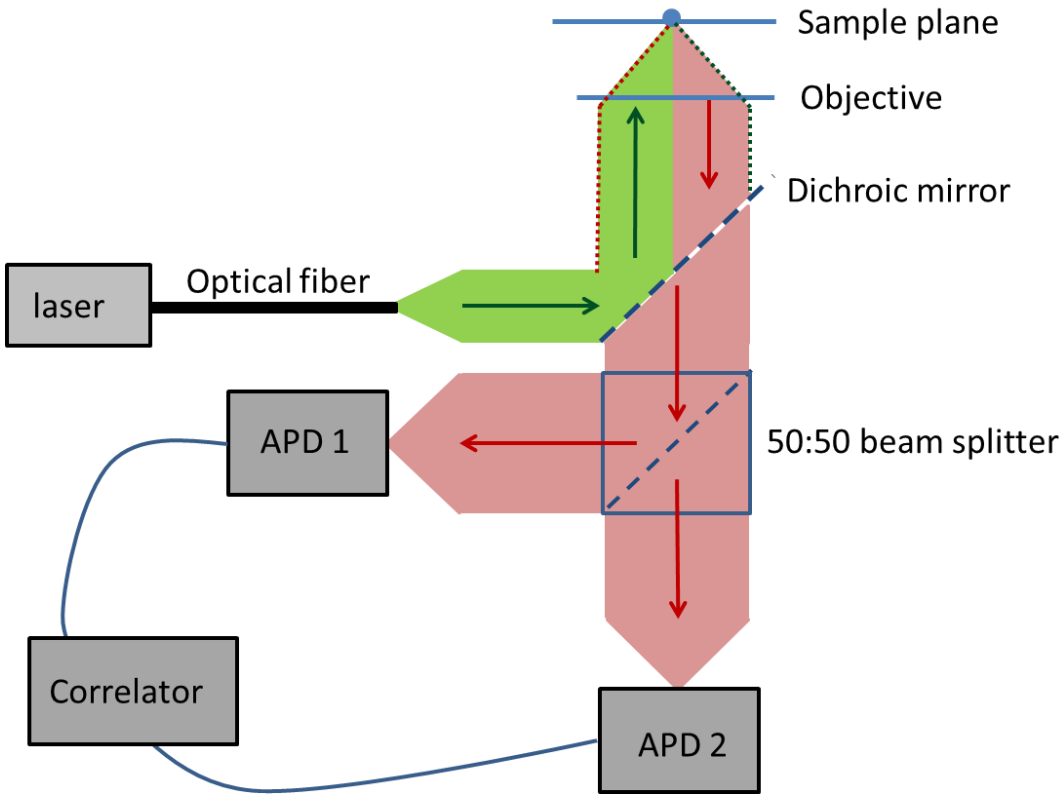

Figure 6.10 Schematic of Hanbury-Brown-Twiss interferometer. The emission is split into two paths and detected in two single photon detector APDs. The correlator measures the time-difference between photons detected by the two APDs. The TimeHarp200 photon counting card from PicoQuant was used for the photon correlation measurement.

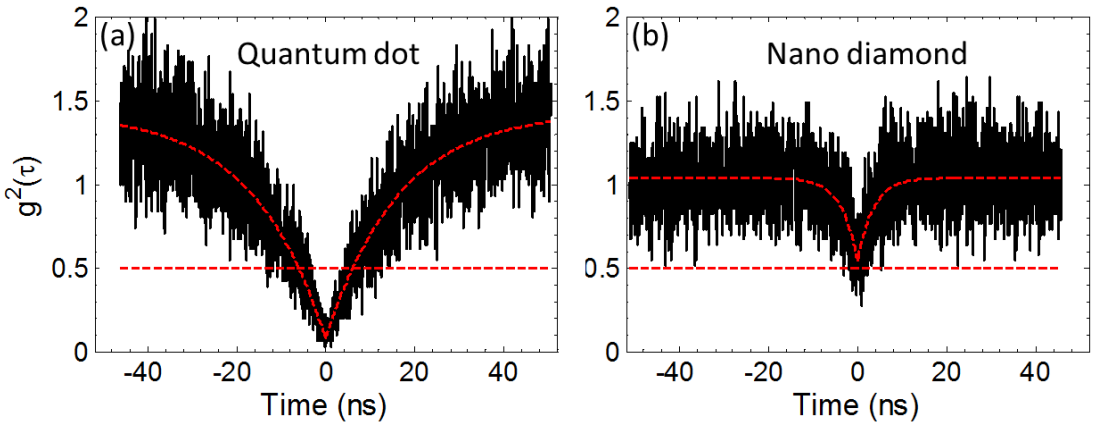

Figure 6.11 Photon antibunching experiment. (a) Second-order correlation function is plotted for the emission from a single quantum dot. The fitted function (red) goes less than 0.5, representing a single emitter. (b) Emission from a single nanodiamond. The second-order correlation function has a dip, but does not go below 0.5, implying multiple emitters.

the nanodiamond may contain more than one color-center. The individual samples I measured from both sources (*Adamasnano* and *Quantum Particles*), were shown to have multiple color-centers. An AFM image of a single nanodiamond is shown in Figure 6.12. The nanodiamond samples have a very irregular shape and a wide distribution of sizes (mean size of 23 nm for *Quantum Particles* and 40 nm for *Adamasnano*). This irregularity makes it difficult to locate the emitter (color-center) within the nanodiamond. From our previous measurement (Section 5.4), the AFM tip will control the emitter polarization and direction only if the tip is within ~10 nm from the top and ~20 nm to the side of the QD. This condition is barely achieved using a nanodiamond for the currently available commercial sample.

There have been numerous efforts to synthesize single-digit nanocrystal (nanodiamond with a crystal size below 10 nm) with stable color-centers [122-125]. In addition, there has been a lot of research going on to improve the brightness of

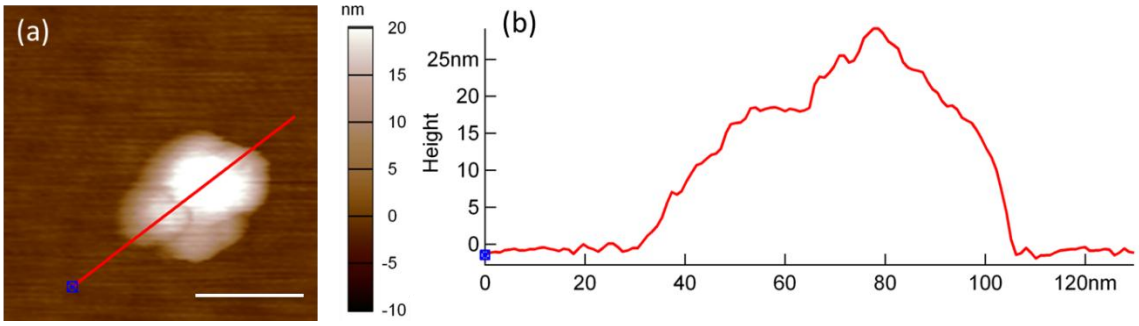

Figure 6.12 AFM image of a single nanodiamond. A carbon nanotube attached to the gold tip is used to scan the AFM image. (a) Topography of single nanodiamond. Scale bar is 50 micron. (b) Height profile along the red line in (a).

nanodiamond color-center [126]. With a chromium-related color-center in nanodiamonds, the emission rate is enhanced two orders of magnitude more than the highest reported emission rate for single-photon source for a nitrogen vacancy nanodiamond [127]. If we obtain the sample by either collaborating with a different group who makes such bright single photon sources or fabricating it ourselves down the road, we might achieve back-focal imaging as a function of tip-height.

6.7 Summary and Outlook

We developed a laser pulsing technique to modulate the laser to intermittently excite the fluorescent sample. Using the near-field interaction on the emission signal, the laser pulsing signal is synchronized with the tip-height. Experimental back-focal imaging is achieved and the tip-induced modification in the angular emission is experimentally verified.

Once we can overcome the experimental limitations by either reducing the noise or improving the signal from a single-photon source, we can study the modification emission pattern of single emitter placed next to a gold near-field probe.

CHAPTER 7

EMISSION PROPERTIES OF GALLIUM NITRIDE NANOWIRES

Most of the work on my dissertation has been related to investigation of the near-field interactions between QDs and the atomic force microscope tip to control the properties of QD emission. However, I have also been involved in several other projects in the lab. In this chapter, I will discuss investigations of the emission properties of gallium nitride (GaN) nanowires (NWs) with triangular cross-sections. Although at this point in time we have not applied any nano-optics methods to study these NWs, this is planned for the future and the work reported here is an important step toward that goal.

This project is a collaborative effort between the Molecular Foundry at Lawrence Berkeley National Lab (LBNL), the Gerton lab at Utah, and Mike Bartl's lab in the Department of Chemistry at Utah. The GaN NWs studied here are grown by Dr. Shaul Aloni at LBNL using metal-organic chemical-vapor deposition (MOCVD) [128]. Triangular cross-section GaN NWs (100-500 nm in diameter and up to tens of microns long) are grown on a sapphire wafer and provided to us. To date, I have been involved in acquisition of spectral data from these NWs, and have performed (and established and coded) appropriate algorithms for much of the analysis. I would like to thank Dr. Nicholas J. Borys for acquiring the photoluminescence emission spectroscopy and time-resolved spectroscopy data in Prof. John Lupton's lab at the Department of Physics and Astronomy, University of Utah, and Yuchen Yang, a graduate student in the Gerton lab

who is continuing this project for his PhD dissertation. Some of the data were taken using a WITec alpha-SNOM 300 S confocal microscope while the remaining were taken using a custom built hyper-spectral imaging system that I developed with some help from Yuchen Yang and Jason Martineau, a first-year graduate student in the Gerton lab.

In this chapter, the cavity modes and wave-guiding properties within the NWs are examined. In addition, photoluminescence excitation spectroscopy, time-resolved photoemission spectroscopy, and confocal hyperspectral imaging were used to reveal spatial, temporal, and spectral inhomogeneities arising from variations of the surface states on the nanowires.

7.1 Introduction

Semiconducting NWs have recently attracted increasing attention for their application in nanophotonics devices such as nanolasers [129], modulators [130], detectors [131], nanoscale white light sources [132], etc. In particular, GaN NWs have been investigated for some years due to their unusual absorption/emission properties [133-135]. In particular, while the bandgap for bulk GaN is in the UV (3.4 eV, ~365 nm), GaN nanowires efficiently absorb/emit light in the visible spectral range. There seems to be consensus in the community that this mid-gap optical response can be attributed to surface states and surface defects, which become more important when the material dimensions are nanometer-scale due to the increasing surface-to-volume ratio. Nevertheless, the origin and nature of these surface states/defects are not fully understood as a number of different types can be introduced during the growth process: point defects, dislocations, impurities, etc. [136].

Studying the visible photoluminescence spectrum of a NW as a function of

position on the NW gives some information on the density and nature of mid-gap surface states. When the spectrum is acquired from an ensemble of NWs or is averaged over one entire NW, much of this information is lost. To our understanding, we are the only group studying NWs of this sort at the sub-NW level, which allows us to reveal inhomogeneities that could be important for various applications including solar-driven photoelecrochemical water splitting. In this chapter, we use confocal measurements (focused excitation and collection from the same volume) combined with hyper-spectral imaging techniques to study inhomogeneity in the emission spectrum as a function of position on the NW. The spectrally and temporally resolved spectrum gives insight into the photoluminescence decay dynamics of the NW emission.

The luminescence from GaN NWs has a broad spectrum, which can cover the whole visible range. For such a broad spectrum, it can be difficult to characterize its shape, but this is desirable in order to map the spectral response at different locations on the wire. To overcome this difficulty, we introduce a quantity called the spectral center of mass (SCOM), which is expressed as:

$$\mathrm{SCOM} = \frac{\sum \lambda_m I_m}{\sum I_m} \tag{7.1}$$

where λ_m is the wavelength (in nm) and I_m the intensity corresponding to λ_m. The summation is performed for the whole measured spectrum at a single spatial location on the wire. SCOM has been shown as a robust way to measure a relative shift of a spectrum or a change in its shape [137] .

7.2 Results

7.2.1 Waveguide and Cavity Modes

In a typical confocal hyper-spectral measurement, a NW is excited at $\lambda = 488$ nm (well below the bulk bandgap energy, $\lambda \sim 365$ nm) with a laser beam and the emission from each spatial pixel is collected using the same microscope objective (100X, 1.4 NA) in a confocal microscope system (WITec Alpha-SNOM 300 S). In this excitation/detection scheme, the spatially resolved luminescence spectrum can be studied. The emission spectrum in each spatial pixel is summed over a certain wavelength range to make an intensity image of a NW, as shown in Figure 7.1a. The image exhibits intensity variations along the length of NW, which is clearly seen in the intensity profile curve along the center of nanowire. Interestingly, most of the nanowires we studied have brighter emission at the NW ends. The intensity enhancement at the end facets of the NW indicates strong waveguiding properties of both excitation and emission photons due to the significant index of refraction mismatch between GaN ($n \sim 2.4$) and air ($n = 1$) [132]. Also, the emission spectrum at the both ends of the NW shows a series of fringes over the entire spectrum, as shown in the black and red curves in Figure 7.1b. In contrast, the middle part of the NW shows very weak fringes with a different periodicity (blue spectrum in Figure 7.1b), which could be due to whispering gallery modes circulating azimuthally relative to the NW axis.

Previous studies have shown that the high-visibility fringes at the NW ends are caused by longitudinal Fabry-Perot modes that modulate the broad emission spectrum of a single NW [138-141]. Schwartzberg *et al.* (our collaborators for GaN nanowire sample growth) have studied the emission spectra from GaN NWs in detail [132], and have

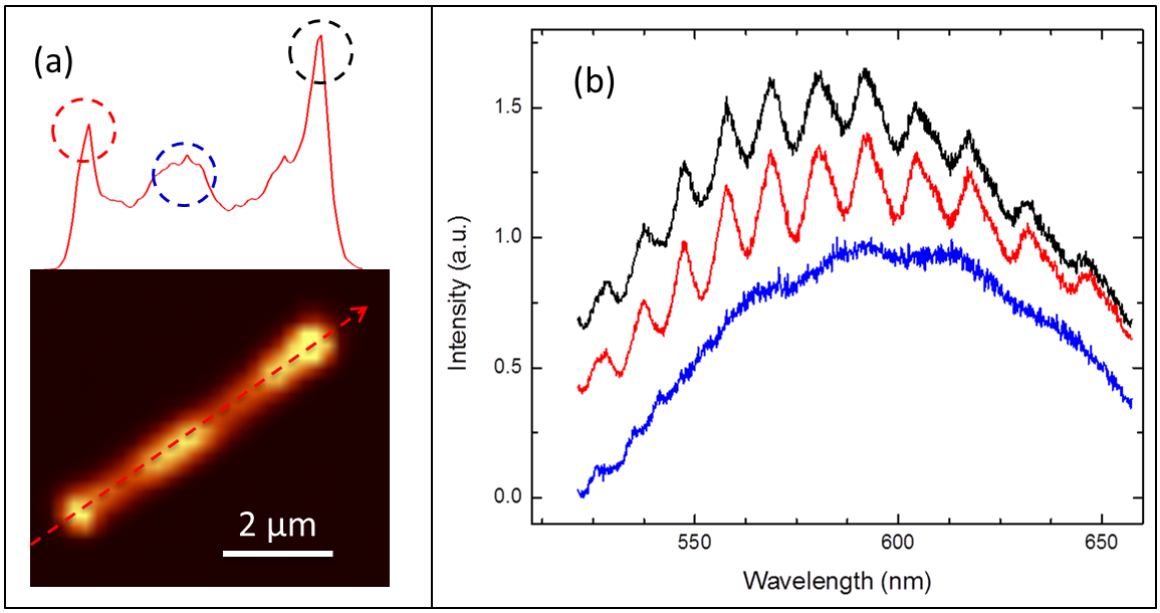

Figure 7.1 Cavity modes of a nanowire. (a) The intensity profile along the length of nanowire (along the red dotted line). (b) Waterfalls plot of the spectrum at the two ends (red and black curves) and at the middle (blue curve) of a nanowire. The dotted circles in (a) correspond the location of the image pixels chosen to be shown in (b). The red and black spectrums are normalized and shifted up by 0.4 and 0.65, respectively, for visual clarity.

shown that the fringes at both ends peak at the same wavelength, which is evidence of longitudinal cavity modes in the NWs. To study the cavity modes in detail, one has to study the mode spacing correlating to the length of the NW, which is not my current interest. By improving the quality factor of the cavity modes (Q-factor), there is a possibility of achieving lasing from a single NW. Due to existence of waveguide and cavity modes within a GaN NW, the absorption becomes enhanced. As a result, the emission is also enhanced. Moreover, the emitted photons can undergo multiple absorption and emission process, which complicates the absorption/emission process in GaN NWs.

7.2.2 Photoluminescence Excitation (PLE) Spectroscopy

In a typical PLE measurement, a NW is excited in wide-field mode (the whole NW is excited at once) using laser excitation that varies in wavelength between 380 and 480 nm with a 5 nm interval. The emission is collected with a 40X air objective, which can resolve spatial features on the wire of $\sim 1\ \mu m$ size. The photon-flux density is kept constant when the excitation wavelength is scanned. The collected emission is analyzed using a spectrometer/CCD system with a vertical entrance slit and emission spectrum will be spectrally resolved along the horizontal direction of the CCD imager. For a NW parallel to the vertical slit axis, the emission spectrum along the length of nanowire is spatially resolved along the NW length, as shown in Figure 7.2b. In this configuration, the vertically resolved emission spectrum of a NW can be studied as a function of the excitation wavelength.

Figure 7.2a shows NW imaged directly on the CCD (no spectral analysis) using pulsed excitation at a wavelength of 380 nm. Figure 7.2b and Figure 7.2c show the measured spectrum and normalized spectrum, respectively, of the same NW. The etalon fringes are clearly visible at the ends of the NW, as shown in Figure 7.2b and 7.2c. The emission intensity and spectral shape vary along the NW length, and the SCOM (black line in Figure 7.2c) demonstrates significant spectral inhomogeneity.

The black and blue lines in Figure 7.3a show the integrated intensity (sum of intensity along the horizontal pixels in Figure 7.2b) and the calculated SCOM (same as black line in Figure 7.2b) along the NW length. Comparing these curves, it is clear that there is a correlation between total intensity and SCOM. For a brighter region of NW, the spectrum is redshifted, which results in a SCOM value corresponding to longer

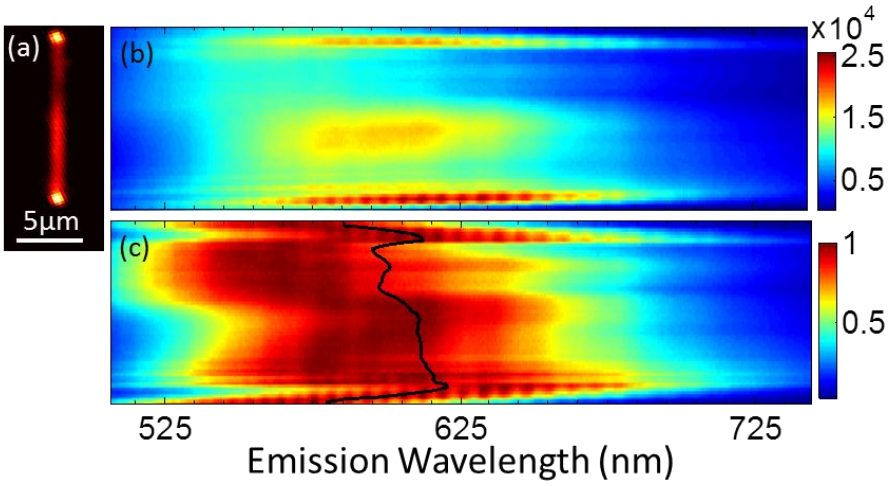

Figure 7.2 Emission spectrum of a nanowire. (a) A nanowire image observed on a CCD with 380 nm excitation and 500 nm long pass filter. (b) Emission spectrum image along the length of the nanowire, as shown in (a). (c) Each spectrum is normalized along the length of the nanowire. The black line in (c) represents the SCOM along the nanowire.

wavelengths. The integrated intensity and the calculated SCOM along the length of the NW as a function of excitation wavelength are shown in Figure 7.3b and 7.3c. The intensity and spectral shift remain consistently correlated for all excitation conditions.

Figure 7.4 shows the emission spectrum as a function of excitation wavelength for the whole nanowire. The colorscale in Figure 7.4a shows that the luminescence intensity decreases for longer excitation wavelengths. The normalized spectrum in Figure 7.4b also shows that the spectrum shifts as a function of the excitation wavelength. The black line in Figure 7.4b represents the calculated SCOM for each excitation wavelength averaged over the whole nanowire, revealing that the emission spectrum initially shifts toward red as the excitation wavelength is increased, and then shifts toward blue when the excitation wavelength is beyond ~440 nm. The normalized spectra shown in Figure 7.5, obtained for excitation wavelengths of 380, 440, and 480 nm, clearly demonstrate this spectral shift pattern. This pattern is consistent along the length of the NW as well, as shown by

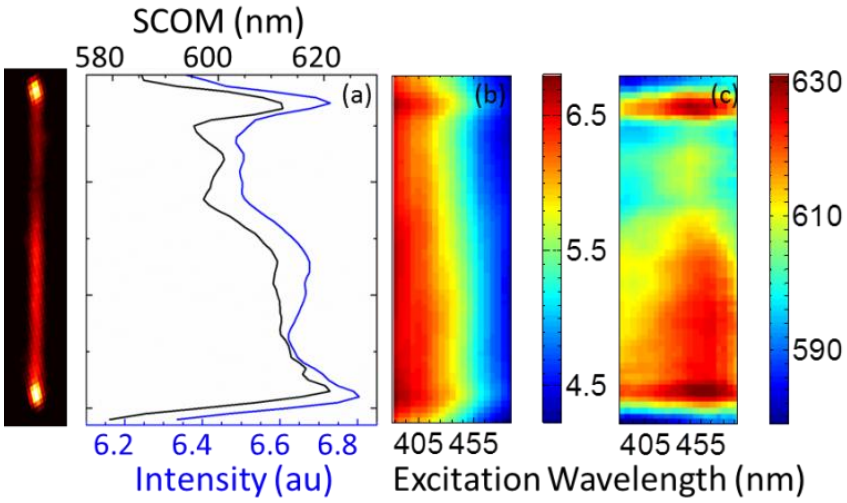

Figure 7.3 Intensity correlated with SCOM along the length of a nanowire. (a) The black and blue lines represent the calculated SCOM and the integrated intensity (log scale), respectively, along the nanowire length for 380 nm excitation wavelength. (b) The integrated intensity (log scale) image across the length of the wire as a function of excitation wavelength (380-480 nm in 5 nm step). (c) The calculated SCOM image as a function of excitation wavelength.

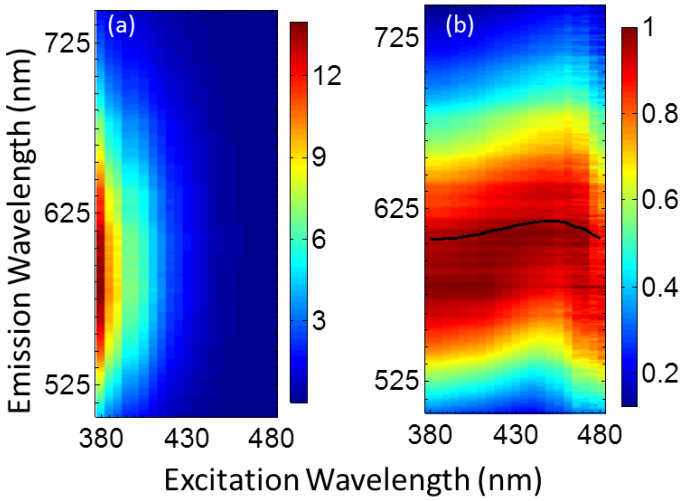

Figure 7.4 PLE spectroscopy. (a) The emission spectrum as a function of the excitation wavelength for the whole nanowire. (b) The emission spectrum is normalized for each excitation wavelength. The excitation wavelength is scanned between 380 nm and 480 nm in 5 nm steps. The excitation photon flux is kept constant for all excitation wavelengths. The black line in (b) represents the calculated SCOM plotted for each emission spectrum.

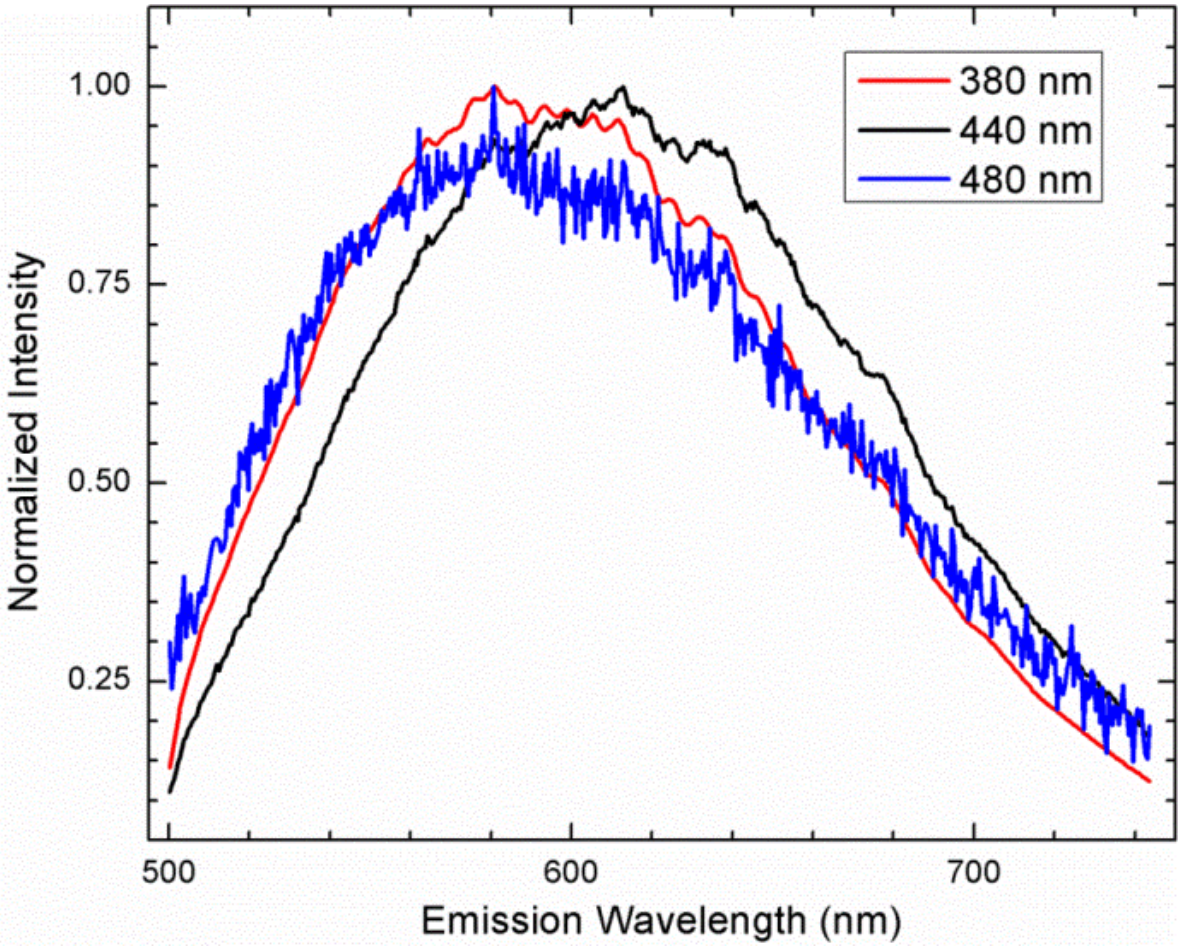

Figure 7.5 Normalized spectrum for the whole nanowire at the three excitation wavelengths. As excitation wavelength increases to 440 nm, the spectrum becomes redshifted. However, as excitation wavelength increases to 480 nm, the spectrum becomes blueshifted.

the SCOM image in Figure 7.3c: the emission from each spatial section of the NW shifts toward red up to ~440 nm excitation wavelength, and then shifts toward blue beyond that.

Figure 7.6 shows the total NW emission intensity captured on the spectrometer integrated over the length of the NW as a function of the excitation wavelength. Since the photon flux density in the excitation beam remains constant for each of the 21 different wavelengths, the variation in emission intensity reflects changes in the

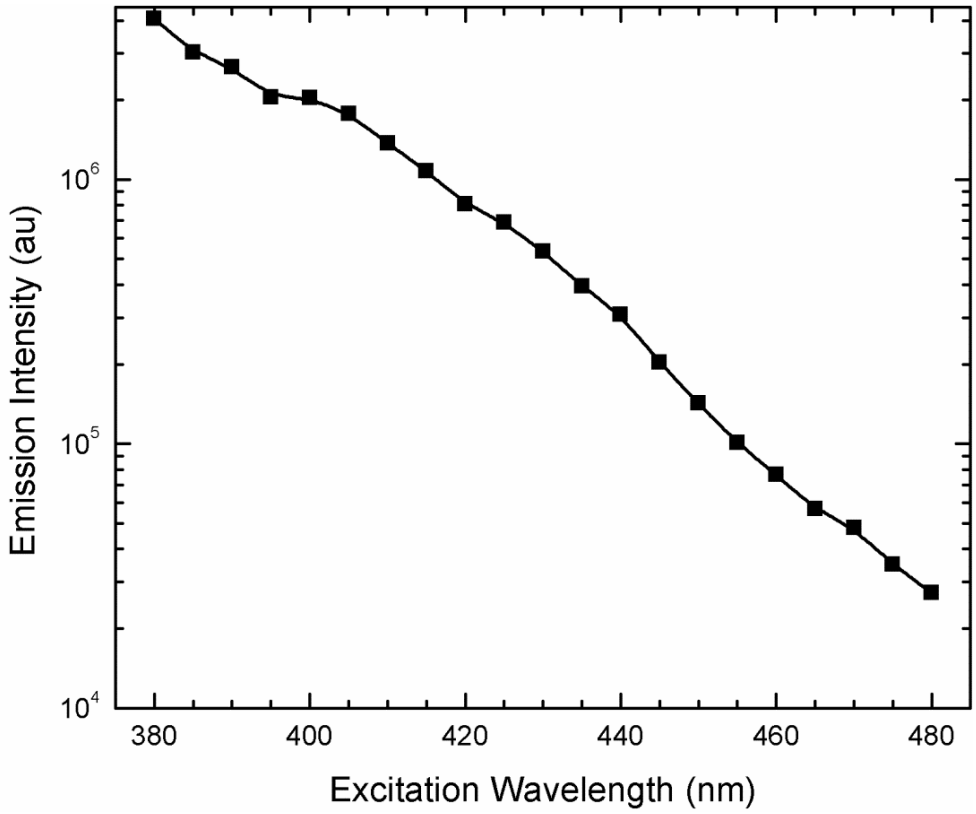

Figure 7.6 Photoluminescene emission spectroscopy of the whole nanowire. Emission intensity as the function of excitation wavelength at a constant photon flux density. The error bars are embedded within the symbol.

absorption efficiency and/or the fluorescence quantum yield. In general, the peak in the total intensity in the PLE measurement represents the absorption lines of the material. The material will have peak absorption at the bandgap. Since the bandgap of GaN is more towards the bluer wavelengths (~365 nm) than the excitation wavelength range we varied (380-480 nm), the luminescent intensity increases rapidly as the band edge is approached.

7.2.3 Spectral Inhomogeneity

As discussed above, the hyperspectral imaging technique enables us to study the spatially resolved emission spectrum within a diffraction-limited excitation volume.

Figure 7.7 shows an integrated luminescence intensity image for a NW when excited at 488 nm wavelength. The experimental setup is very similar as that described in Section 7.2.1. At each spatial pixel, the SCOM value is calculated, as shown in Figure 7.7b. The colorscale in the SCOM image reveals that the emission spectrum on one side of the NW is different than on the other. The red, yellow, cyan, and blue pixels across the dotted-line in Figure 7.7b is shown in the corresponding red, yellow, cyan, and blue curves in Figure 7.7c. The variation of calculated SCOM (wavelength shift ~30 nm) across two faces of the NW is reflected in the shift in the spectrum peak seen in Figure 7.7c. For the same batch of NW samples, there are variations in the spectral inhomogeneity from NW to NW, which is demonstrated from the SCOM image for different NWs, as shown in Figure 7.8.

7.2.4 Power Dependence of Spectral Inhomogeneity

To investigate how spectral inhomogeneity depends on the laser power, we interrogated single NWs while varying the excitation power over three orders of magnitude. A calculated SCOM image for a particular NW for different excitation powers is shown in Figure 7.9. The excitation power density ratios for the images are 1:10:63:100:253:432 from (a)-(f) in Figure 7.8, demonstrating that the spectrum shifts toward blue as the excitation power increases. One possible reason for the blueshift with increasing excitation power is saturation of surface defect states mentioned above. As the exciton generation rate overshoots the recombination rate, the excited electrons pile up to a higher energy state in the density of states, opening a wider quasi-bandgap [142]. As a result, the luminescent spectrum becomes blueshifted with increasing excitation power.

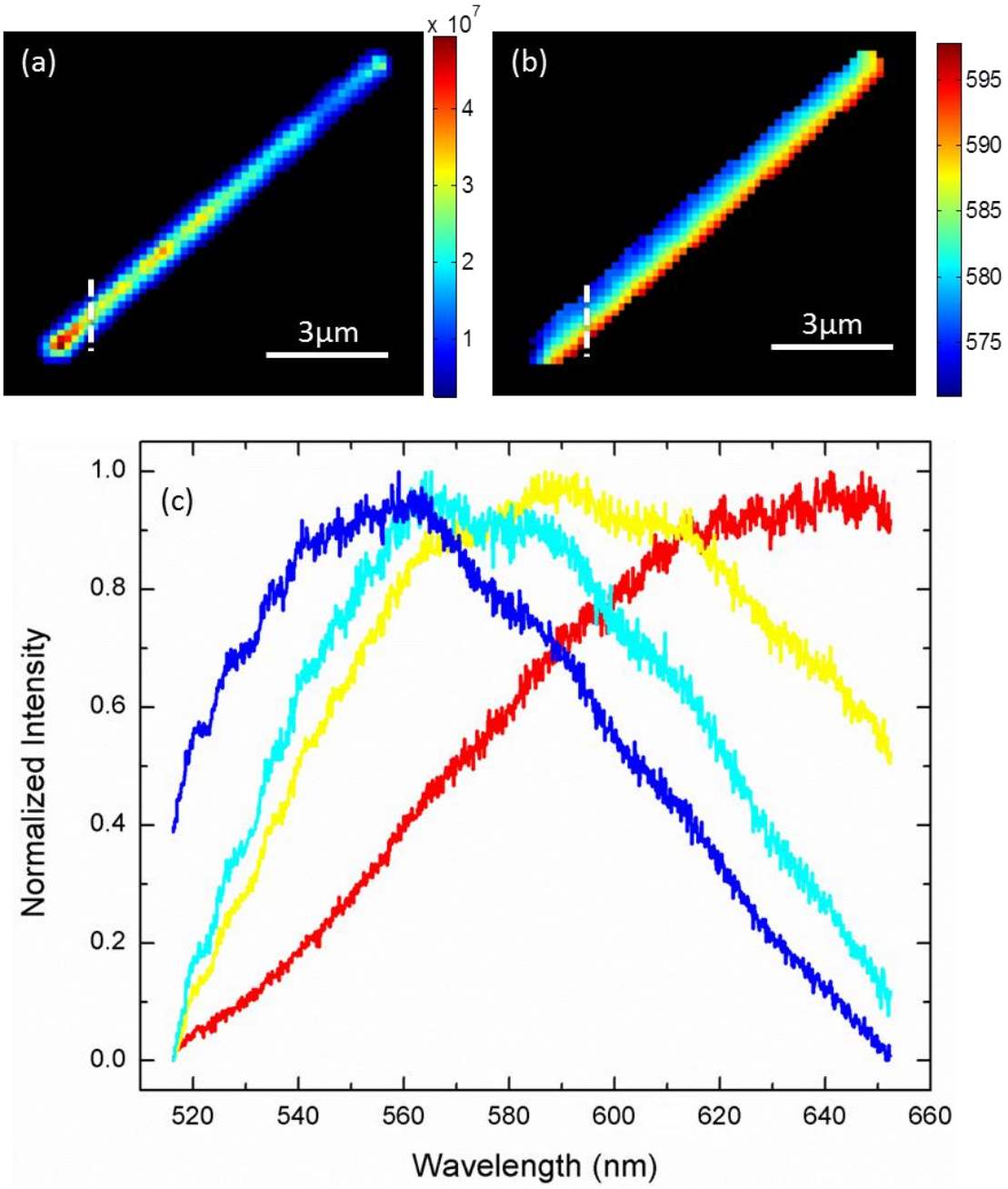

Figure 7.7 Spectrum inhomogeneity within a nanowire. (a) Integrated intensity image for a nanowire. (b) Calculated SCOM on each pixel spectrum. (c) Normalized spectrum of blue, cyan, yellow, and red pixels along the dashed line in (a) and (b), showing examples of spectrum variation in different colored SCOM pixels in (b).

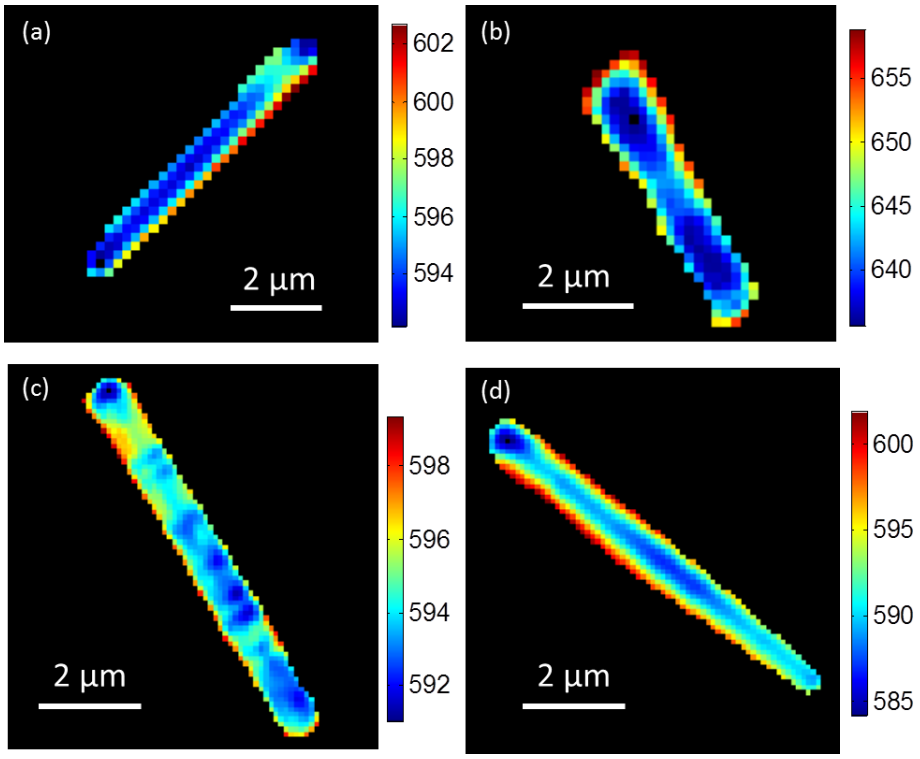

Figure 7.8 SCOM images showing variations of spectrum inhomogeneity among different nanowires.

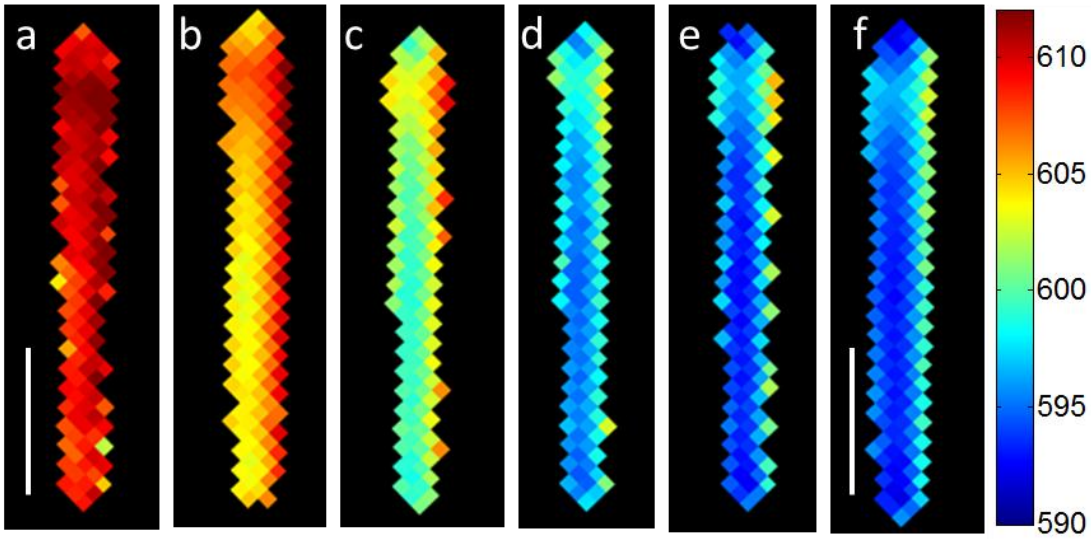

Figure 7.9 Excitation power-dependent SCOM image for a nanowire. The power density from (a)-(f) has a scaling ratio of 1:10:63:100:253:432. The lowest power density corresponding to f is 1.2532×10^{8} watt/m^{2}. The white scale bar in (a) and (f) is 2 µm.

7.2.5 Time-Resolved Emission Spectroscopy (TRES)

TRES measures the excited state decay dynamics of photogenerated carriers. In this measurement, a NW is excited with a pulsed laser (140 fs pulse width) at 350 nm wavelength. The emission is spectrally separated using a grating monochrometer followed by a streak camera to temporally resolve the different spectral components. Figure 7.10 shows both spectrally and temporally resolved emission spectrum in the horizontal and vertical directions, respectively. The colorscale represents the intensity of the spectrum. Figure 7.10b is the same NW as Figure 7.10a, but with each spectrum normalized in the horizontal direction (for constant decay time). The black line in Figure 7.10b represents the calculated SCOM as a function of the decay time. The normalized TRES (Figure 7.10b) demonstrates that the emission becomes redshifted as the decay time increases. This redshift is verified from the calculated SCOM as a function of decay time, as shown in Figure 7.11.

Figure 7.12 shows the decay curve for the integrated spectrum. The luminescence intensity decays rapidly as a function of decay time. The intensity data can be fit with a stretch exponential function:

$$I = I_0 \exp(-(t/\tau)^{\beta}) \qquad (7.2)$$

where t is the decay time, τ is the decay constant, and the coefficient β is called the dispersive kinetics coefficient. The value of this coefficient is $0 \leq \beta \leq 1$. In the limiting case when $\beta = 1$, the stretch exponential function becomes a normal exponential function with the characteristic lifetime τ. For $\beta < 1$, the emission process can be expressed as the superposition of many exponential decays [143]. The fitted values for the decay constant

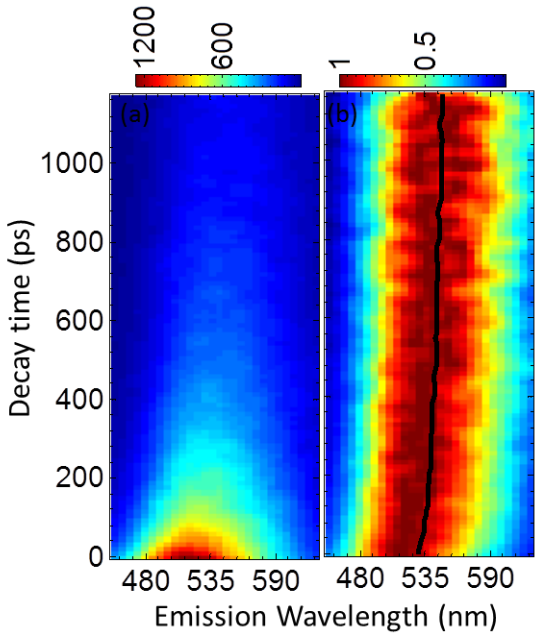

Figure 7.10 Time-resolved emission spectroscopy. (a) Intensity decay over time after a pulse excitation for various emission wavelengths. (b) Spectrum is normalized for each time bin. The black continuous line represents the SCOM for each spectrum along the decay time. The normalized spectrum together with calculated SCOM (black line) shows the spectrum shifts towards longer wavelength.

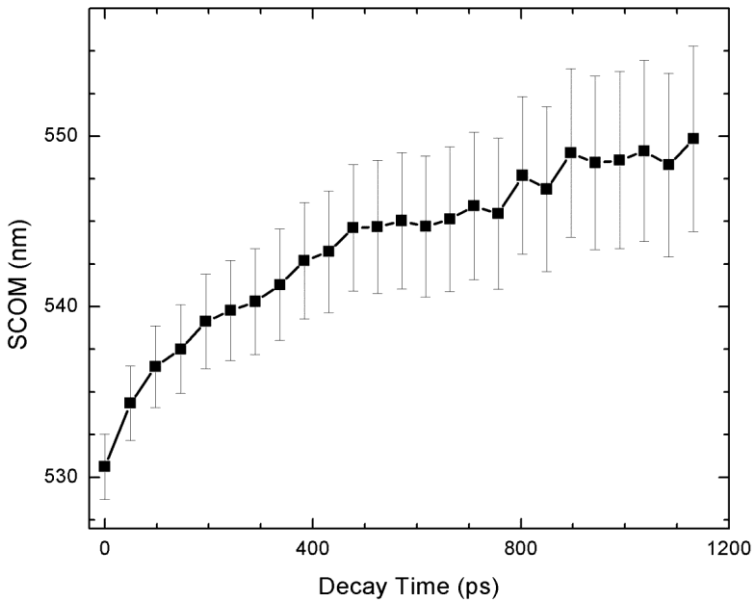

Figure 7.11 Calculated SCOM versus decay time. The calculated SCOM shows the redshift of spectrum with the decay time. The error bars are calculated from the data.

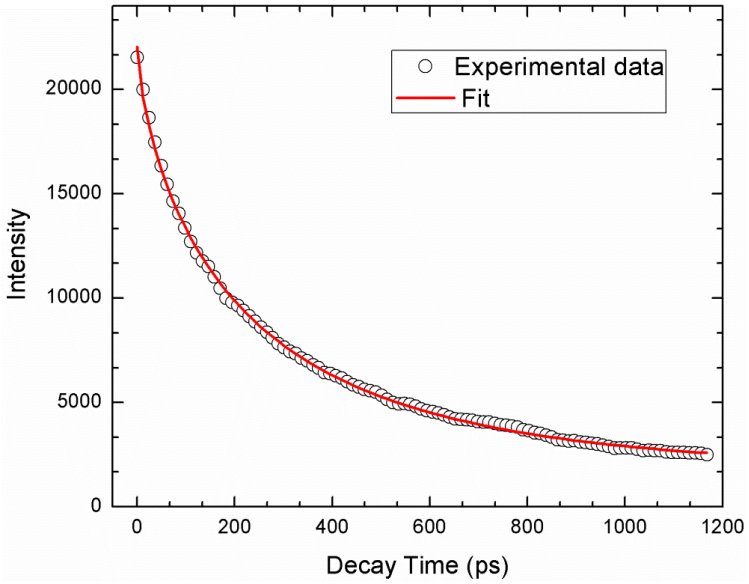

Figure 7.12 Intensity decay curve for the total spectrum with a pulse excitation. The open symbol represents the measured data and red line represents the fit. The decay is fitted using stretch-exponential function with decay constant (τ) = 227 ps and coefficient (β) = 0.705.

(τ) and the coefficient (β) are 227 ps and 0.705, respectively, for the data shown in Figure 7.12. The same stretch exponential function can be used to analyze the spectrally-resolved emission data shown in Figure 7.10. The decay constants (τ) extracted from the fit are shown in Figure 7.13. The decay constant (τ) increases as the emission wavelength increases, indicating that the blue spectral components decay faster than the red components. Within the spectral range studied, the decay constant varies from 100 to 350 ps. The value of β extracted from the fits is broadly distributed, as shown by the histogram (Figure 7.14). More interestingly, the value of beta in this distribution remains less than unity, indicating that the emission process consists of a distribution of decay constants even within the narrow emission spectrum-band.

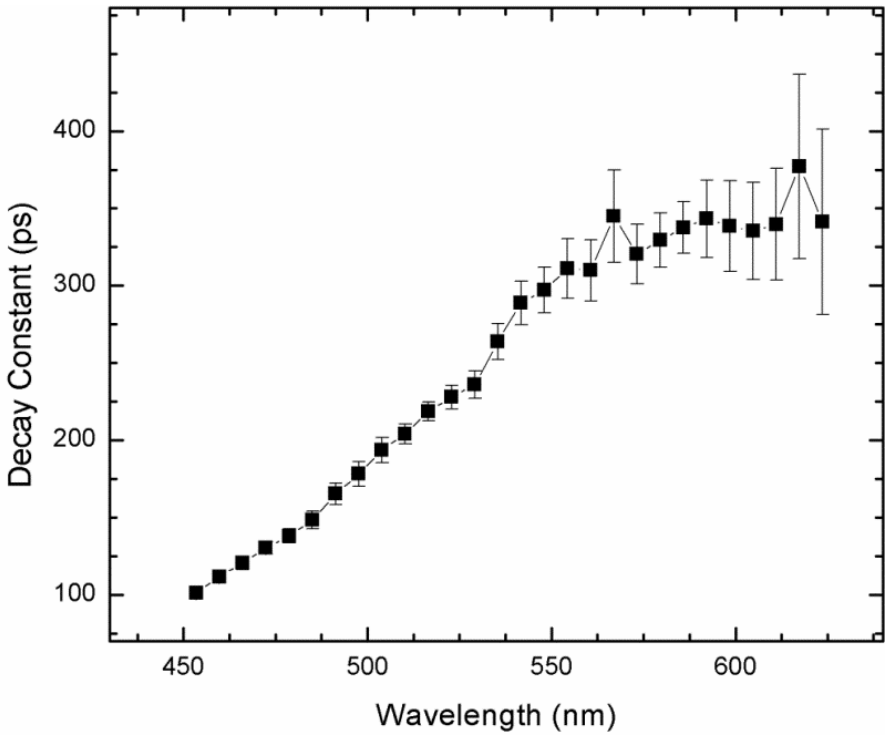

Figure 7.13 Decay constant (τ) for different emission wavelengths extracted from the fit. Each decay curve is binned in 6 nm spectrum-band. The decay curve is fitted with the stretch exponential function and decay constants are extracted from the fit. The error bars are taken from the fit.

7.1 Discussion

The photoluminescence from a GaN nanowire shows a broadband emission spectrum. The origin of such a broad spectrum is due to the presence of the myriad of optical transitions associated with mid-gap defect states [136]. For the generation of such broadband emission spectra from a single nanowire, multistate emission processes are required, as schematically shown in Figure 7.15. Due to the presence of such a high density of mid-gap defects states, GaN nanowires have been shown to have high two/multiphoton absorption cross-sections. These cross-sections enable the band-edge excitation of the wide-bandgap (3.4 eV) semiconductor using visible light. The waveguide and cavity modes within the nanowire confine both excitation and emission

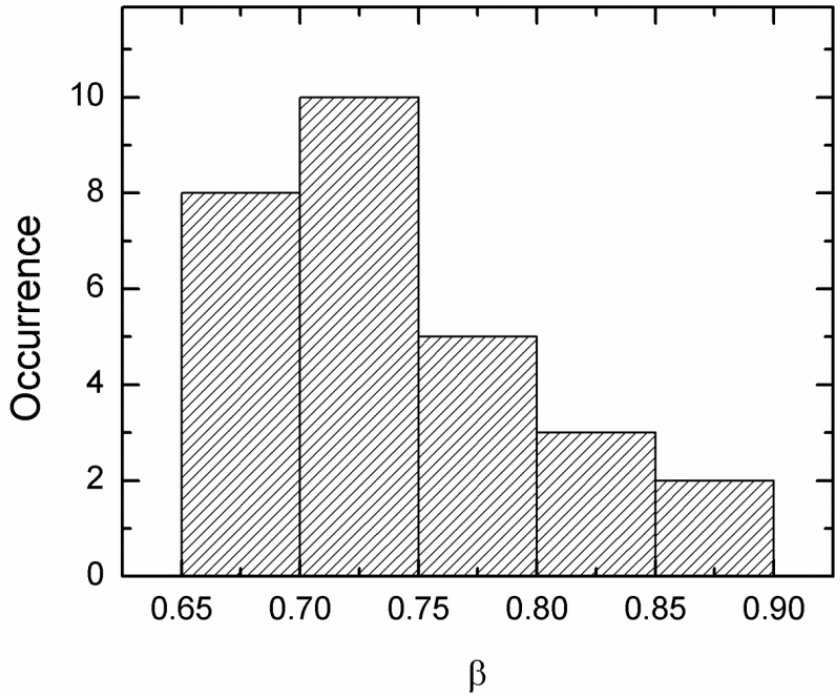

Figure 7.14 Histogram showing the distribution of the coefficient β extracted from the fit.

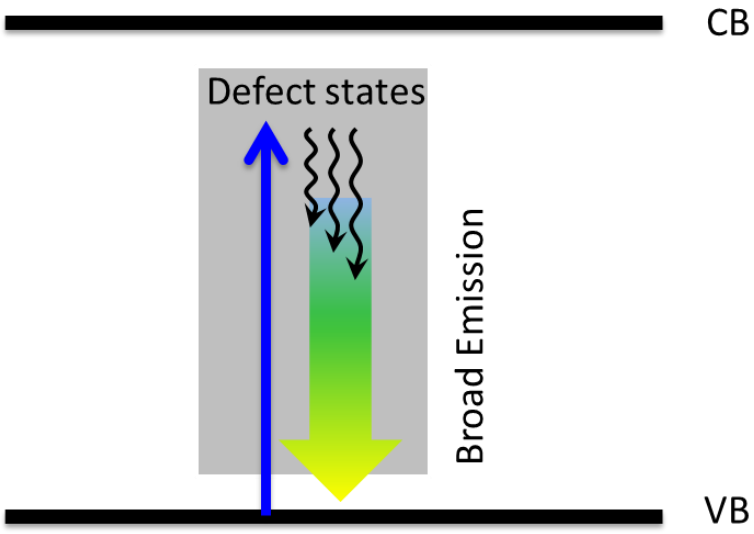

Figure 7.15 Idealized schematic diagram of broadband emission via absorption of blue laser (represented by blue arrow) followed by nonradiative decay (represented by black arrows) to energetically broad mid-gap states (represented by large arrow).

within a nanowire, enhancing the multiphoton absorption process. The same emitted photon can undergo a cascaded absorption and reemission process within a nanowire, yielding a broad emission across a visible range.

The calculated SCOM in PLE spectroscopy reveals a spectral inhomogeneity along the length of the nanowires (Figure 7.2c). In general, brighter end regions exhibit a redshifted spectrum. One plausible explanation for redshift is stated as follows. Cavity modes act as a resonator, and in general, brighter parts of the nanowire correspond to the ultimate/final mode leakage region for that resonator. The cascaded absorption and reemission process happens for a longer time within the nanowire. This cascaded absorption and emission process will shift the emission spectrum towards lower energy states, i.e., towards longer wavelengths, which is ultimately detected in the brighter region of the nanowire. Also, TRES supports this explanation as the spectrum is redshifted at longer decay times (Figure 7.11).

The calculated SCOM in PLE measurements (Figure 7.4b) shows that the spectrum is shifted toward red as the excitation wavelength increases from 380 to 440 nm and shifted toward blue from 440 to 480 nm. There is not an obvious clue to explain this spectral shift in our result. One would expect some indication in the luminescence intensity variation at ~440 nm excitation wavelength (the integrated intensity versus excitation wavelength curve in Figure 7.6). One possible explanation for this blueshift in spectrum may be due to increase in two-photon absorption cross-section at longer than 440 nm excitation wavelength. The luminescent spectrum has minimum intensity at ~440 nm, (in Figure 3 [132]) for a similar GaN nanowire, indicating lower density of mid-gap states corresponding to that energy band. As the density of mid-gap states

increases beyond excitation energy corresponding to wavelength ~440 nm, it is more likely to have efficient two-photon absorption. The integrated luminescence intensity at higher energies than excitation energy needs to be studied to verify if this is the case.

More importantly, the spatially resolved luminescence spectrum analysis reveals that a nanowire has spectral variations at different regions of a nanowire, which is depicted by the calculated SCOM (Figure 7.7 and Figure 7.8). These variations in the emission spectrum demonstrate that the density of mid-gap defect states is also varying at different regions of a nanowire. The broadband luminescent spectrum is proof of highly continuous mid-gap defect states present on a single nanowire. However, these continuous states have local variations in different energy states producing spectral inhomogeneity (Figure 7.7 and Figure 7.8) locally within a nanowire.

A GaN nanowire contains many structural and point defects caused to a large extent by lattice and stacking mismatch with substrates during the growth process [136]. The distribution of defects may not be uniform and are expected to be at the corners of the triangular cross-section. Besides surface defects, metallic nanoparticles (Ni or Au) are embedded inevitably within the nanowire, which are used as a precursor during the growth process [144]. Physical conditions such as temperature gradient, growth time, precursor density/size, sample flow rate, etc. will control the growth direction and diameter of the nanowire, which results in various crystallographic terminations on the exposed surfaces. Even in the highly pure/clean MOVCD growth process, impurities such as carbon, hydrogen, etc. are expected to unintentionally introduce defects [136]. The presence of such defects might contribute to spatial-spectral inhomogeneity. Full spectrum analysis for so-called blue-, green- and yellow-band mid-gap states might reveal

the contributing factors for such local variation in density of defect states [136, 145].

By measuring the luminescence intensity using pulse excitation at different wavelengths as a function of decay time reveals some valuable information about the recombination mechanism. The redshift in the emission spectrum as a function of decay time (Figure 7.10 and 7.11) indicates that the higher energetic states (blue spectrum) decay faster than lower energetic states (red spectrum). The luminescence decay is nonexponential and instead fits well with the stretch-exponential. The coefficient $\beta < 1$ in the fit indicates that the luminescence in GaN nanowire can be considered as the superposition of many emitter systems having different decay rates. Spectrally-resolved decay processes follow the same decay dynamics ($\beta < 1$) as the integrated spectrum, indicating that the mid-gap defect states have a similar energy gap but a different decay rate constant. The luminescence in a GaN nanowire has multistate emission processes with spatial variations in mid-gap defect states, making the decay dynamics act like a disordered system [146].

7.2 Conclusion and Outlook

In conclusion, we have seen that a GaN nanowire has broadband luminesce covering nearly the entire visible spectrum. This broad luminescence in GaN is coming from the optical transitions of highly dense mid-gap defect states. Hyper-spectral imaging techniques enable us to study the spatial variation of these mid-gap states, resulting in spectral inhomogeneity within the nanowire. The luminescent decay dynamic illustrates that the high energy states are less stable, resulting in a redshift in emission spectrum as a function of decay time. The intensity decay follows the stretch-exponential law, indicating the luminesce decay in GaN nanowires consists of multiple emission

processes.

To understand more about these mid-gap defect states on GaN nanowires, one could perform hyper-spectral imaging combined with high resolution atomic force microscopy or scanning electron microscopy. To see if there are defects associated with impurities (C, H), energy dispersive X-ray spectroscopy could be performed for elemental analysis. Excitation power-dependent photoluminescence experiments combined with some theoretical modeling might also help to study the density of mid-gap states since our excitation power-dependent measurements show that as the power goes up, these mid-gap states gradually fill up. Photoluminescence spectroscopy combined with other measurement techniques is required to unravel the mystery of these localized mid-gap defect states in GaN nanowires.

APPENDIX A

SIZE EFFECTS, MIE THEORY

In the limit of very small particles, much smaller than the wavelength of light, the dipole approximation (Raleigh theory) is sufficient to explain the scattering of electromagnetic waves from such particles. The finiteness of the speed of light limits the dipole approximation with increasing particle size. When the particle size is larger than the *penetration depth*, the electromagnetic field is expelled from inside the metal, which will change the optical response of large metal particles. More importantly, for a sphere of diameter $2R$ comparable to the wavelength, retardation effects play a significant role in scattering. In particular, for opposite charges separated diametrically, two ends of a particle have a relative phase delay on the order of $4\pi R/\lambda_m$. Consequently, higher order near-field modes (quadrupole, hexapole, etc) are induced on the surface of the particle. The near-field intensity distribution for a gold sphere of different radii $R = 50, 100, 150, 200$ nm) is shown in Figure A.1.

The optical response of a spherical particle is theoretically predicted from analytical solutions of Maxwell's equations. Gustave Mie first found the size-independent solution for a spherical particle in 1908 [42]. The total cross-section of a spherical particle is:

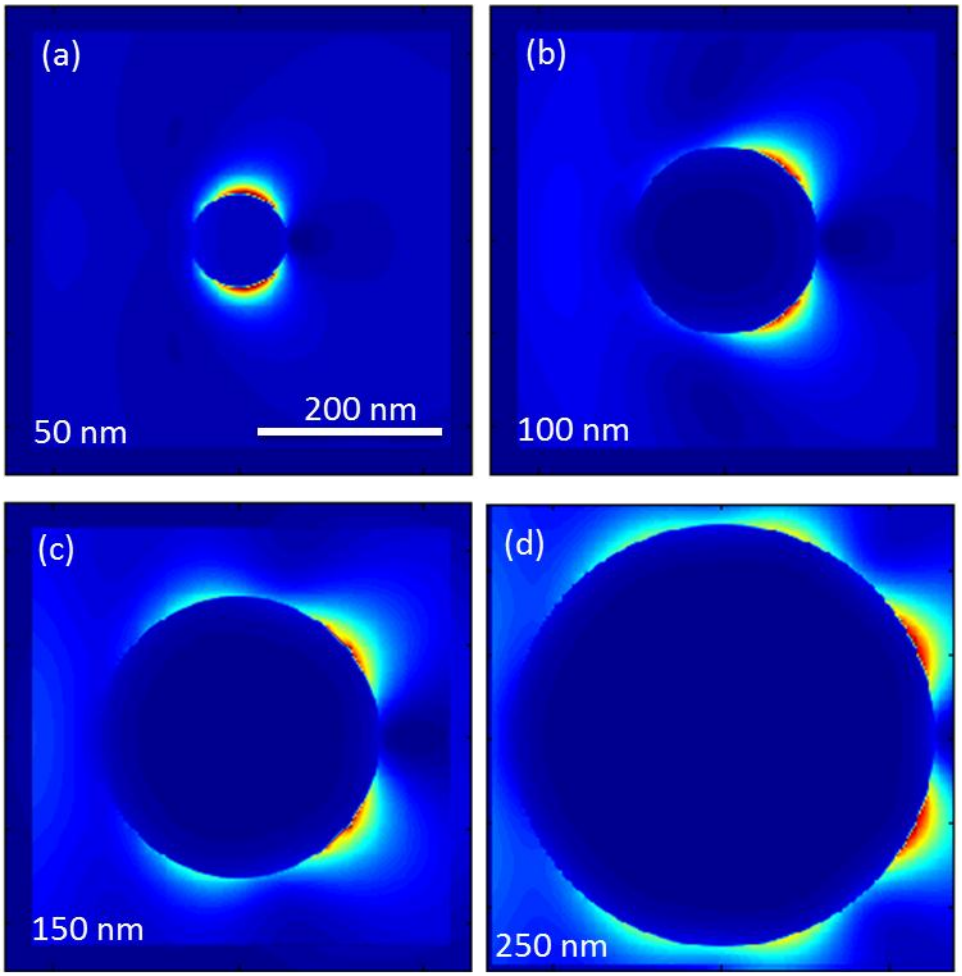

Figure A.1 Near–field intensity of spherical gold particles for different sizes. FDTD simulation: a plane wave is propagating left to right and the polarization axis is in the vertical direction. The wavelength of light is 524 nm using a dielectric constant from ref. [40]. (a), (b), (c), and (d) shows near-field intensity pattern for gold sphere of radius $R = 50,100,150,$ and 250 nm, respectively. The maximum intensity ratio for each figure is a:b:c:d ≈ 21:15:11:7.5. (a) 50 nm sphere mainly has dipolar mode ($l = 1$). (b), and (c) have quadrupole mode ($l = 2$), distinctly with 150 nm radius. (d) has six lobes with hexapoles ($l = 3$) for 250 nm radius.

$$\sigma = \frac{\lambda_m^2}{2\pi}\sum_{l=1}^{\infty}(2l+1)[\Im\{t_l^E\} + \Im\{t_l^M\}] \quad \text{(A.1)}$$

where l = 1, 2… correspond to dipole, quadrupole, etc. moments and t_l^E and t_l^M are the electric and magnetic scattering coefficients, respectively. These coefficients are related to the spherical Bessel (j_l) and Hankel (h_l) functions as:

$$t_l^E = \frac{-\epsilon_m j_l(\rho_m)[j_l(\rho) + \rho j_l'(\rho)] + \epsilon[j_l(\rho_m) + \rho_m j_l'(\rho_m)]j_l(\rho)}{\epsilon_m h_l^{(+)}(\rho_m)[j_l(\rho) + \rho j_l'(\rho)] - \epsilon\left[h_l^{(+)}(\rho_m) + \rho_m h_l^{(+)\prime}(\rho_m)\right]j_l(\rho)} \quad \text{(A.2)}$$

$$t_l^M = \frac{-\rho j_l(\rho_m) j_l'(\rho) + \rho_m j_l'(\rho) j_l(\rho)}{\rho h_l^{(+)}(\rho_m) j_l'(\rho) - \rho_m h_l^{(+)\prime}(\rho_m) j_{l(\rho)}} \quad \text{(A.3)}$$

where $\rho = (2\pi R/\lambda)\sqrt{\epsilon}$ (particle), $\rho_m = (2\pi R/\lambda)\sqrt{\epsilon_m}$ (medium), and prime represent the derivatives [47].

These equations allow cross-section calculations in a relatively straightforward way using simple computer programming. In fact, there are a large number of free programs available to calculate scattering from spherical particles using Mie theory [147].

APPENDIX B

DETECTED SIGNAL DUE TO INTERACTING FIELD

For a point dipole located at $\mathbf{r}_0(x_0, y_0 z_0)$ in the homogeneous, isotropic, and linear medium, the electric field at point $\mathbf{r}(x, y, z)$ due to this radiating dipole is given by [1]:

$$\mathbf{E}(\mathbf{r}, \omega) = \mu_r \mu_0 \omega^2 \, \vec{\mathbf{G}}(\mathbf{r}, \mathbf{r}_0, \omega)\mathbf{q} \tag{B.1}$$

where μ_r is the relative permeability, μ_0 is the permeability of vacuum, $\vec{\mathbf{G}}(\mathbf{r}, \mathbf{r}_0, \omega)$ is outgoing infinite-space of the dyadic Green function and $\mathbf{q}$ is the dipole moment. When a sharp gold tip is within the field of the dipole (Equation B.1), the tip will be polarized due to the dipole field and the induced dipole moment of a polarized tip is given by the relation [148]:

$$\mathbf{q}_{\text{tip}} = \alpha \, \mathbf{E}(\boldsymbol{r}, \omega) \tag{B.2}$$

where α is the polarizability tensor as discussed in Chapter 2 (Section 2.9) and E(r,ω) is the electric field of the emitting dipole. Equation B.2 is the expression for induced dipole when the dipole and tip are in homogeneous, isotropic media. If the dipole is situated near the air/glass interface and the gold tip is in air medium near the dipole, the effective dipole moment of induced dipole of the tip will be changed significantly. To calculate the effective dipole moment of the tip, we have to first calculate the total electric field that

polarize the tip.

Figure B.1 shows the schematic picture of the interaction of different fields (dipole field, field scattered from tip, and field reflected on the interface). In fact, the emitting dipole also gets polarized due to its own field scattered from the tip and reflected field through the interface (blue arrow in Figure B.1). Due to this polarization, the effective dipole moment of the emitting dipole may be also modified. However, let us focus only on the effective dipole on the tip. The total field on the tip is mainly composed of three different fields (indicated by green arrows in Figure B.1): direct emission field from dipole, reflected (dipole field and field of induced dipole within tip) from interface. If the tip is very close to the dipole and interface, the contribution to the total field from the scattered field is significant. Mathematically, the effective dipole inside the tip is written as:

$$\mathbf{q_t} = \alpha\ \mu_r\mu_0\omega^2\ [\overleftrightarrow{\mathbf{G}}(\mathbf{r},\mathbf{r}_0,\omega)\mathbf{q} + \overleftrightarrow{\mathbf{G}}_r(\mathbf{r},\mathbf{r}_0,\omega)\mathbf{q} + \overleftrightarrow{\mathbf{G}}_{rt}(\mathbf{r},\mathbf{r}_0,\omega)\mathbf{q_t}] \tag{B.3}$$

where $\overleftrightarrow{\mathbf{G}}(\mathbf{r},\mathbf{r}_0,\omega)$, $\overleftrightarrow{\mathbf{G}}_r(\mathbf{r},\mathbf{r}_0,\omega)$ and $\overleftrightarrow{\mathbf{G}}_{rt}(\mathbf{r},\mathbf{r}_0,\omega)$ are the free-space Green tensor for the source dipole (green path 1 in Figure B.1), reflection Green tensor on the interface for the source dipole (green path 2 in Figure B.1) and reflection Green tensor for the tip dipole itself (green path 3 in Figure B.1). In the above Equation B.3, the change in radiative reaction of dipole emitter is neglected, which will change the total decay rate of dipole emission.

Now the field in the detection plane can be written as linear superposition of the field due to each effective dipole as:

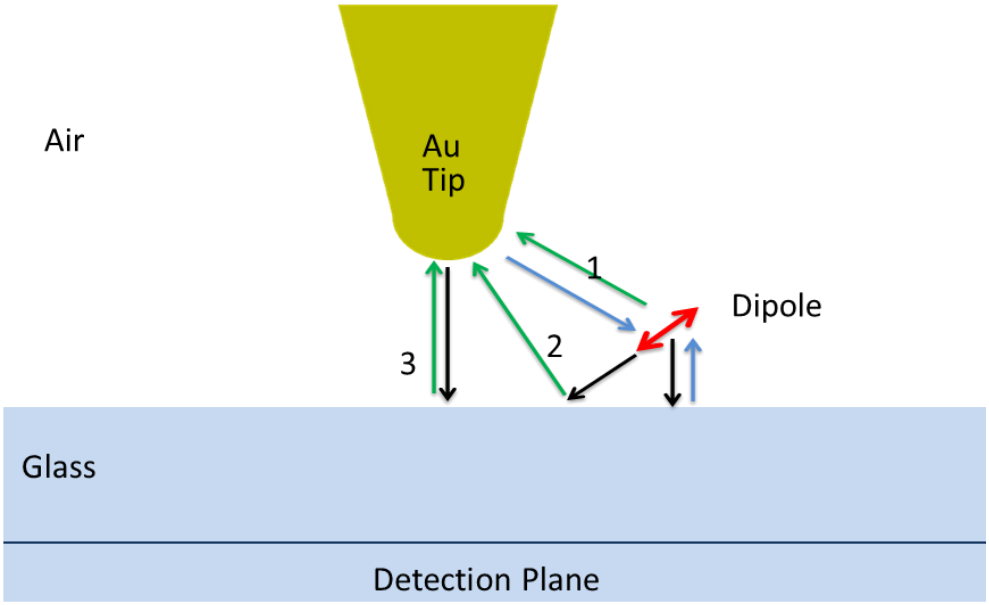

Figure B.1. Schematic picture of interaction of dipolar field between dipole and gold tip near air-glass interface. A dipole emitter is situated near air-glass interface. The gold tip is close to dipole and interact with near-field of dipole emitter. The scattered and reflected field from tip and interface interact with dipole itself represented by blue arrow. The tip is polarized by different fields: direct field of dipole, field reflected at interface, self-field of tip reflected at interface (represented by green arrows). Here, we neglect the multiple-reflection as well as the scattering from sample (dipole).

$$\mathbf{E_d}(\mathbf{r},\omega) = \mu_r \mu_0 \omega^2 \vec{\mathbf{G}}_t(\mathbf{r},\mathbf{r}_0,\omega)\mathbf{q}_{\text{eff}} \tag{B.4}$$

where $\vec{\mathbf{G}}_t(\mathbf{r},\mathbf{r}_0,\omega)$ is the transmitted Green's function in the glass medium and $\mathbf{q}_{\text{eff}}$ is each effective dipole. Hence, the total field in the imaging plane is the superposition of the emitting dipole field and the effective tip dipole field:

$$\mathbf{E}_{\text{im}}(\mathbf{r},\omega) = \mathbf{E}_{\text{q}}(\mathbf{r},\omega) + \mathbf{E}_{\text{qt}}(\mathbf{r},\omega) \tag{B.5}$$

The intensity pattern in the imaging plane (far-field) is related to the field as:

$$I_{im}(r,\omega) = |\mathbf{E}_{im}(\mathbf{r},\omega)|^2 \qquad \text{(B.6)}$$

The interference due to superposition of the effective dipolar field will determine the emission pattern in the far-field. The theoretical treatment described above is an analytical approach to simplify the scattering problem reduced to effective dipole moments in terms of Green's function.

APPENDIX C

EVANESCENT FIELD

Evanescent fields play a fundamental role in near-field optics. These fields are nonpropagating but decaying exponentially within the subwavelength dimension in space. Due to the nature of the evanescent field, it cannot be created in the homogenous medium. The simple realization of the evanescent field is understood by identifying the total internal reflection condition.

To illustrate the creation of the evanescent field using the total internal reflection condition, let us start with the configuration shown in Figure C.1a. A plane wave (both s- and p-polarized wave) is incident on the interface of two mediums defined by the optical constants ϵ_1, μ_1 and ϵ_2, μ_2, respectively. The amplitude of the reflected and refracted beam is given by Fresnel coefficients [1]. The transmitted amplitude can be expressed in terms of incident amplitude as:

$$\begin{bmatrix} E_{2x} \\ E_{2y} \\ E_{2z} \end{bmatrix} = \begin{bmatrix} -\mathrm{E}_1^{(\mathrm{p})}\mathrm{t}^{\mathrm{p}}(k_x)k_{z2}/k_2 \\ \mathrm{E}_1^{(\mathrm{s})}\mathrm{t}^{\mathrm{s}}(k_x) \\ \mathrm{E}_1^{(\mathrm{p})}\mathrm{t}^{\mathrm{p}}(k_x)k_x/k_2 \end{bmatrix} e^{ik_x x + ik_{z2} z} \qquad \text{(C.1)}$$

The wave vectors can be expressed in terms of the angle of incidence as:

$$k_x = k_1 \sin\theta_1, \quad k_{z_1} = k_1\sqrt{1-\sin^2\theta_1}, \quad k_{z_2} = k_2\sqrt{1-\eta^2\sin^2\theta_1} \qquad \text{(C.2)}$$

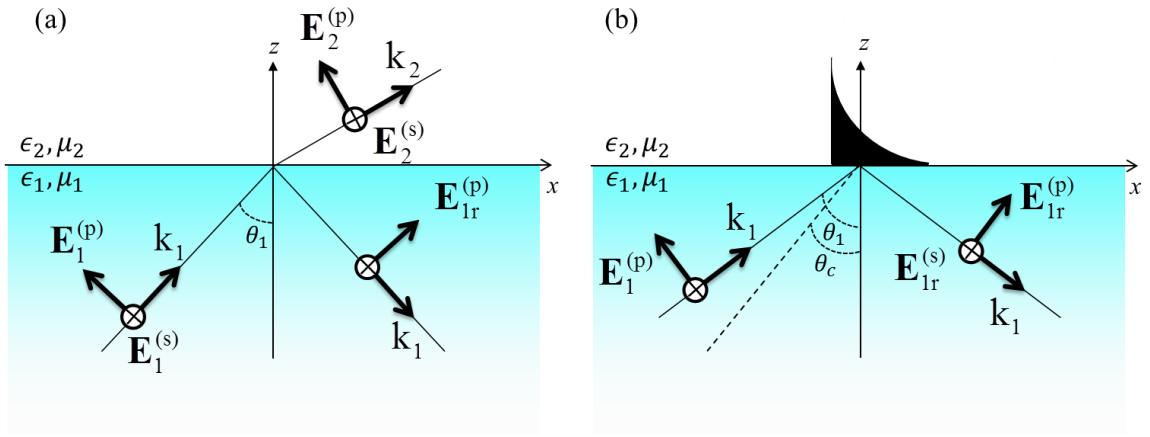

Figure C.1 Reflection and refraction of a plane wave (both s- and p-polarized) at an interface of two mediums. (a) For the angle of incidence $\theta_1 < \theta_c$, a reflection and refracted beam is created. (b) For the angle of incidence $\theta_1 \geq \theta_c$, the incident beam is totally internally reflected back into the same medium, creating an evanescent wave in the other medium. In the case of total internal reflection, the field is exponentially damped above the interface. Hence, there is no net energy transmitted in that direction.

where η is the relative refractive index of two mediums defined as $\eta = \sqrt{(\epsilon_1\mu_1)/(\epsilon_2\mu_2)}$. For $\eta > 1$, with an increased angle of incidence (θ_1), the wave vector k_{z_2} becomes imaginary above a certain angle of incidence, which is called the critical angle and defined by the condition:

$$1 - \eta^2 \sin^2 \theta_1 = 0. \qquad \text{(C.3)}$$

At the critical angle of incidence, k_{z_2} becomes zero; in other words, the waves propagate parallel to the interface. After solving for the critical angle, we obtain $\theta_c = \sin^{-1}(1/\eta)$. For $\theta_1 > \theta_c$, the transmitted field in the second medium can be written as:

$$\begin{bmatrix} E_{2x} \\ E_{2y} \\ E_{2z} \end{bmatrix} = \begin{bmatrix} -i\,\mathrm{E}_1^{(\mathrm{p})}\,\mathrm{t}^{\mathrm{p}}(\theta_1)/(k_2 z_0) \\ \mathrm{E}_1^{(\mathrm{s})}\,\mathrm{t}^{\mathrm{s}}(\theta_1) \\ \mathrm{E}_1^{(\mathrm{p})}\,\mathrm{t}^{\mathrm{p}}(\theta_1)\sqrt{1+(k_2 z_0)^2}/(k_2 z_0) \end{bmatrix} e^{i\,sin\theta_1 k_1 x\, e^{-z/z_0}} \qquad \text{(C.4)}$$

where z_0 is the decay constant defined by:

$$z_0 = \frac{1}{k_2\sqrt{\eta^2 \sin^2\theta - 1}} \qquad \text{(C.5)}$$

Equation C.4 indicates that the field decays exponentially with the decay constant z_0 along the *z*-direction when a plane wave is incident on the planner interfaces above the critical angle. In the case where the entire incident field is reflected back into the same medium, the phenomenon is called total internal reflection. The exponentially decaying field above the interface is called the evanescent field, as shown in Figure C.1b.

There are mainly two advantages of using evanescent field in our scanning probe microscopy system. The polarization of the evanescent field reveals a strong axial component (for p-polarized excitation), which is an important factor for enhancing the field at the apex of a sharp tip. Secondly, the evanescent field created just above the interface can be much larger than that of an incident field. In Equation C.4, we see that for s-polarized light, the evanescent field consists of only an s-polarized field (*y*-component), but for p-polarized light, the evanescent field consists of both *x*- and *z*-components. Importantly, the z-field component becomes stronger than the incident, which in fact depends on the angle of incidence. The field enhancement will be maximum when the angle of incidence is close to the critical angle and will decay as the angle of incidence increases beyond the critical angle [1, 149]

APPENDIX D

HYPER-SPECTRAL IMAGING

The AFM system is from Asylum Research and the spectrometer is from Princeton Instrument. Both systems are equipped with their own controlling software. When the AFM stage is rastered scanning using the Asylum software, it will display the images such as Topography, Amplitude, Phase, Z-sensor, Fluorescent with the given points and lines (pixels). Since the spectrometer is a separate system, the AFM and the spectrometer need to be synchronized to measure the spectrum on individual pixels.

The AFM controller has a pixel clock which is a standard TTL pulse. This pixel is connected to the External Sync of the spectrometer. The number of pixels detected during a complete scan will be more than the input pixels (lines × pixels per line) from the software. The reason for this is the following. When the stage is scanning in a particular size, the stage is raster scanned, it will move with the constant speed within the designed size and on either side, it overshoots some scanning area. On this overshoot region, it stops and returns for both Trace and Retrace. However, the pixel clock comes at constant time, so there will be an extra pixels signal that corresponds to the overshoot time/area. Overall, there are 50% more pixels in one complete Trace and Retrace scan. This information is very important during data analysis.

Figure D.1 shows the timing diagram for external synchronization with a positive edge trigger. In the continuous measurement mode with external synchronization, the

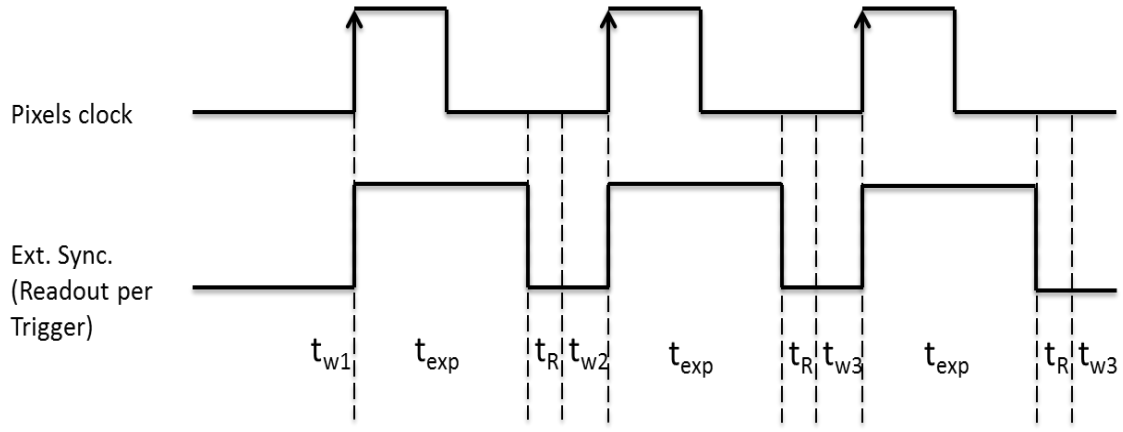

Figure D.1 Timing diagram for External Sync mode with Readout per Trigger option (Standard way of operation).

CCD waits for an external pulse (pixel clock) with the waiting time (t_w). With the external positive pulse, the CCD goes to data acquisition mode for the defined exposer time (t_{exp}). After the exposer time is completed, the system goes for readout (t_R). With this readout, the system completes one acquisition cycle. The system waits for the next external positive pulse (pixel clock) to start the next cycle with the waiting time (t_w). The time interval between pixel clocks is determined by the input parameter in AFM software (scan rate and points per line). In this standard way of operation, we have to be always careful to choose the exposer time (t_{exp}), so that the total time for an acquisition cycle (sum of t_{exp} and t_R) does not exceed the timing between pixel clocks. Otherwise, there will be missing pixels (data). We found an alternative way of operation to overcome this inconvenience. The timing diagram for this new acquisition system is shown in Figure D.2. In this method, the exposer time (t_{exp}) is set to zero as the input parameter. The system goes directly to readout with the external trigger (pixel clock). Since the CCD is exposed all the time, each pixel clock will trigger to readout. In this configuration, there is no hassle of choosing an appropriate exposer time for a different scanning parameter.

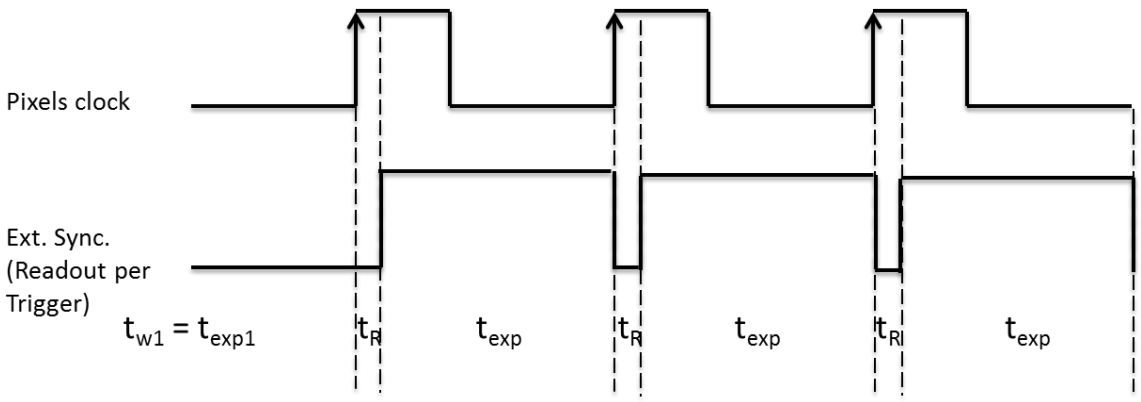

Figure D.2 Timing diagram for External Sync mode with Readout per Trigger option (Implemented in operation).

The internal clock rate of our CCD (Pixis 400) is 80 MHz. The system will go to read out the spectrum in 12.5 nanoseconds after the positive edge trigger of the pixel clock. Since the shutter in front of the camera is kept open for all the time during data acquisition, the camera should be operated below saturation. The number of frames (spectrometer input parameter) for the given measurement should be chosen more than total pixels in the scan. For example, if there are 16 points per line and 10 lines chosen in the input parameter of AFM software, total pixels will be 16 ×2.5×10 = 400. The factor 2.5 is for Trace and Retrace with overshoot.

APPENDIX E

LIGHT THROUGH A LENS

An electric field and its properties (polarization, direction) will undergo transformation as it passes through a lens system. To understand how the electric field is modified, consider a point source is situated at focus from an objective lens, as shown in Figure E.1a. The electric field for an incident light can be expressed in spherical co-ordinate as:

$$\mathbf{E}_{\text{in}} = (\mathbf{E}_{\text{in}} \cdot \mathbf{n}_{\text{r}})\mathbf{n}_{\text{r}} + (\mathbf{E}_{\text{in}} \cdot \mathbf{n}_{\theta})\mathbf{n}_{\theta} + (\mathbf{E}_{\text{in}} \cdot \mathbf{n}_{\phi})\mathbf{n}_{\phi} \tag{E.1}$$

where $\mathbf{n}_{\text{r}}$, $\mathbf{n}_{\theta}$, and $\mathbf{n}_{\phi}$ are the unit vectors in the spherical coordinate system. Since $\mathbf{r}$ and $\mathbf{n}_{\text{r}}$ are in the same direction as the propagation direction ($\mathbf{k}$), due to the transverse nature of electromagnetic field, $\mathbf{E}_{\text{r}}$ will be neglected in further equations. So the remaining field can be expressed as s and p polarized component of incident field as:

$$\mathbf{E}_{\text{in}} = \mathbf{E}_{\text{in}}^{(\text{s})}(\mathbf{E}_{\phi}) + \mathbf{E}_{\text{in}}^{(\text{p})}(\mathbf{E}_{\theta}) \tag{E.2}$$

As shown Figure E.1, the lens converts the spherical wave to the cylindrical wave. In the meantime, the energy flux passing through the lens also needs to be conserved. The power transmitted through a small area is written as:

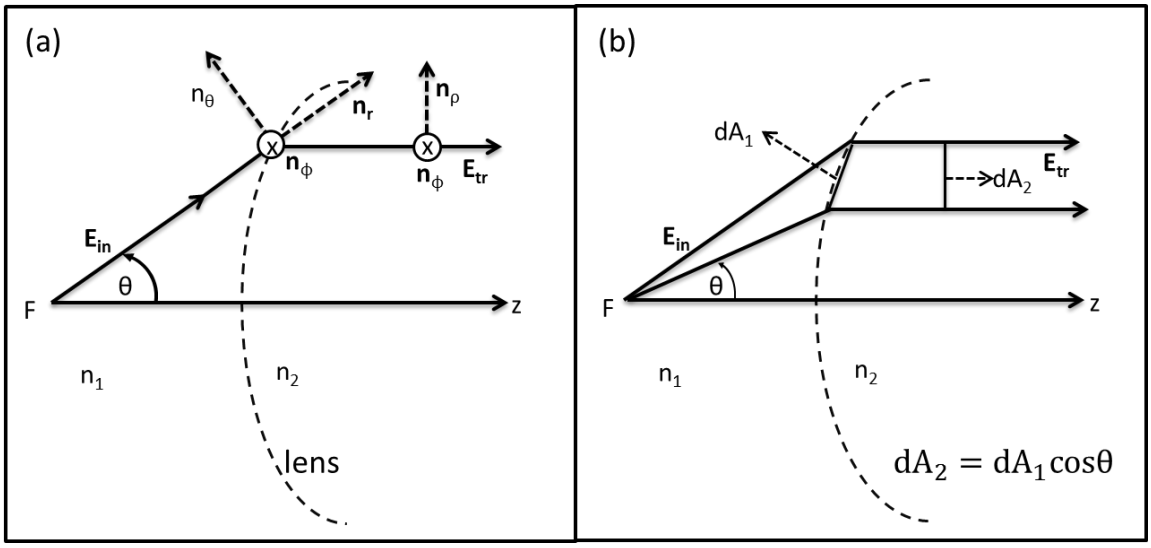

Figure E.1 Schematic of ray diagram for electric field passing through a lens system. (a) Ray diagram showing incident and transmitted field resolved in spherical and cylindrical coordinate system before and after lens, respectively. (b) Mapping of area before and after the lens.

$$P = \frac{1}{2}\frac{1}{\sqrt{z_{\mu\epsilon}}}|\mathbf{E}|^2 dA \tag{E.3}$$

where $z_{\mu\epsilon}$ is the wave impedance and dA is an infinitesimal cross-section perpendicular to the propagating direction. Applying the conservation of energy for a propagating field before and after the lens, the transmitted electric field is related to the incident electric field by the relation:

$$|\mathbf{E}_{tr}| = |\mathbf{E}_{in}|\left(\frac{n_1\mu_2}{n_2\mu_1}\right)^{1/2}\cos^{-1/2}\theta. \tag{E.4}$$

For a nonmagnetic medium, the magnetic permeability at optical frequencies is equal to 1. From the ray diagram, it is clear that an incoming beam (spherical beam) from the spherical coordinate system transfers to the cylindrical coordinate system (parallel beam).

As shown in Figure E.1b, the unit vector $\mathbf{n}_\theta$ maps into $\mathbf{n}_\rho$, the unit vector $\mathbf{n}_\phi$ remains unaffected. Therefore, the transmitted field in cylindrical coordinate system is written as:

$$\mathbf{E}_{\text{tr}} = \left[t^{p}(\mathbf{E}_{\text{in}} \cdot \mathbf{n}_\theta)\mathbf{n}_\rho + t^{s}(\mathbf{E}_{\text{in}} \cdot \mathbf{n}_\phi)\mathbf{n}_\phi\right]\left(\frac{n_1}{n_2}\right)^{1/2} \cos^{-1/2}\theta \qquad \text{(E.5)}$$

where $t^{(s)}$and $t^{(p)}$ are the transmission coefficient for s and p polarized light at the interface. The transmitted field ($\mathbf{E}_{tr}$) after the lens is the Fourier transfer of field from the point source F shown in Figure E.1a. The plot of the transmitted intensity ($|\mathbf{E}_{tr}|^2$) after the lens is known as the back-focal image (BFI) of the lens system.

The unit vector $\mathbf{n}_\rho$ and $\mathbf{n}_\varphi$ can be expressed in terms of the Cartesian unit vector $\mathbf{n}_x$ maps into $\mathbf{n}_y$ using the coordinate transformation:

$$\mathbf{n}_\rho = \cos\phi\mathbf{n}_x + \sin\phi\mathbf{n}_y, \quad \mathbf{n}_\phi = -\sin\phi\mathbf{n}_x + \cos\phi\mathbf{n}_y \qquad \text{(E.6)}$$

Using the above transformation, the transmitted electric field in the Cartesian coordinate system is expressed as:

$$\mathbf{E}_x = A(\theta)\left[\mathbf{E}_\theta\cos\phi - \mathbf{E}_\phi\sin\phi\right], \qquad \mathbf{E}_y = A(\theta)[\mathbf{E}_\theta\sin\phi + \mathbf{E}_\phi\cos\phi] \qquad \text{(E.7)}$$

where $A(\theta) = (n_1/n_{2)}^{1/2}\cos^{-1/2}\theta$.

APPENDIX F

RESONANCE SCATTERING IN NANOSPHERE/DIPOLE ANTENNA

As I discuss in the Chapter 2, the collective oscillation of charges (plasmons) within gold nanoparticles leads to scattering and absorption of the incident radiation. Figure F.1 shows the wavelength-dependent scattering/absorption cross-section for the nanosphere of radius 15 and 50 nm. Finite-difference time domain simulation is used to calculate the scattering and absorption cross-section curves as shown here. Scattering cross-section curves (Figure F.1) have broad peaks at wavelengths ~525 nm and ~540 nm which correspond to plasmons resonance condition for the 15 nm and 50 nm radius sphere, respectively. The absorption of the incident radiation is also peaked close to the resonance wavelengths, as shown in Figure F.1. For the smaller particle, the resonance peak shifts towards short wavelength. As the scattering cross-section relates with the particle size/area, the scattering cross-section for 50 nm radius sphere is more than three orders of magnitude higher than the 15 nm radius sphere (Figure F.1).

Similarly, Figure F.2 shows the absorption/scattering cross-section for a dipole antenna. The dipole antenna is a rounded cylinder having radius of cylinder of 15 nm, radius of curvature of 15 nm, and length of 100 nm. Simulated results reveal that the resonance scattering/absorption occurs at ~ 660 nm excitation wavelength.

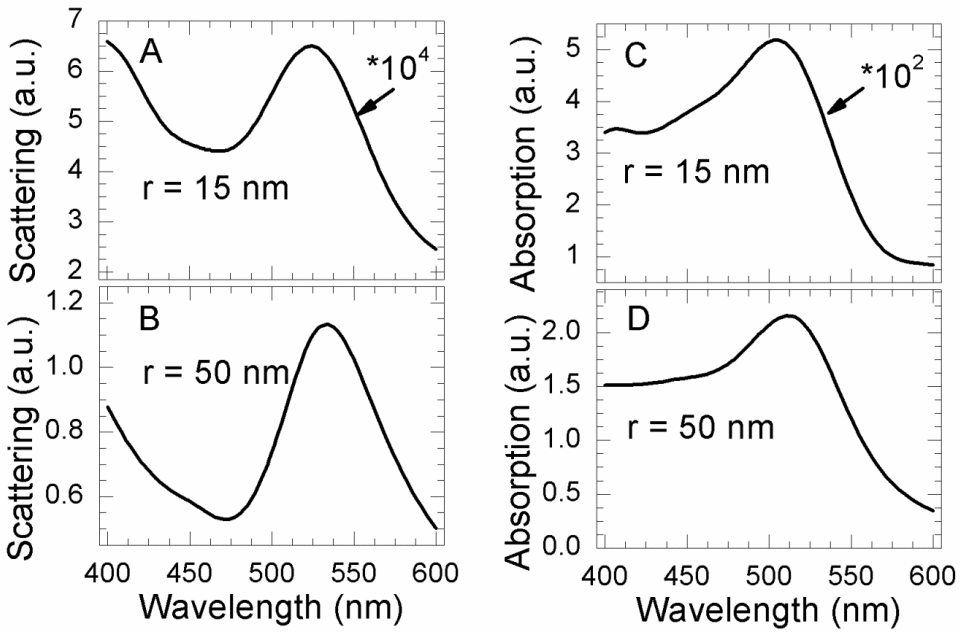

Figure F.1 Scattering/absorption cross-section for nanospheres of radius 15 and 50 nm as the function of excitation wavelengths. Finite-difference time domain simulation is performed using a broadband source.

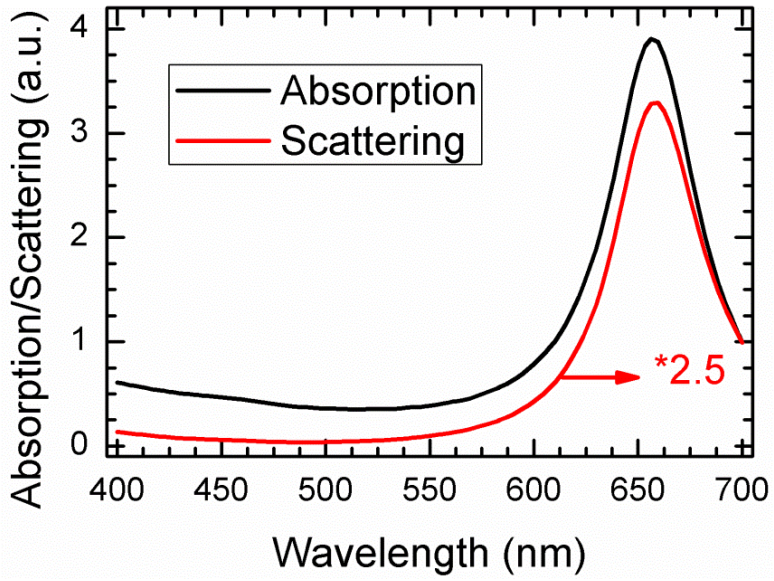

Figure F.2 Absorption/scattering cross-section as the function of excitation wavelength for a dipole antenna. The dipole antenna is rounded-cylindrical in shape with radius of cylinder of 15 nm, radius of curvature of 15 nm, and total length of 100 nm.

APPENDIX G

NITROGEN VACANCY CENTER IN NANODIAMOND

Nitrogen-vacancy color-centers are the point defects in a diamond lattice. A carbon atom in the regular lattice site in a diamond crystal is replaced by a nitrogen atom and a nearest lattice site to the nitrogen atom if vacant; this combination is named a nitrogen-vacancy (NV) color-center in diamond. NV center in diamond are optically active. The emission spectrums of NV centers for four different nanodiamonds measured in our lab are shown in Figure G.1. An important property of NV luminescence is temporal stability as compared to the fluorescent molecules. Not only NV centers in diamond, there are other color centers like silicon, nickel, and chromium.

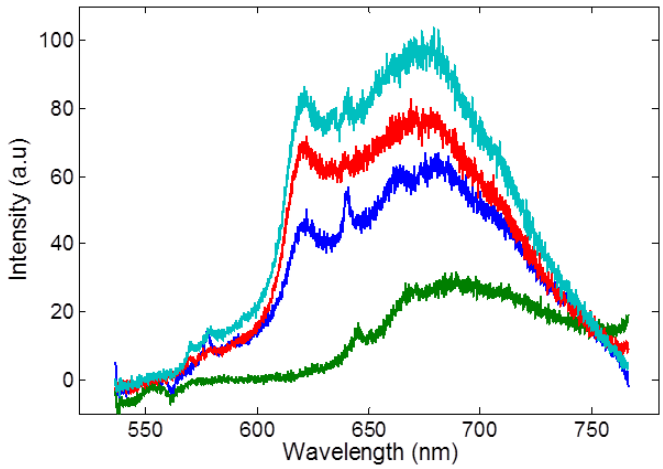

Figure G.1 Emission spectrum from NV centers for four different nanodiamonds. Laser of 488 nm wavelength is used to excite an individual nanodiamond.

REFERENCES

[1] L. Novotny, B. Hecht, *Principles of Nano-Optics*, Cambridge University Press, 2006.

[2] S.W. Hell, J. Wichmann, *Opt. Lett.*, 19 (1994) 780-782.

[3] T.A. Klar, S.W. Hell, *Opt. Lett*., 24 (1999) 954-956.

[4] J.M. Gerton, L.A. Wade, G.A. Lessard, Z. Ma, S.R. Quake, *Phys. Rev. Lett.*, 93 (2004) 180801.

[5] Z. Ma, J.M. Gerton, L.A. Wade, S.R. Quake, *Phys. Rev. Lett.*, 97 (2006) 260801.

[6] B.D. Mangum, C. Mu, J.M. Gerton, *Opt. Express*, 16 (2008) 6183-6193.

[7] L. Novotny, S.J. Stranick, *Annu. Rev. Phys. Chem.*, 57 (2006) 303-331.

[8] T. Endo, K. Kerman, N. Nagatani, H.M. Hiepa, D.-K. Kim, Y. Yonezawa, K. Nakano, E. Tamiya, *Anal. Chem.*, 78 (2006) 6465-6475.

[9] P. Schuck, D. Fromm, A. Sundaramurthy, G. Kino, W. Moerner, *Phys. Rev. Lett.*, 94 (2005) 17402.

[10] P. Bharadwaj, B. Deutsch, L. Novotny, *Adv. Opt. Photon.*, 1 (2009) 438-483.

[11] A.G. Curto, G. Volpe, T.H. Taminiau, M.P. Kreuzer, R. Quidant, N.F. van Hulst, *Science*, 329 (2010) 930-933.

[12] T. Taminiau, F. Stefani, F. Segerink, N. Van Hulst, *Nat. Photon.*, 2 (2008) 234-237.

[13] S. Kühn, G. Mori, M. Agio, V. Sandoghdar, *Mol. Phys.*, 106 (2008) 893-908.

[14] S. Kühn, V. Sandoghdar, *Appl. Phys. B*, 84 (2006) 211-217.

[15] H. Gersen, M. García-Parajó, L. Novotny, J. Veerman, L. Kuipers, N. Van Hulst, *J. Microsc.*, 202 (2001) 374-378.

[16] H. Gersen, M.F. Garcia-Parajo, L. Novotny, J.A. Veerman, L. Kuipers, N.F. van Hulst, *Phys. Rev. Lett.*, 85 (2000) 5312-5315.

[17] R.J. Moerland, T.H. Taminiau, L. Novotny, N.F. Van Hulst, L. Kuipers, *Nano Lett.*,

8 (2008) 606-610.

[18] T. Taminiau, F. Stefani, N. Van Hulst, *New J. Phys.*, 10 (2008) 105005.

[19] J. Li, A. Salandrino, N. Engheta, *Phys. Rev. B*, 76 (2007) 245403.

[20] Z. Li, T. Shegai, G. Haran, H. Xu, *Acs Nano*, 3 (2009) 637-642.

[21] T. Kosako, Y. Kadoya, H.F. Hofmann, *Nat. Photon.*, 4 (2010) 312-315.

[22] D. Unitt, A. Bennett, P. Atkinson, K. Cooper, P. See, D. Gevaux, M. Ward, R. Stevenson, D. Ritchie, A. Shields, *J. Opt. B: Quantum and Semiclassical Optics*, 7 (2005) S129.

[23] B. Lounis, M. Orrit, *Rep. Prog. Phys.*, 68 (2005) 1129.

[24] W. Moerner, *New J. Phys.*, 6 (2004) 88.

[25] J.W. Goodman, *Introduction to Fourier Optics*, McGraw-Hill, 1996.

[26] Rayleigh, *Philos. Mag. Series*, 5, 8 (1879) 261-274.

[27] J.M. Vigoureux, D. Courjon, *Appl. Opt.*, 31 (1992) 3170-3177.

[28] J.-J. Greffet, R. Carminati, *Prog. Surf. Sci.*, 56 (1997) 133-237.

[29] B. Hecht, B. Sick, U.P. Wild, V. Deckert, R. Zenobi, O.J. Martin, D.W. Pohl, *J. Chem. Phys.*, 112 (2000) 7761-7774.

[30] H.F. Arnoldus, J.T. Foley, *Opt. Lett.*, 28 (2003) 1299-1301.

[31] J.D. Jackson, *Classical Electrodynamics*, Wiley, 1998.

[32] M. Born, E. Wolf, Principles of Optics: *Electromagnetic Theory of Propagation, Interference and Diffraction of Light*, Cambridge University Press, 1997.

[33] H. Kuhn, *J. Chem. Phys.*, 53 (1970) 101-108.

[34] R. Chance, A. Prock, R. Silbey, *Adv. Chem. Phys.*, 37 (1978) 65.

[35] E.M. Purcell, *Phys. Rev.* 69, 681 (1946).

[36] K.H. Drexhage, *J. Lumin.*, 1–2 (1970) 693-701.

[37] P. Drude, *Annalen der Physik*, 306 (1900) 566-613.

[38] G.E.R. Schulze, *Berichte der Bunsengesellschaft für physikalische Chemie*, 71

(1967) 641-641.

[39] C. Kittel, *Introduction to Solid State Physics*, Wiley, 2004.

[40] P.B. Johnson, R.W. Christy, *Phys. Rev. B*, 6 (1972).

[41] N.K. Grady, N.J. Halas, P. Nordlander, *Chem. Phys. Lett.*, 399 (2004) 167-171.

[42] G. Mie, *Ann. Phys.(Leipzig)*, 1 (1976) 377-445.

[43] W. Sun, N.G. Loeb, B. Lin, *Appl. Opt.*, 44 (2005) 2338-2342.

[44] E.M. Purcell, C.R. Pennypacker, *Astrophys. J.*, 186 (1973) 705-714.

[45] K.L. Kelly, C. Eduardo, Z. Lin Lin, C.S. George, *J. Phys. Chem. B*, 107 (2003).

[46] C.F. Bohren, D.R. Huffman, *Absorption and Scattering of Light by Small Particles*, Wiley, 1983.

[47] H.C. Hulst, H.C. van de Hulst, *Light Scattering by Small Particles*, Dover Publications, 1957.

[48] B.T. Draine, P.J. Flatau, *JOSA A*, 11 (1994) 1491-1499.

[49] C. Noguez, *J. Phys. Chem. C*, 111 (2007).

[50] P. Biagioni, J.-S. Huang, B. Hecht, *Rep. Prog. Phys.* 75 (2012) 24402.

[51] T. Taminiau, R. Moerland, F. Segerink, L. Kuipers, N. van Hulst, *Nano Lett.*, 7 (2007) 28-33.

[52] A. Taflove, S.C. Hagness, *Computational Electrodynamics: The Finite-Difference Time-Domain Method*, Artech House, Incorporated, 2005.

[53] F. Hao, C. Nehl, J. Hafner, P. Nordlander, *Nano Lett.*, 7 (2007) 729-732.

[54] C. Hafner, *Phys. Status Solidi B*, 244 (2007) 3435-3447.

[55] M. Viktor, C.-A. Enrique, P.-S. Isabel, P.-J. Jorge, M.L.-M. Luis, F.J.G.d. Abajo, *Adv. Mater.*, 20 (2008).

[56] M. Micic, N. Klymyshyn, Y.D. Suh, H.P. Lu, *J. Phys. Chem. B*, 107 (2003) 1574-1584.

[57] J. Pomplun, S. Burger, L. Zschiedrich, F. Schmidt, *Phys. Status Solidi B*, 244 (2007) 3419-3434.

[58] T. Kalkbrenner, U. Hakanson, A. Schädle, S. Burger, C. Henkel, V. Sandoghdar,

Phys. Rev. Lett. 95, 200801 (2005).

[59] J.S. Shumaker-Parry, H. Rochholz, M. Kreiter, *Adv. Mater.*, 17 (2005) 2131-2134.

[60] L. Liz-Marzán, *Langmuir: ACS J. Surf. colloids*, 22 (2006) 32-41.

[61] M.P. Pileni, *J. Phy. Chem. C*, 111 (2007).

[62] P. Mühlschlegel, H.-J. Eisler, O. Martin, B. Hecht, D. Pohl, *Science*, 308 (2005) 1607-1609.

[63] J.A. Porto, R. Carminati, J.-J. Greffet, *J. Appl. Phys.*, 88 (2000) 4845-4850.

[64] J. Sun, P.S. Carney, J.C. Schotland, *J. Appl. Phys.*, 102 (2007) -.

[65] M. Esslinger, R. Vogelgesang, *ACS Nano*, 6 (2012) 8173-8182.

[66] F. Keilmann, R. Hillenbrand, P *Philos. Trans. A Math. Phys. Eng. Sci*, (2004) 787-806.

[67] M.B. Raschke, C. Lienau, *Appl. Phys. Lett.*, 83 (2003) 5089-5091.

[68] C. Huber, A. Trügler, U. Hohenester, Y. Prior, W. Kautek, *Phys. Chem. Chem. Phys.*, 16 (2014) 2289-2296.

[69] W. Chen, Q. Zhan, *Opt. Express*, 15 (2007) 4106-4111.

[70] R. HillenbRand, B. Knoll, F. Keilmann, *J. Microsc.*, 202 (2001) 77-83.

[71] N.A. Issa, R. Guckenberger, O*pt. Express*, 15 (2007) 12131-12144.

[72] A. Bouhelier, M. Beversluis, A. Hartschuh, L. Novotny, *Phys. Rev. Lett.*, 90 (2003) 013903.

[73] L. Novotny, R.X. Bian, X.S. Xie, *Phys. Rev. Lett.*, 79 (1997) 645-648.

[74] K. Anika, Y. Zongfu, F. Shanhui, A. Yuri, M. Klaus, W.E. Moerner, *Nat. Photon.*, 3 (2009).

[75] H. Mertens, J.S. Biteen, H.A. Atwater, A. Polman, *Nano Lett.*, 6 (2006) 2622-2625.

[76] W.L. Stutzman, G.A. Thiele, *Antenna Theory and Design*, Wiley, 1998.

[77] L. Novotny, N. van Hulst, *Nat. Photon.*, 5 (2011) 83-90.

[78] G.W. Bryant, F.J. García de Abajo, J. Aizpurua, *Nano Lett.*, 8 (2008) 631-636.

[79] T.H. Taminiau, F.D. Stefani, N.F. van Hulst, *Opt. Express*, 16 (2008) 10858-10856.

[80] H.G. Frey, F. Keilmann, A. Kriele, R. Guckenberger, *Appl. Phys. Lett.*, 81 (2002) 5030-5032.

[81] A. McLeod, A. Weber-Bargioni, Z. Zhang, S. Dhuey, B. Harteneck, J.B. Neaton, S. Cabrini, P.J. Schuck, *Phys. Rev. Lett.*, 106 (2011) 037402.

[82] Z. Zhang, A. Weber-Bargioni, S. Wu, S. Dhuey, S. Cabrini, P.J. Schuck, *Nano Lett.*, 9 (2009) 4505-4509.

[83] H. Kim, A. Ghimire, S. Jamali, T.K. Djidjou, J.M. Gerton, A. Rogachev, *Phys. Rev. B*, 86 (2012) 024518.

[84] H.G. Frey, S. Witt, K. Felderer, R. Guckenberger, *Phys. Rev. Lett.*, 93 (2004) 200801.

[85] C. Mu, B.D. Mangum, C. Xie, J.M. Gerton, *IEEE J. Sel. Top. Quantum Electron*.

[86] B.D. Mangum, *Exploring the limits of near-field fluorescence microscopy: Toward molecular-scale imaging of bilolgical systems*, PhD dissertation, University of Utah, 2010.

[87] F. Koberling, U. Kolb, G. Philipp, I. Potapova, T. Basché, A. Mews, *J. Phys. Chem. B*, 107 (2003) 7463-7471.

[88] I. Chung, K.T. Shimizu, M.G. Bawendi, *Proc. Natl. Acad. Sci.*, 100 (2003) 405-408.

[89] S. Empedocles, R. Neuhauser, M. Bawendi, *Nature*, 399 (1999) 126-130.

[90] C. Huang, A. Bouhelier, G. Colas des Francs, A. Bruyant, A. Guenot, E. Finot, J.-C. Weeber, A. Dereux, *Phys. Rev. B*, 78 (2008) 155407.

[91] A. Drezet, A. Hohenau, A.L. Stepanov, H. Ditlbacher, B. Steinberger, N. Galler, F.R. Aussenegg, A. Leitner, J.R. Krenn, *Appl. Phys. Lett.*, 89 (2006) -.

[92] M.U. González, A.L. Stepanov, J.-C. Weeber, A. Hohenau, A. Dereux, R. Quidant, J.R. Krenn, *Opt. Lett.*, 32 (2007) 2704-2706.

[93] M.A. Lieb, J.M. Zavislan, L. Novotny, *J. Opt. Soc. Am. B*, 21 (2004) 1210-1215.

[94] E.B. Ureña, M.P. Kreuzer, S. Itzhakov, H. Rigneault, R. Quidant, D. Oron, J. Wenger, *Adv. Mater.*, 24 (2012) OP314-OP320.

[95] R.A. Schultz, T. Nielsen, J.R. Zavaleta, R. Ruch, R. Wyatt, H.R. Garner, *Cytometry*, 43 (2001) 239-247.

[96] K. Yee, *IEEE Transactions on Antennas and Propagation*, 14 (1966) 302-307.

[97] Y. Hao, R. Mittra, *FDTD Modeling of Metamaterials: Theory and Applications*, Artech house, 2008.

[98] J.-P. Berenger, *J. Comput. Phys.*, 114 (1994) 185-200.

[99] S. Gedney, *Introduction to the Finite-Difference Time-Domain (FDTD) Method for Electromagnetics*, Morgan & Claypool Publishers, 2011.

[100] Lumerical Solutions, Inc., in.

[101] S. Kühn, U. Håkanson, L. Rogobete, V. Sandoghdar, *Phys. Rev. Lett.*, 97 (2006) 017402.

[102] P. Biagioni, M. Savoini, J.-S. Huang, L. Duò, M. Finazzi, B. Hecht, *Phys. Rev. B*, 80 (2009) 153409.

[103] L. Neumann, J. van 't Oever, N.F. van Hulst, *Nano Lett.*, 13 (2013) 5070-5074.

[104] B.D. Mangum, E. Shafran, C. Mu, J.M. Gerton, *Nano Lett.*, 9 (2009) 3440-3446.

[105] J.H. Hafner, C.-L. Cheung, T.H. Oosterkamp, C.M. Lieber, *J. Phys. Chem. B*, 105 (2001) 743-746.

[106] E. Shafran, B.D. Mangum, J.M. Gerton, *Nano Lett.*, 10 (2010) 4049-4054.

[107] M. Böhmler, N. Hartmann, C. Georgi, F. Hennrich, A. Green, M. Hersam, A. Hartschuh, *Opt. Express*, 18 (2010) 16443-16451.

[108] E. Shafran, *Optical Interactions Between Single Emitters and Nanostructures*, PhD dissertation, University of Utah, 2011.

[109] L. Schulz, *JOSA*, 44 (1954) 357-362.

[110] L. Schulz, F. Tangherlini, *JOSA*, 44 (1954) 362-367.

[111] J. Vesenka, S. Manne, R. Giberson, T. Marsh, E. Henderson, *Biophys. J.*, 65 (1993) 992-997.

[112] E. Shafran, B.D. Mangum, J.M. Gerton, *Phys. Rev. Lett.*, 107 (2011) 037403.

[113] R.M. Dickson, D.J. Norris, W.E. Moerner, *Phys. Rev. Lett.*, 81 (1998) 5322-5325.

[114] D.J. Griffiths, *Introduction to Quantum Mechanics*, Pearson Education, 2005.

[115] W. Lukosz, R. Kunz, *JOSA*, 67 (1977) 1615-1619.

[116] A.I. Chizhik, A.M. Chizhik, D. Khoptyar, S. Bär, A.J. Meixner, *Nano Lett.*, 11 (2011) 1131-1135.

[117] S.A. Empedocles, R. Neuhauser, M.G. Bawendi, *Nature*, 399 (1999) 126-130.

[118] X. Brokmann, L. Coolen, J.-P. Hermier, M. Dahan, *Chem, Phys.*, 318 (2005) 91-98.

[119] W.G.J.H.M. van Sark, P.L.T.M. Frederix, D.J. Van den Heuvel, H.C. Gerritsen, A.A. Bol, J.N.J. van Lingen, C. de Mello Donegá, A. Meijerink, *J. Phys. Chem. B*, 105 (2001) 8281-8284.

[120] A. Cuche, A. Drezet, Y. Sonnefraud, O. Faklaris, F. Treussart, J.-F. Roch, S. Huant, *Opt. Express*, 17 (2009) 19969-19980.

[121] R.Q. Twiss, A.G. Little, R. Hanbury Brown, *Nature*, 180 (1957) 324-326.

[122] A.M. Schrand, S.A.C. Hens, O.A. Shenderova, *Crit. Rev. Solid State Mater. Sci.*, 34 (2009) 18-74.

[123] B.R. Smith, D.W. Inglis, B. Sandnes, J.R. Rabeau, A.V. Zvyagin, D. Gruber, C.J. Noble, R. Vogel, E. Ōsawa, T. Plakhotnik, *Small*, 5 (2009) 1649-1653.

[124] J. Tisler, G. Balasubramanian, B. Naydenov, R. Kolesov, B. Grotz, R. Reuter, J.-P. Boudou, P.A. Curmi, M. Sennour, A. Thorel, M. Börsch, K. Aulenbacher, R. Erdmann, P.R. Hemmer, F. Jelezko, J. Wrachtrup, *ACS Nano*, 3 (2009) 1959-1965.

[125] I.I. Vlasov, O. Shenderova, S. Turner, O.I. Lebedev, A.A. Basov, I. Sildos, M. Rähn, A.A. Shiryaev, G. Van Tendeloo, *Small*, 6 (2010) 687-694.

[126] I. Aharonovich, A.D. Greentree, S. Prawer, *Nat. Photon.*, 5 (2011) 397-405.

[127] I. Aharonovich, S. Castelletto, D.A. Simpson, A. Stacey, J. McCallum, A.D. Greentree, S. Prawer, *Nano Lett.*, 9 (2009) 3191-3195.

[128] T. Kuykendall, P.J. Pauzauskie, Y. Zhang, J. Goldberger, D. Sirbuly, J. Denlinger, P. Yang, *Nat. Mater.*, 3 (2004) 524-528.

[129] X. Duan, Y. Huang, R. Agarwal, C.M. Lieber, *Nature*, 421 (2003) 241-245.

[130] C.J. Barrelet, A.B. Greytak, C.M. Lieber, *Nano Lett.*, 4 (2004) 1981-1985.

[131] C. Soci, A. Zhang, B. Xiang, S.A. Dayeh, D.P.R. Aplin, J. Park, X.Y. Bao, Y.H. Lo, D. Wang, *Nano Lett.*, 7 (2007) 1003-1009.

[132] A.M. Schwartzberg, S. Aloni, T. Kuykendall, P.J. Schuck, J.J. Urban, *Opt. Express*, 19 (2011) 8903-8911.

[133] D. Kim, I. Libon, C. Voelkmann, Y. Shen, V. Petrova-Koch, *Phys. Rev. B*, 55 (1997) R4907.

[134] C.-K. Sun, J.-C. Liang, J.-C. Wang, F.-J. Kao, S. Keller, M.P. Mack, U. Mishra,

S.P. DenBaars, *Appl. Phys. Lett.*, 76 (2000) 439-441.

[135] P. Schuck, R. Grober, A. Roskowski, S. Einfeldt, R. Davis, *Appl. Phys. Lett.*, 81 (2002) 1984-1986.

[136] M.A. Reshchikov, H. Morkoç, *J. Appl. Phys.*, 97 (2005).

[137] A. Tittl, X. Yin, H. Giessen, X.-D. Tian, Z.-Q. Tian, C. Kremers, D.N. Chigrin, N. Liu, *Nano Lett.*, 13 (2013) 1816-1821.

[138] Y. Ding, J. Motohisa, B. Hua, S. Hara, T. Fukui, *Nano Lett.*, 7 (2007) 3598-3602.

[139] B. Hua, J. Motohisa, S. Hara, T. Fukui, *Phys. Status Solidi C*, 5 (2008) 2722-2725.

[140] J.P. Long, R.A. Flynn, I. Vurgaftman, B.S. Simpkins, A.J. Mäkinen, M.A. Mastro, P.E. Pehrsson, *Appl. Phys. Lett.*, 97 (2010) -.

[141] S. Rühle, L. Van Vugt, H.-Y. Li, N. Keizer, L. Kuipers, D. Vanmaekelbergh, *Nano Lett.*, 8 (2008) 119-123.

[142] J.I. Pankove, *Optical Processes in Semiconductors*, Dover, 1971.

[143] G. Mauckner, K. Thonke, T. Baier, T. Walter, R. Sauer, *J. Appl. Phys.*, 75 (1994) 4167-4170.

[144] M.S. Kang, C.-H. Lee, J.B. Park, H. Yoo, G.-C. Yi, *Nano Energy*, 1 (2012) 391-400.

[145] Y. Toda, T. Matsubara, R. Morita, M. Yamashita, K. Hoshino, T. Someya, Y. Arakawa, *Appl. Phys. Lett.*, 82 (2003) 4714-4716.

[146] R. Chen, *J. Lumin.*, 102 (2003) 510-518.

[147] W. contributors, *Mie scattering* in, Wikipedia, The Free Encyclopedia.

[148] E.J. Sánchez, L. Novotny, X.S. Xie, *Phys. Rev. Lett.*, 82 (1999) 4014-4017.

[149] D. Axelrod, T.P. Burghardt, N.L. Thompson, *Annu. Rev. Biophy. Bio.* 13 (1984) 247-268.